Damage and fracture mechanisms investigations of an aluminium laser beam weld

(Vom Promotionsausschuss der Technischen Universität Hamburg-Harburg als Dissertation angenommene Arbeit)

Authoress:

P. Cambrésy

Damage and fracture mechanisms investigations of an aluminium laser beam weld

(Vom Promotionsausschuss der Technischen Universität Hamburg-Harburg als Dissertation angenommene Arbeit)

Authoress:

P. Cambrésy

(Institute for Materials Research)

GKSS 2006/5

Damage and fracture mechanisms investigations of an aluminium laser beam weld

Patricia Cambrésy

124 pages with 73 figures and 7 tables

Abstract

The present work deals with the characterisation of the fracture behaviour of an aluminium under-matched weld using finite element methods. The strain concentration and the elevated triaxiality within the weld favours crack extension and such weld mismatch configuration is detrimental to the life of a structure. Two damage models have been applied, namely the Gurson-Tvergaard-Needleman model and a cohesive model. In spite of their difference in representing the fracture process zone, both models are able to evaluate the fracture resistance of non-homogeneous materials. Good prediction of the experimental results were obtained, and the influencing factors controlling the fracture mechanisms of the laser weld in terms of joint properties have been determined.

Bruch- und schädigungsmechanische Bewertung von Laser-Schweißverbindungen

Zusammenfassung

In der vorliegenden Arbeit wird die Charakterisierung des Bruchverfahrens in Aluminium-Under-matched-Schweißverbindungen mit Finite-Element-Methoden abgehandelt. Die Dehnungskonzentration und die höhere Mehrachsigkeit in der Schweißnaht beeinflussen die Risszähigkeit. Solche Schweißverbindungen sind für das Leben einer Struktur schädlich. Zwei Schädigungsmodelle wurden benutzt: das Gurson-Tvergaard-Needleman-Modell und ein Kohäsivmodell. Trotz deren Unterschied in der Beschreibung der Bruchprozesszone sind beide Modelle geeignet, den Bruchwiderstand von nicht-homogenen Werkstoffen zu bewerten. Eine gute Vorhersage der experimentellen Ergebnisse wurde erreicht, und die wichtigsten Faktoren für die Bruchmechanismen in Laserschweißverbindungen hinsichtlich der Joint-Eigenschaften sind bestimmt worden.

Danksagung

iv

Notations

δ_0	Maximum separation of the cohesive elements
δ_N, δ_T	Normal and tangential separations of the cohesive elements
δ_5	CTOD-Definition after [86]
Δa	Crack extension
Γ_0	Cohesive energy
ϵ_{pl}	Plastic strain
η	Stress triaxiality
κ	Damage acceleration factor in the GTN-model
σ_0	Yield strength
a	Crack length
B	Thickness of fracture mechanics specimen
D, w, b	Size of a finite element (height, width, thickness)
E	Young's modulus
f	Void volume fraction
f_0	Initial void volume fraction in the GTN-model
f_c	Critical void volume fraction in the GTN-model
f_f	Final void volume fraction in the GTN-model
f^*	modified damage variable $f^*(f)$ in the GTN-model
f_u^*	$f^*(f = f_f)$ in the GTN-model
G	Energy release rate
2H	Width of fusion zone
J	J-integral
K	Stress intensity factor
M, m_{global}	Mismatch ratio
m_{local}	Local mismatch ratio
n	Strain hardening exponent
q_1, q_2, q_3	Model parameters affecting the GTN yield surface
r	Void radius
r_y	Plastic zone size
T_0	Maximum cohesive traction
T_N, T_T	Normal and tangential cohesive tractions
W	Width of fracture mechanics specimen

Acronyms

BM	Base Material
CMOD	Crack Mouth Opening Displacement
CTOA	Crack Tip Opening Angle
CTOD	Crack Tip Opening Displacement
EPFM	Elastic Plastic Fracture Mechanic
ES	Evolution Strategy
FZ	Fusion Zone
GTN	Gurson-Tvergaard-Needleman model
HAZ	Heat Affected Zone
LEFM	Linear Elastic Fracture Mechanics
LBW	Laser Beam Weld
MFT	Micro flat tensile specimen
TSL	Traction-separation law

Contents

Chapter 1

Introduction

The Comet aircraft designed by de Havilland of England was a revolution when it first flew in July 1949 as it was the first commercial airliner ever built to use turbojet engines. The aircraft maker managed to minimise the aircraft weight and the fuel consumption to transport more passengers and freight. Unfortunately, after eighteen months of service, some of the airplanes went down. Intensive investigations followed to determine the origin of the crashes. A test, carried out on a full scale aircraft placed into a water tank to study the cabin pressurisation, revealed the formation of a fatigue crack from a rivet hole at a window corner that propagated to catastrophic failure.

This well known example in the history of aviation illustrates the modern philosophy of the aerospace industry: the desire to transport numerous passengers at reduced costs. One way to achieve this increase in performance is to minimise the weight of the aircraft itself and therefore reduce the fuel consumption. However, the investigations that followed the crashes pointed out first the necessity to validate both aircraft design and materials in terms of damage resistance and second, the importance of post crash investigations to clarify the origins of the failure in order to prevent any fatal ruptures. Furthermore, the inspections showed a critical problem in airplanes: the occurrence of corrosion at rivet holes.

Traditionnally made of aluminum alloys, the new generation of aircrafts, such as the future A380, contains only 60% of aluminum. The remaining 40 % consist of modern composite materials that are lighter. Moreover, novel technologies such as improved welding techniques have been developed to increase the performance and competitiveness of the aircraft. Weldment in aircraft is, however, not a new concept. Airplanes containing welded steel or titanium parts (as in the F14 Fighter) have flown since decades but the use of welding has decreased with the appearance of "all aluminium planes" as the main problem had resided in the quality of the aluminium welds made of traditional welding techniques such as arc welding. The development of friction stir welding or fusion welding has opened the door to aluminium weld in planes. Airbus introduces the laser beam welding technology to join the stringers to the lower fuselage shells in its A318. Added to the weight and manufacturing time gains, the welding technology presents higher resistance against corrosion and improved behaviour under fatigue than the traditional riveting techniques. Investigations are carried out to extend this technology to other parts of the aircraft fuselage. The materials used for the fuselage must be highly damage tolerant that is resistant to damage propagation.

In aluminium alloys, a crack grows while under static loading in a ductile manner by the formation and growth of cavities that damage the material. These microporosities can either origin from impurities such as dispersoids and second phase particles. The circumstances under which those micro pores grow and coalesce are the basis of the fracture mechanics theory applied to ductile failure. The resistance of the material to damage expressed by the material fracture resistance can be analysed by experiments and numerical simulations. The combined use of experimental and numerical approaches permit the validation of the damage models as well as an improved understanding of the failure mechanisms. Moreover, experimental determination of the fracture resistance of a material is generally carried out on laboratory coupons whose geometry and loading conditions try to represent the service conditions of a component or a structure. Only a limited amount of full scale structure tests exist because of the high cost of such tests as well as the considerable need of materials. Nowadays, the use of computational mechanics permits to simulate complex structures with high accuracy and then get confidence about the macroscale phenomenon taking place.

In this work, the damage and fracture behaviour of an aluminium Al6056 laser beam weld is investigated. The welded Al6056 sheets have been sent by the EADS Corporate Research Centre in France to GKSS Research Centre as part of a project between the two centres. The objective of the project was to investigate the properties of the Al6056 laser beam weld in terms of tensile properties and resistance to crack extension. Both the tensile and the fracture toughness tests have therefore been carried out within the joining technologies group of GKSS. Moreover, the desire to improve the understanding of the fracture behaviour of high strength aluminium alloys and of its weldment has permitted to launch a European sponsored project called IDA: "Investigations on Damage tolerant Aluminium alloys" in which GKSS is involved in the experimental and numerical workpackages.

A typical attribute of aluminium welds is the reduction of strength in the fusion zone. The weld metal is then a preferential location for crack extension because the crack driving force for crack extension is smaller than in the parent metal. The whole weld component is therefore weakened. Due to the welding process and to an eventual addition of filler material, both the microstructure and mechanical properties of the weld are not homogeneous. Three main regions are observed in a laser weld: the fusion zone (or weld metal), an intermediate region called the heat affected zone and the base material. As a consequence the location of a crack within the weld influences its fracture resistance. This particular aspect is investigated both experimentally and numerically by considering the crack within these three main zones of the laser beam weld: in the middle of the fusion zone, within the heat affected zone and in the base material.

Damage models are able to describe the ductile fracture by taking into consideration the mechanism of initiation, growth and coalescence of voids. Two different models are applied: the Gurson-Tvergaard-Needleman model and the cohesive model. These two models present different approaches to simulate crack extension. The first one, the GTN-model, is based on the idea that fracture results from the process of voids nucleation, growth and coalescence whereas the cohesive model considers the evolution of the crack through the separation of the two crack surfaces in the process zone. Another difference between the two models resides in their implementation in a FE-code. The GTN-model is a coupled model and the continuum elements behave accordingly to the GTN-plastic

potential that accounts for damage evolution, whereas the cohesive elements are interface elements that are placed between the continuum element following the von Mises plasticity. These two models are applied to simulate crack extension of the aluminium laser weld under static loading.

Chapter 2 presents background information on the basics of the fracture mechanics theory and reviews the existing damage models to simulate crack extension. A detailed description of the two models employed is also given. The microstructure and mechanical properties of the Al6056 T78 laser beam weld are described in Chapter 3. Fracture mechanics test results carried out on compact specimens with various initial crack positions are discussed at the end of the chapter. Chapters 4 and 5 present the numerical results obtained from the Gurson-Tvergaard-Needleman model and Chapter 6 is dedicated to the numerical simulation of crack extension using the cohesive zone model. Chapters 5 and 6 emphasise the understanding on the occurrence of crack path deviation as functions of the model parameters as well as functions of the weld dimensions and mechanical properties of the different regions of the present laser beam weld.

Chapter 2

Background

Microcracks and defects are inevitable in materials and components. The aim of fracture mechanics is to understand the circumstances, the mechanisms under which those localised microcracks propagate to macroscopic fracture and to prevent the occurrence of such catastrophic failures. Nowadays two complementary approaches exist to predict and analyse the failure of a component, structure: a global approach based on fracture mechanics equations and a local approach involving damage mechanics. The global approach has been developed since the beginning of the 20th century and considers the presence of an existing flaw as origin of fracture. Damage mechanics is a more recent approach and its development has become easier with the growth of computer capacity since finite element codes are required. Moreover, the use of damage mechanics is not limited to precracked structure. Those two approaches are presented in the present chapter.

2.1 Fracture mechanics

Griffith [42] proposed an energy criterion for fracture in the 1920's. Fracture takes place when the energy available to create two new surfaces is high enough to overcome the resistance of the material. The energy release rate G is the driving force for fracture and is expressed by Eq. (2.1) for a crack of length 2a in an infinite plate subjected to remote tensile stress. σ:

$$G = \frac{\pi \sigma^2 a}{E} \tag{2.1}$$

Linear elastic fracture mechanics

In linear elastic fracture theory (LEFM), the stresses at the crack tip can be expressed by the stress intensity factor: K. For a through-thickness crack in an infinite plate subjected to a remote tensile stress, K is expressed by $K_I = \sigma\sqrt{\pi a}$ and is related to the energy release rate by $G = \frac{K_I^2}{E}$. Failure under plane strain state occurs when the stress intensity factor reaches a critical value K_{IC} ($K_I = K_{IC}$) called the fracture toughness which is a function of the temperature, strain rate and of course of the material. Using the stress intensity factor, the different components of the stress tensor at the crack tip can be

calculated using the Williams analysis:
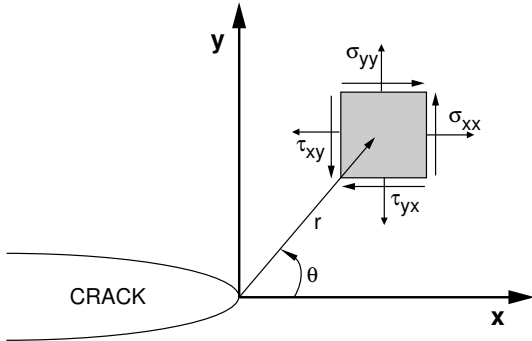
$$\sigma_{ij} = \frac{K_I}{\sqrt{2\pi r}} f_{ij}(\theta) + T\delta_{1i}\delta_{1j} + R, \quad (2.2)$$

Figure 2.1: Crack tip stresses in an elastic material

with r the radial distance from the crack tip and θ the angular position as schematised in Figure 2.1. The Williams expression is a power series whose first term is singular in $1/\sqrt{r}$. The second term of Eq. (2.2) is called the T-stress and it influences the plastic zone shape and the stresses inside the plastic zone. The T-stress is often omitted in crack tip stress analysis but it does become of importance in the case of interface cracks and problems of constraint effects. The higher order terms (R) vanish near the crack tip. Classical fracture mechanics theory considers only the singular term. Analytical solutions for K_I exist for most of the fracture mechanics specimens and structural configurations considering either plane stress or plane strain condition. The domain in which the stress intensity factor K is valid is called the K-domain.

A linear elastic analysis of a sharp crack predicts infinite stresses at the crack tip. In metals, plasticity takes place at the crack tip with stress relaxation. To account for such effects, simple corrections of the previous theory have been proposed by Irwin [49]. Under moderate yielding, the K-field solutions are corrected by the size of the plastic zone: the zone in which plastic deformation takes place. The plastic zone can be described as a function of the angle θ and reads:

$$r_y(\theta) = \begin{cases} \frac{1}{4\pi}\left(\frac{K_I}{\sigma_0}\right)^2[1 + cos\theta + \frac{3}{2}sin^2\theta], & \text{for plane stress} \\ \frac{1}{4\pi}\left(\frac{K_I}{\sigma_0}\right)^2[(1-2\nu)^2(1 + cos\theta) + \frac{3}{2}sin^2\theta], & \text{for plane strain} \end{cases} \quad (2.3)$$

When $\theta = 0$, r_y represents the diameter of the plastic zone along the ligament. The plane stress plastic zone is larger than the plane strain one.

For further increase of yielding, the LEFM theory is not valid anymore since plastic deformation occurs over a large portion of the specimen or component and the global behaviour is not linear anymore. Elastic-plastic fracture mechanics (EPFM) has then been introduced. Two elastic-plastic parameters are defined to characterise the crack tip conditions: the CTOD (Crack Tip Opening Displacement) and the J-integral.

Crack Tip Opening Displacement (CTOD)

By examination of fractured specimens, Wells noted that the faces of an initially sharp crack have moved apart before fracture, leading to a blunted crack, see Figure 2.2. He then proposed the opening at the crack tip as an alternative fracture mechanics parameter when LEFM is not valid. Today this parameter is known as CTOD (δ).
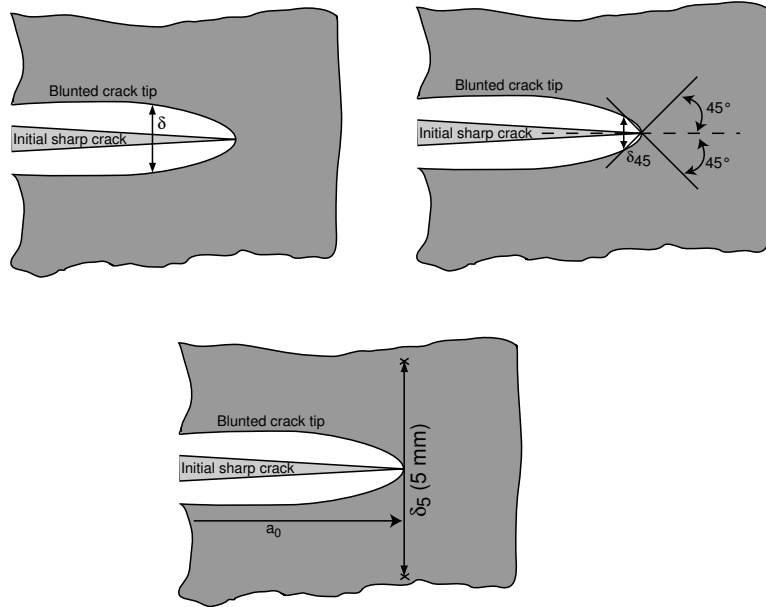
Figure 2.2: Definitions of Crack Tip Opening Displacement, δ, δ_{45} and δ_5

Different definitions of CTOD exist: δ, δ_{45} suggested by Shih [90] is generally used to measured CTOD in finite element calculations, and δ_5. δ_5 has been developed at GKSS research center [86]. δ_5, is measured between two points indented on a fracture mechanics specimen surface, as presented in Figure 2.2 [86]. The points are located 5 mm apart across the crack plane and perpendicular to the initial crack orientation at the crack tip. δ_5 is considered to be a "local" quantity as it is measured nearby the crack tip. In the case of sheet material characterisation δ_5 is preferred over other fracture parameters since it does possess the larger validity range in terms of acceptable crack extension, see the fracture resistance curve section. Moreover, δ_5 presents several advantages: for interface crack between two materials the influence of each material can be evaluated; the δ_5 measurements are different on each side of the interface. This feature is interesting in the case of fracture characterisation of weldments. Another advantage is that buckling of the tested specimens can also be evaluated by measuring δ_5 on both sides of the specimens.

J-integral

The second parameter that can characterise the crack tip under intense plasticity is the J-integral. The J-integral, first introduced by Rice [74], is a mathematical expression that expresses the energy input per unit of crack extension:

$$J = \int_s \{W\,dy - T_i \cdot \frac{\partial u_i}{\partial x} ds\}, \tag{2.4}$$

s being the contour along which J is determined. W is the strain energy: $W = \int_0^{\epsilon_{ij}} \sigma_{ij} d\epsilon_{ij}$, T is the traction vector and u a displacement vector, ds is a length increment. J is a line integral and Rice demonstrated that J is path independent, see also [16]. It can be demonstrated, see Rice [74], that J corresponds to the energy release rate in non-linear material and is then equivalent to G.

J can be experimentally determined from the force-displacement test records, it corresponds to the area under the curve. J is calculated using:

$$J = \frac{-1}{B} \frac{\partial U}{\partial a}. \tag{2.5}$$

For linear material behaviour at the crack tip a linear relationship exits between CTOD and the energy release rate: $G = m\sigma_0\delta$. Under those conditions the J-integral is equal to G, consequently a linear relationship exists between the J-integral and CTOD, see Eq. (2.6):

$$J = m\sigma_0\delta, \tag{2.6}$$

where m is dimensionless and a function of the stress state (plane stress or plane strain). This equation is valid under small scale yielding and Shih [90] further demonstrated that this relationship is unique for a given material. He analysed the displacements at the crack tip according to the HRR theory and related the displacements to J and the flow properties. Shih's relationship reads:

$$\delta_{45} = d_n(n, E, \sigma_0, I_n) \frac{J}{\sigma_0}. \tag{2.7}$$

Moreover, Hutchinson [48] and Rice and Rosengreen [75] demonstrated that J characterises the crack tip conditions in a non-linear elastic material. Considering a material behaviour of Ramberg-Osgood type, they found that *stress ∗ strain* varies as $1/r$ near the crack tip. It results that the distribution of stresses and strains at the crack tip can be expressed as:

$$\sigma_{ij} = \sigma_0 \left(\frac{EJ}{\alpha\sigma_0^2 I_n r} \right)^{\left(\frac{1}{n+1}\right)} \tilde{\sigma}_{ij}(n, \theta)) \tag{2.8}$$

$$\epsilon_{ij} = \frac{\alpha\sigma_0}{E} \left(\frac{EJ}{\alpha\sigma_0^2 I_n r} \right)^{\left(\frac{n}{n+1}\right)} \tilde{\epsilon}_{ij}(n, \theta)) \tag{2.9}$$

These two equations are nowadays called the HRR singularity and often serve as reference.

To account for the geometry dependency of the crack tip stresses, two additional parameters have been proposed: the T-stress for elastic material [113] and the Q-stress in the case of elastic-plastic material [67, 68]. The T-stress influences the shape of the plastic zone and the stresses deep inside the plastic zone. The Q-stress has been found by comparing results from finite element calculation with the HRR reference solutions. The Q-stress is

evaluated at a distance $r_c = 2J/\sigma_0$ from the crack tip along the ligament ($\theta = 0$) and is expressed as:

$$Q = \frac{\sigma_{\theta\theta}^{FE} - \sigma_{ij}^{HRR}}{\sigma_0}. \tag{2.10}$$

T and Q are comparable, when T is negative Q is also negative. A positive Q-stress enhances ductile void growth.

Fracture resistance curve

The fracture resistance curve (R-curve) represents the resistance to both stable and unstable crack extension of a statically loaded material. Since all the previously defined fracture parameters are compatible, they can be used to define the R-curve. The R-curve can therefore be expressed either as K, J or CTOD as functions of the crack extension, Δa. A multiple specimen technique or a single specimen technique can be used. During these tests, both the load and displacement are continuously recorded. In a multiple specimen technique, the specimens are loaded up to various load levels resulting in different crack lengths. The crack length is measured post test on the fracture surface of the broken specimens using multi-point weighted average method according to the GKSS EFAM GTP 02 testing procedure [86]. In a single specimen test, the crack length is measured either by optical method or by the unloading compliance or electrical potential drop techniques. J and K are calculated from the test data whereas the CTOD is recorded during the test using displacement gauge measurement. An advantage of the single specimen test over the multiple specimen one resides in the reduced amount of material needed.

The fracture resistance data serve as the basis for comparison, selection and quality assurance of materials [1]. Indeed, the K-based R-curve is employed by the aerospace industries to certify and select new alloys. They use a compliance method to calculate an effective crack size: the crack size is corrected to take into account the plasticity that develops at the crack tip. K is then calculated based on this effective crack length.

CTOD-δ_5 fracture resistance curves are particularly suited to characterise the fracture resistance in sheet material that exhibits extensive stable crack extension and reduced constraints compared to thicker material. Furthermore, it is also specially adapted in the presence of welds. As a local parameter, the strain gradient on the surface of the specimen can be monitored and no plastic zone size evaluation is required as in the ASTM E 561 standard [1]. In the presence of welds, the plastic zone size and shape differs from the one in a homogeneous material and up to now, no standard evaluation of the plastic zone size at a bi-material interface exists. Moreover, the linear relationship between J and δ is not valid anymore in the case of welded components [89]. In this configuration, the relationship becomes complicated due to the change in constraint induced by the weld geometry and the strength mismatch at the interface.

The validity ranges of the fracture resistance curves are defined by the standards [2, 1]. Within this range, the R-curve is size independent. Different criteria exist in terms of specimen geometry, J_{max}, δ_{max}, Δa_{max} .... For example, to determine the δ-R curve, the validity range is defined by $\delta_{max} = b_0/20$ and $\Delta a_{max} = 0.25b_0$ with $b_0 = W - a_0$ the initial specimen ligament.

Crack Tip Opening Angle (CTOA)

An alternative to the traditional fracture resistance curve is to plot the CTOA (Crack Tip Opening Angle) as a function of the crack length (Δa). After crack initiation, the CTOA values attain a plateau and stay constant for longer crack as no blunting takes place anymore. Therefore the CTOA is an option to characterise the fracture behaviour of sheet metals. A reference length must be defined, see Figure 2.3. Up to now no unique definition exists, some codes [86] suggest to use an average value of CTOA over a distance between 0.5 and 1.5 mm from the crack tip.
The CTOA is related to the δ_5 fracture resistance curve by

$$CTOA \approx \frac{d\delta_5}{d\Delta a}. \tag{2.11}$$

An advantage of the CTOA is that it is experimentally measurable on the specimen surface using optical methods. However, a large amount of pictures of the crack tip during the test have to be taken and high effort is required afterwards to analyse the pictures and determine the CTOA value optically as presented in Figure 2.3.
The CTOA can also be determined numerically (Figure 2.3b) and be used to simulate numerical crack extension using a node release technique (Figure 2.3c).
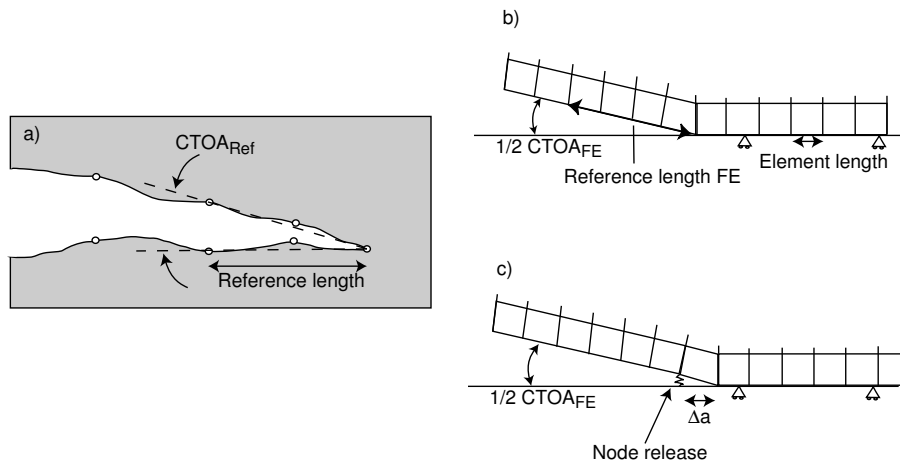
Figure 2.3: Definitions of Crack Tip Opening Angle: a) optical measurement, b) calculation in FE-model, c) crack extension simulation controlled by CTOA

Interface crack problem

Since the last decades, the amount of bi-material interfaces found in structures and components has increased principally due to the recent development of joining techniques and new mutli-material systems. The induced mismatch can result from different elastic properties (Young's modulus, Poisson's ratio . . .) or different plastic properties (yield strength, strain hardening exponent . . .) on each side of the interface. As a result, the stresses at the crack tip of an interfacial crack differ from those of a crack in a homogeneous material. At the interface, it is seen that the normal stresses (σ_{yy}) and shear stresses (σ_{xy})

are identical in the two materials, whereas the parallel stresses (σ_{xx}) can differ leading to different stress triaxialities ($\eta = \sigma_h/\sigma_{eq}$) and plastic zone sizes.

Shih and Asaro [91, 92, 93] studied the stresses ahead of the crack tip for two interface configurations: between an elastic and elastic-plastic material and between two elastic-plastic materials. Under small scale yielding, the stress field solutions are similar to the one established for mixed mode loading. They also observed that under fully plastified condition, at a given J value, the stress fields in the interface problems are similar to the one observed in homogeneous material, but more intense. Effectively, at a given J-integral value, the opening of the crack is larger in the interface case than in an homogeneous one, resulting in a larger plastic strain area.

In order to characterise the constraint resulting from the material mismatch, Zhang et al [117] proposed the introduction of an additional parameter, M. M is the maximum amplitude of the difference fields. The crack tip stresses can be identified by the so-called J-M theory as named by the previous authors:

$$\sigma_{ij} \approx \sigma_{ij}^{Ref}(J) + M\sigma_{0Ref}\tilde{f}_{ij}(\theta + 12\beta), \tag{2.12}$$

where $\beta = 0$ in case of overmatching and $\beta = 1$ for undermatched joint, σ_{0Ref} is the yield strength of the reference material and $\tilde{f}_{ij}^{M}$ is an angular function of the difference fields that has undergone a 12° shift.
Coupling of geometry and material constraints can be expressed by the J-Q-M theory.

In the case of interface crack, it is often observed that the crack follows a non-straight path. Different criteria exist to determine the direction of crack extension for linear elastic homogeneous materials. The mostly employed criteria are:

- the maximum opening stress criterion: The direction of cracking is perpendicular to the direction of maximum opening stress at the crack tip,

- the maximum energy release rate criterion: The direction of crack extension is the one that maximises the energy release rate,

- the mode I fracture criterion: the crack extends in the direction that maintains pure mode I fracture at the crack tip, i.e. $K_{II} = 0$.

The last approach by Cotterrel and Rice [27] has received much attention [61, 105]. They established the role played by the T-stress in the stability direction of a crack under small scale yielding and found that a crack is directionally stable if the T-stress is negative and directionally unstable if $T > 0$. Thus a positive T-stress favours kinking of the crack. Those criteria initially derived for homogeneous materials have been employed to characterise the crack direction of adhesively bonded joints [24].

2.2 Damage mechanics

In metals, the type of fracture (brittle or ductile) depends on mechanical and environmental conditions: strain rate, temperature, medium (air, vacuum, water . . .). However, under non-extreme conditions, most metals fracture in a ductile manner; the final rupture takes place after a considerable degree of deformation. In ductile fracture, large

deformation in the vicinity of a defect causes the formation of microcracks or microvoids (cavities). Defects such as inclusions, solution precipitates, piling up of dislocations, grain boundaries, triple points, etc are responsible for the formation of the cavities and are stress concentrators. Under the combined effect of increased plastic strain and hydrostatic tension, the formed microvoids grow and coalesce to form a macrocrack. A schematic of ductile damage and fracture is shown in Figure 2.4. Three coalescence mechanisms are sketched. If a single population of particles is present in the material, coalescence can take place by impingement or by shear band localisations: large dimples are formed and coalesce together. In modern alloys, several populations of particles of different sizes are present and dimples are formed around all types of particles. The second smaller dimples link the larger dimples together to form a void sheet mechanism, mechanism d3 in Figure 2.4. Each type of coalescence mechanisms can be found on the same fracture surface if the microstructure of the material is not homogeneous for example. Two fracture surfaces are presented in Figure 2.5: an Al-Al_3Ti alloy with a unique population of large dimples and a pressure vessel steel (20MnMoNi 55) that contains two populations of dimples.

Damage mechanics describes ductile fracture by the mechanisms of void initiation, growth and coalescence. Several classes of models exist, the two main groups are: micromechanically based models and phenomenological models. A review of the most utilised models is presented below. The two models employed in this work, namely the Gurson-Tvergaard-Needleman model and the cohesive zone model are more detailed at the end of the Chapter.

Micromechanically based damage models:

- Rice and Tracey model:
  Rice and Tracey [76] introduced in 1969 a potential that relates void growth to the dilatation rate of a spherical cavity located inside an infinite perfectly plastic material. The relationship is valid for high triaxiality only because the model assumes a spherical void and reads:

  $$\frac{dr}{r} = 0.283 exp\left(\frac{3\sigma_m}{2\sigma_0}\right)\dot{\epsilon}_{eq}^{pl} \tag{2.13}$$

  with r the radius of the void and $\dot{\epsilon}_{eq}^{pl}$ the equivalent plastic strain rate. This model does not consider the interaction between neighbouring cavities. Moreover, the Rice and Tracey model is not coupled: degradation of the material due to damage is not taken into account in the plastic potential.

  Huang [47] showed that the dilatation rate of a spherical void in an infinite perfectly plastic matrix is underestimated by Eq. (2.13) and he introduced a new evolution equation function of the stress triaxiality (η):

  $$\frac{dr}{r} = \begin{cases} 0.427\left(\frac{\sigma_m}{\sigma_0}\right)^{\frac{1}{4}} exp\left(\frac{3\sigma_m}{2\sigma_0}\right)\dot{\epsilon}_{eq}^{pl} & \text{for} \quad \frac{1}{3} \leq \eta \leq 1 \\ 0.427 exp\left(\frac{3\sigma_m}{2\sigma_0}\right)\dot{\epsilon}_{eq}^{pl} & \text{for} \quad \eta > 1 \end{cases} . \tag{2.14}$$

  In the case of strain hardening material, the yield strength σ_0 in Eq. (2.13) and Eq. (2.14) is replaced by the von Mises equivalent stress σ_{eq}. In that case, the void

a) inclusion in ductile matrix

b) void nucleation

c) void growth

d) void coalescence

Three mechanisms of void coalescence

d1) by impingement after [7]

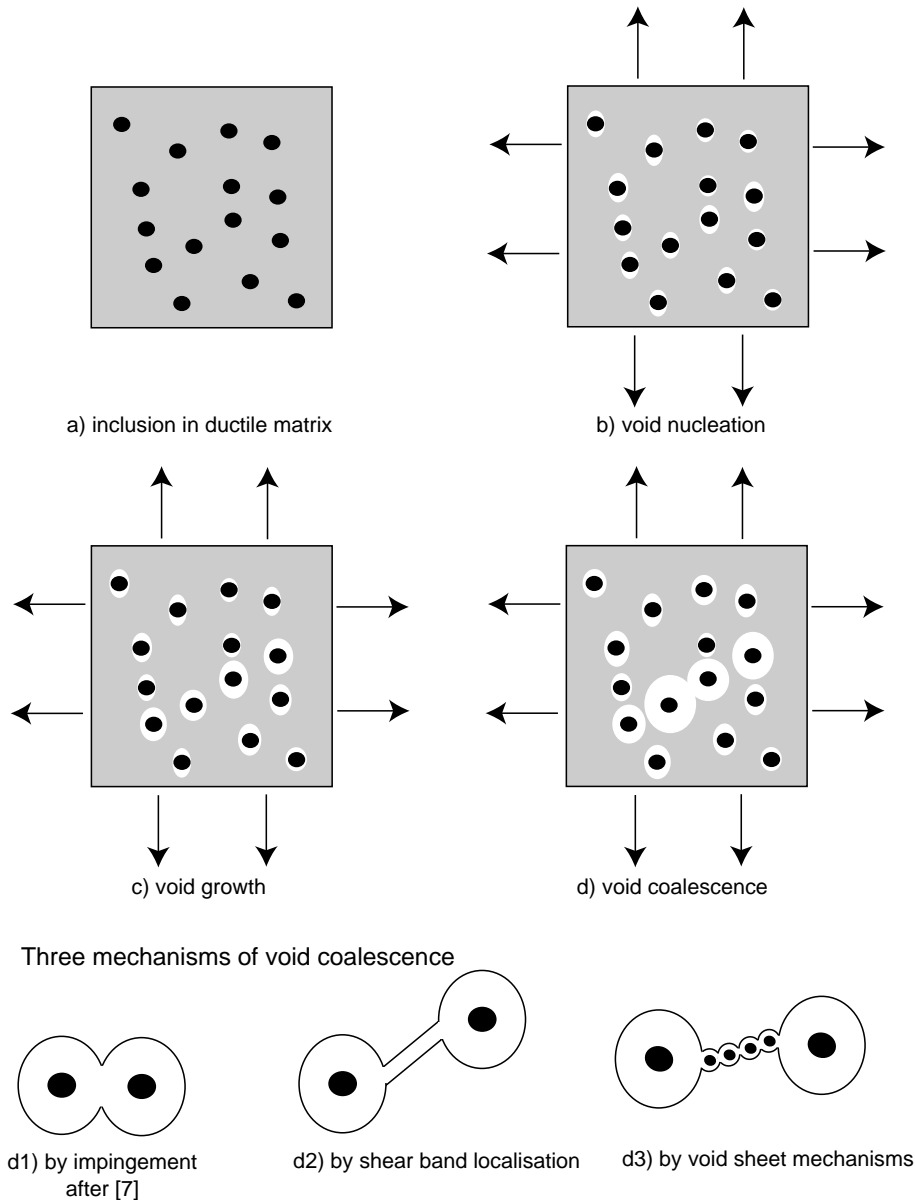d2) by shear band localisation

d3) by void sheet mechanisms

Figure 2.4: Void nucleation, growth and coalescence with various mechanisms of void coalescence

growth rate calculated by Eq. (2.13) compared to the one from the cell model is overestimated as demonstrated by Steglich [100]. Still, the Rice and Tracey model does not predict either the final failure nor the coalescence of voids.

- Gurson type models: see section 2.3

- Rousselier model:
  In the model from Rousselier [79], the damage is defined by a variable f function of the void volume fraction of the particles present in the material. Rousselier suggested in the case of damaged material that the stresses have to be corrected by the density of the material: $\tilde{\Sigma} = \dfrac{\Sigma}{\rho}$ and introduces $\tilde{\Sigma}$ into the plastic potential. The density ρ
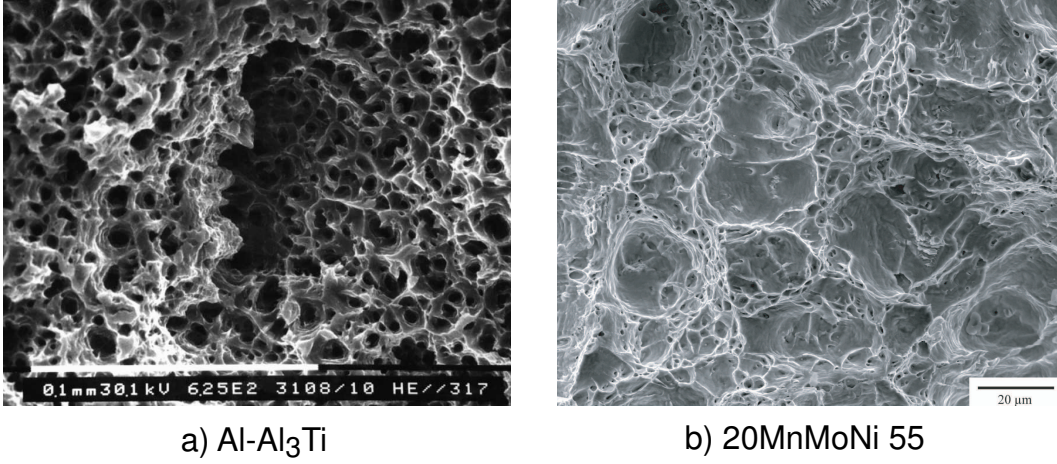
a) Al-Al$_3$Ti   b) 20MnMoNi 55

Figure 2.5: Ductile fracture facies with presence of dimples for Al-Al_3Ti reinforced material and 20MnMoNi 55 pressure vessel steel

is a function of the damage variable f: $\dfrac{\rho}{\rho_0} = \dfrac{1-f}{1-f_0}$. The plastic potential has been derived using thermodynamical considerations, similar to the CDM framework and reads:

$$\Phi = \frac{\tilde{\Sigma}_e}{(1-f)\sigma_M} + \frac{\sigma_1}{\sigma_M} f D \exp\left(\frac{\tilde{\Sigma}_{kk}}{\sigma_1(1-f)}\right) - 1 = 0 \tag{2.15}$$

with σ_1 and D material constants and σ_M the matrix stress. A uniform distribution of voids in the material is assumed. An advantage of the Rousselier model consists in the fact that even at high triaxiality, the shear component is not zero which permits to model perfectly the shear band localisation.

Phenomenological models:

- Continuum Damage Mechanics:
  Kachanov [50] and Lemaitre [56, 54] introduced the idea of Continuum Damage Mechanics (CDM) based on the effective stress concept: the strain response of a damaged volume of material is identical to the strain response of an undamaged volume submitted to the effective stress $\tilde{\sigma}$. $\tilde{\sigma}$ is defined as:

  $$\tilde{\sigma} = \frac{\sigma}{1-D}, \tag{2.16}$$

  D is a damage variable expressed at the macroscale that takes into account the material deterioration at the microscale, i.e. void, microcrack, decohesion...; $D = 0$ in the initial unstressed state and $D = D_c$ at failure. To complete the formulation of such model, a damage criterion, a plastic potential and the evolution of the damage variable D are required. CDM has been applied to simulate fatigue damage, ductile damage and creep damage, see the books of Lemaitre and Chaboche:"Mechanics of solids mechanics" [55] and "A course on damage mechanics" [56] for further details. Even if the CDM formulation is simple, a drawback of this method lies in the identification of the damage variable which is not straightforward. The measurement of

the damage D is indirect: i.e. measurement of density, acoustic methods, Young's modulus measurements ....

- <u>Cohesive zone model</u>: see section 2.4

2.3 Gurson type model

Gurson [44] used velocity fields identical to those of Rice and Tracey to develop a yield surface that accounts for degradation of the matrix material due to damage evolution. Gurson derived a yield surface for both an isolated cylindrical and a spherical cavity in a rigid perfectly plastic matrix of identical shape. The plastic potential reduces to the von Mises one when the damage, expressed by the internal variable, f, is zero. f is considered the void volume fraction. The material simulated by the Gurson model behaves as a continuum since the voids appear through their influence on the global flow behaviour. The material is also homogeneous, no clusters of particles as found in Al2024 T351 [71] can be properly simulated. The Gurson model is "coupled", because the evolution of the internal variable f influences the evolution of the stresses. The plastic potential for an isolated spherical void in a rigid perfectly plastic matrix is written as:

$$\Phi = \left(\frac{\Sigma_e}{\sigma_0}\right)^2 + 2f \cosh\left(\frac{\Sigma_{kk}}{2\sigma_0}\right) - 1 - f^2 = 0, \tag{2.17}$$

with σ_0 the matrix material yield strength, $\Sigma_{eq} = \sqrt{\frac{3}{2}\Sigma'_{ij}\Sigma'_{ij}}$ the macrocopic von Mises equivalent stress, Σ'_{ij} is the macroscopics stress deviator of the stress tensor Σ and $\Sigma_{kk} = 3\Sigma_m$ the trace of the macrosopic stress tensor Σ which can be expressed as three times the macroscopic hydrostatic stress. Similar to the Rice and Tracey model, the model was modified to simulate damage evolution in elasto-plastic strain hardening materials by introducing the current stress of the matrix σ_M instead of the material yield strength σ_0 in Eq. (2.17). The evolution of the plastic deformation is given by the normality rule:

$$\dot{\epsilon}^p_{ij} = \dot{\lambda}\frac{\partial\Phi}{\partial\sigma_{ij}}, \tag{2.18}$$

where the plastic multiplier $\dot{\lambda}$ is calculated using the consistency rule:

$$\dot{\Phi} = 0 = \frac{\partial\Phi}{\partial\sigma_{ij}}\dot{\sigma}_{ij} + \frac{\partial\Phi}{\partial f}\dot{f}. \tag{2.19}$$

To complete the formulation of the model, the current yield stress of the matrix is calculated at the macroscopic level using a linear relationship between the microscopic strain rate $\dot{\epsilon}^p_{ij}$ and the macroscopic strain rate $\dot{\epsilon}^p_{eq}$. The relationship reads:

$$\sigma_M\dot{\epsilon}^p_{eq} = (1 - f)\sigma_{ij}\dot{\epsilon}^p_{ij}. \tag{2.20}$$

The evolution of the porosity originates from two sources: the growth of existing voids and the nucleation of new voids that result either from the cracking or detachment of particles:

$$\begin{aligned} \dot{f} &= \dot{f}_{growth} + \dot{f}_{nucleation} \\ \dot{f}_{growth} &= (1 - f)\dot{E}_{kk} \\ \dot{f}_{nucleation} &= A\dot{\epsilon}^p_{eq} + B(\dot{\sigma}_M + \tfrac{1}{3}\dot{\sigma}_{kk}). \end{aligned} \tag{2.21}$$

In the case of damage evolution due to existing pores, $\dot{f}_{growth}$, the matrix material being incompressible, the variation of the total volume is due to the evolution of the void volume only (Eq. (2.21)).

The contribution resulting from the nucleation of new voids consists either of a strain controlled mechanism if $B = 0$ or of a stress controlled mechanism if $A = 0$. Chu and Needleman [25] proposed a normal distribution for strain-controlled nucleation:

$$A = \frac{f_N}{s_N \sqrt{2\pi}} \exp\left(-\frac{1}{2}\left[\frac{\epsilon_{eq}^p - \epsilon_N}{s_N}\right]^2\right), \quad B = 0. \tag{2.22}$$

f_N is the void volume fraction of the voids-nucleating particles, ϵ_N is the mean strain for nucleation (50% of the particles are void nucleating sites) and s_N is the corresponding standard deviation. Other forms of the distribution of A have been proposed: a constant rate of nucleation between a minimum and a maximum strain, for example [120]. The proposed distribution can then be:

$$A = \frac{f_N}{\epsilon_{final}^{pl} - \epsilon_{initial}^{pl}}. \tag{2.23}$$

For stress-controlled nucleation, the sum $\sigma_M + \frac{1}{3}\sigma_{kk}$ is an approximate value of the maximum normal stress acting on the particle/matrix interface [66, 114]. σ_N is the mean stress for nucleation and the expression holds:

$$B = \frac{f_N}{s_N \sqrt{2\pi}} \exp\left(-\frac{1}{2}\left[\frac{(\sigma_M + \frac{1}{3}\sigma_{kk}) - \sigma_N}{s_N}\right]^2\right), \quad A = 0. \tag{2.24}$$

Conducting FE calculations to analyse the bifurcation behaviour of a material containing a periodic array of cylindrical or spherical voids, Tvergaard [107, 106] found that the predictions obtained from Eq. (2.17) can be improved by introducing three new parameters - q_i - into the plastic potential. Tvergaard suggested to use $q_1 = 1.5$, $q_2 = 1.0$ and $q_3 = q_1^2$. Moreover, in the original Gurson formulation Eq. (2.17) the total loss of stress carrying capacity occurs when $f = 1/q_1$. Experimental and numerical works have shown that this value is much too high. Needleman and Tvergaard [111] have introduced a "coalescence" criterion via the modified damage variable, $f^*(f)$:

$$f^* = \begin{cases} f & \text{for} \quad f \leq f_c \\ f_c + \kappa(f - f_c) & \text{for} \quad f > f_c \end{cases}, \quad \kappa = \frac{f_u^* - f_c}{f_f - f_c}. \tag{2.25}$$

κ accelerates numerically the damage evolution after the critical void volume fraction, f_c, has been reached. The material has lost its stress carrying capacity when $f_u^* = 1/q_1$, the void volume fracture at fracture. Considering the two previous improvements, the newly developed potential is:

$$\Phi = \left(\frac{\Sigma_e}{\sigma_M}\right)^2 + 2q_1 f^* \cosh\left(\frac{q_2 \Sigma_{kk}}{2\sigma_M}\right) - 1 - (q_1 f^*)^2 = 0. \tag{2.26}$$

This formulation, named hereafter the GTN-model, is used in Chapters 4 and 5 to simulate crack extension in aluminium laser welds.

Recent developments of the Gurson model

The use of Gurson type models has considerably increased in the last decades to numerically simulate damage evolution. As a consequence, extensions of the original formulation have emerged. Those modifications can be assembled into two main groups: improvement in the modelling of the plastic flow behaviour and modifications of the plastic potential, to consider the void shape effect or the coalescence of voids.

Three main extensions of the modelling of the plastic flow behaviour of the matrix material are noted:

- Viscoplasticity: in the plastic potential the matrix stress σ_M is dependent on both the plastic strain ϵ_{pl} and the plastic strain rate $\dot{\epsilon}_{pl}$ and Eq. (2.26) remains unchanged. This modification has been successfully used by Brocks et al [15] to simulate ductile tearing resistance of a pressure vessel steel.

- Kinematic hardening: Isotropic hardening is not sufficient to describe the hardening behaviour of the material under cyclic and non-proportional loading. Kinematic hardening is introduced to characterise the shift of the center of the yield surface. However, the proposed extension can be applied only under low cycle fatigue because the Gurson model is not able to describe the damage mechanisms occurring during fatigue loading. Ristinmaa [77], Steglich and Pirondi [101] have used the modified formulation. Mühlich has implemented the kinematic hardening Gurson formulation as a user-material subroutine within ABAQUS [63].

- Plastic anisotropy: To consider the plastic anisotropy of the material due to processing methods, for example, the equivalent von Mises stress in Eq. (2.26) can be replaced by an anisotropic effective stress $\bar{\sigma}$. $\bar{\sigma}$ can be determined either from the Hill anisotropy model ($\bar{\sigma} = \sqrt{\frac{3}{2}h_i\sigma'_i\sigma'_i}$ with $h_{i=1-6}$ describing the sheet anisotropy) or from advanced models derived for a particular material as Bron and Besson [17] did in the case of aluminium alloys based on Barlat's anisotropy model [4].

Void shape considerations

In the GTN-model, the voids are spherical at the beginning of the simulation and stay spherical as loading takes place. Those two assumptions are questionable. Inclusions or second phase particles in materials are mostly non spherical as for example the MnS inclusions in steel. Moreover, unit cell calculations have demonstrated that this assumption is valid only for a stress triaxiality ratio ($\eta = \sigma_h/\sigma_{eq} \geq 1.5$), for small triaxiality, an initially spherical void will evolve in a prolate form whereas at elevated triaxiality the final shape is oblate. These observations have led to employ the parameter q_2 as a function of the void aspect ratio [6] since q_2 regulates the influence of the hydrostatic pressure.
Based on these considerations, Gologanu [39, 40] has modified the yield function proposed by Gurson to account for the shape of the voids. Spheroidal voids are introduced into a confocal spheroid matrix being a rigid-perfectly plastic von Mises material. The spheroidal cavity can be either prolate or oblate with the void shape parameters $W = R_z/R_r$ and $S = \ln W$. R_r and R_z are the semi-minor axis (smallest half axis) (resp. semi-major) and semi-major (largest half axis) (resp. semi-minor) axis of a prolate (resp. oblate) void.

The yield surface formulation holds:

$$\Phi = \frac{C}{\sigma_0^2}(\Sigma_{zz}-\Sigma_{xx}+\varpi\Sigma_h)^2+2q(g+1)(g+f)\cosh\left(\kappa\frac{\Sigma_h}{\sigma_0}\right)-(g+1)^2-q^2(g+f)^2 = 0, \quad (2.27)$$

with $\Sigma_h = 2\alpha_2\Sigma_{xx} + (1 - 2\alpha_2)\Sigma_{zz}$ and q the parameter introduced by Tvergaard. g is defined by Gologanu [41] as a fictitious porosity obtained by replacing the real spheroidal void by a spherical one with radius equal to the focal distance, $g = 0$ for a prolate void. The parameters C, ϖ, κ and α_2 are functions of the shape of the void. A full description of the parameters is given by Pardoen and Hutchinson [70]. The potential reduces to the Gurson one when $S = 0$. Evolution solutions have also been developed for f and S. $\dot{f}$ is identical as in the Gurson model and $\dot{S} = f(\dot{E}, h_i)$.

Coalescence criteria

It has been shown that the third stage of damage evolution consists of the coalescence of voids. In the GTN-model, the volume fraction of particles at which coalescence occurs is imposed by the parameter f_c. However the coalescence stage is a function of the void shape, inter-particle spacing and loading conditions that are not considered by f_c. Brown and Embury suggested that coalescence of voids takes place when the diameter of the deformed voids equals the distance between the two neighbouring void centers.
Thomasson [103] proposed a more rigorous criterion for void coalescence. The criterion says that coalescence occurs when a plastic limit load is attained. This limit corresponds to an equilibrium load between the homogeneous and the localised deformation modes. Pardoen and Hutchinson [70] developed an expression including the void aspect ratio. For axisymmetry geometries, the average normal stress acting on the cell at the onset of localisation is:

$$\frac{\sigma_z}{\sigma_f} = \left[1 - \left(\frac{R_r}{L_r}\right)^2\right]\left[\alpha\left(\frac{R_z}{L_r - R_r}\right)^{-2} + \beta\left(\frac{R_r}{L_r}\right)^{-\frac{1}{2}}\right] \quad (2.28)$$

with σ_f the effective matrix flow stress, R_r, R_z are the two axes of the void and L_r is the radial axis of the confocal matrix. $\alpha = 0.1$ and $\beta = 1.2$ have been fitted by Thomasson and those values have been used by Zhang [120]. However, Pardoen and Hutchinson [70] found by comparison with FE analysis that $\beta = 1.24$ and α is function of the strain hardening of the material.

2.4 Cohesive Model

Since "infinite" stresses at the crack tip as predicted by the K-field are non-physical, modifications like the "effective crack length" of Irwin [49] or the "strip yield model" of Dugdale [32] and Barenblatt [3] have been introduced. The latter becomes the fundamental idea of the cohesive model. Dugdale and Barenblatt assumed that a crack is composed of two parts: a stress-free part and a part that is loaded by cohesive stresses. For Dugdale, the cohesive stress equals the yield strength (σ_0) of the material whereas for Barenblatt, the cohesive stress is function of the ligament coordinates: $\sigma(x)$ (x being the distance from the crack tip). The stress free part is modelled as a continuum that behaves according

to the J_2 plastic flow theory. The second part is simulated using interface elements and represents any fracture mechanisms. The principle of the cohesive model is sketched in Figure 2.6.
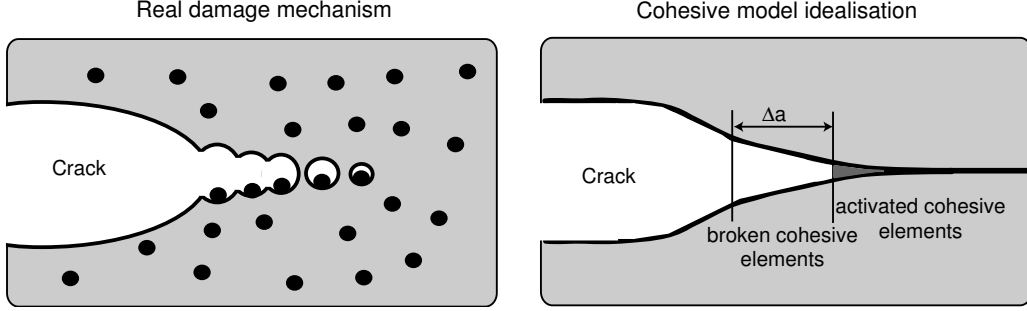

Figure 2.6: Schematisation of the cohesive zone model

The cohesive models that followed the "strip yield model" differ from the idea of Barenblatt, the traction acting on the ligament is a function of the crack opening $\sigma(\delta)$ and not of the distance from the crack tip $\sigma(x)$. Hillerborg [46] was the first to implement the cohesive model in a FE-code by simulating fracture in brittle materials. Ten years later, Needleman [64] applied the cohesive model to study crack extension in ductile materials.

The cohesive elements have no thickness and possess four nodes in 2D and eight nodes in 3D. They behave according to a cohesive law or traction-separation law (TSL): a relationship between the opening of the cohesive elements and the cohesive stress: $T(\delta)$. The cohesive elements open when damage takes place and loose their stress carrying capacity at final fracture. The separation δ of the interface elements results from the displacement jump between the two surfaces of the element:

$$\delta = u^+ - u^-. \tag{2.29}$$

The separation can be in a normal (δ_N) or/and in a shear (δ_T) mode. In mixed mode case, when both normal and tangential separations are activated, the normal traction influences the tangential one and vice versa. Under pure mode I fracture, the separation of the cohesive elements is only normal and $\delta_T = 0$. The elements are totally separated or broken when the displacement jump attains a critical value: δ_0.

The second parameter controlling the cohesive law is the traction of the cohesive elements. After the maximum traction, T_0, has been reached the cohesive elements start to loose their stress carrying capacity. In the case of mixed-mode, both normal and tangential tractions (resp. T_N and T_T) are activated.
A third parameter can be calculated from the two previous ones: the cohesive energy: Γ_0. The cohesive energy is the work dissipated by the cohesive elements and corresponds to the area under the $T(\delta)$ curve:

$$\Gamma_0 = \int_\delta^{\delta_0} T(\delta)d\delta = \alpha T_0 \delta_0. \tag{2.30}$$

with α varying between 0.5 and 1.0 for most metals.

Different forms of the TSL have been proposed. They are all characterised by:

- the two parameters introduced previously: T_0 and δ_0,

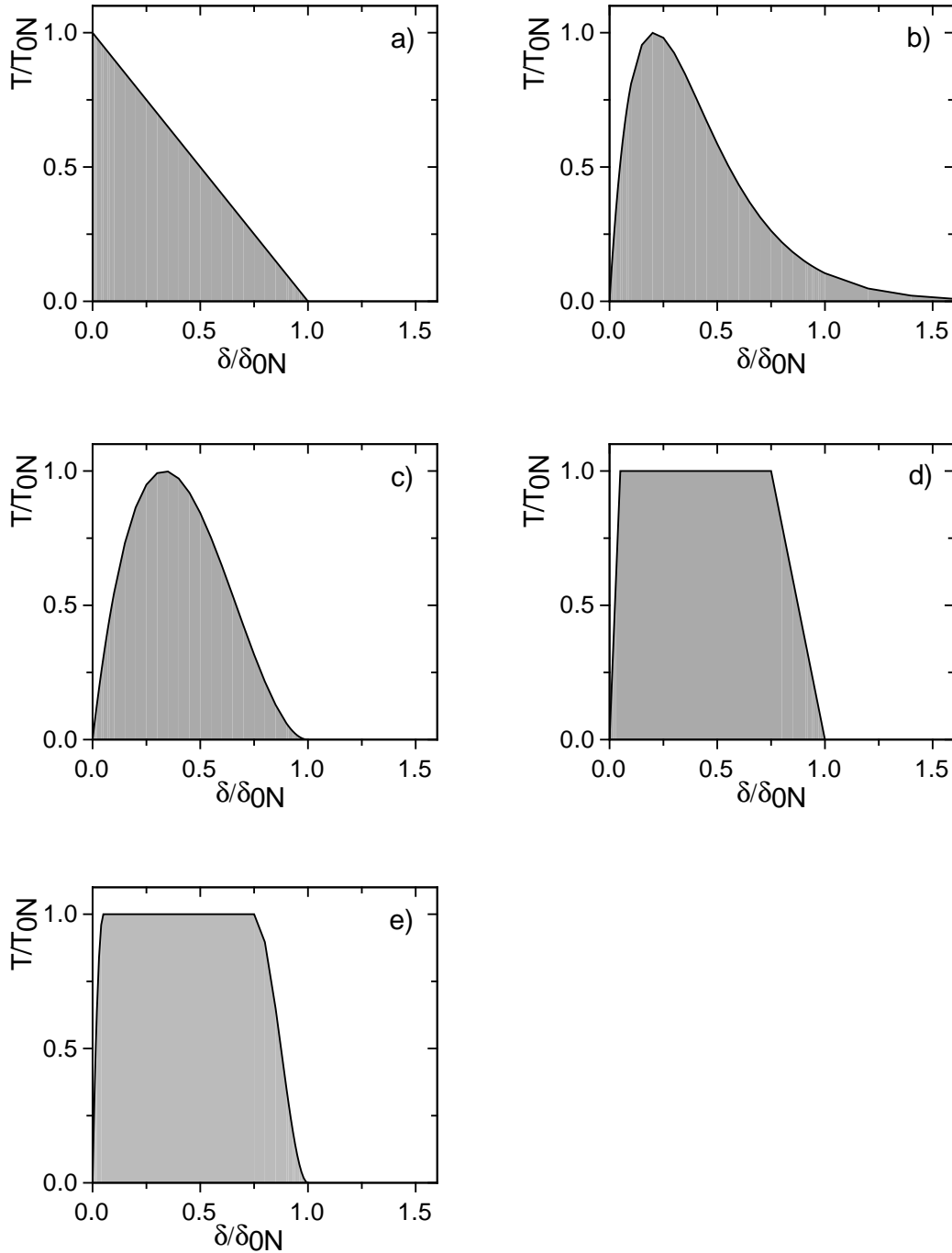- at total failure, when the critical separation δ_0 is achieved, the traction is zero.

Figure 2.7: Shape of the traction separation laws: a) from Hillerborg [46], b) from Rose et al [78, 65], c) from Needleman [64], d) from Tvergaard and Hutchinson [109] and e) from Scheider [81]

Some of the TSL proposed in the literature are displayed in Figure 2.7 for pure mode I (T_N

and $T_T = 0$). The equations that define the traction separation laws, presented in Figure 2.7, are reported in [14]. Hillerborg [46] proposed a linearly decreasing potential. This kind of shape, Figure 2.7a, is mostly used for brittle materials, such as in concrete or rock. For concrete, bilinear functions also exist. An exponential form of the traction-separation law, Figure 2.7b, based on atomistic analyses of interfacial separation, has been proposed by Rose et al [78] and further developed by Needleman [65]. When the separation δ reaches the critical value δ_0, the cohesive elements have not totally lost their stress carrying capacity and $T_N/T_0 = 0.105$. Needleman [64] derived a traction $T(\delta)$ which is polynomial of degree three, Figure 2.7c. The maximum traction T_0 is reached at $\delta_N = \delta_0/3$. Tvergaard and Hutchinson [109] have proposed a trilinear function introducing two additional parameters: δ_1 and δ_2, as shown in Figure 2.7d. This function is not necessary differentiable which could lead to numerical complications. Lin et al [58] have used a special case of Figure 2.7d assuming $\delta_1 = 0$ and $\delta_2 = \delta_0$. Recently, Scheider proposed a cohesive law plotted in Figure 2.7e which is a generalisation of the models from Lin, Needleman and Tvergaard and Hutchinson. This form is described in the following as it is used in Chapter 6 to simulate the crack extension in an aluminium laser weld.

The model of Scheider considers both normal and tangential separations and has been extended to 3D analyses. This cohesive law has been implemented as a user-element subroutine within the commercial program ABAQUS.

The dependence of the normal traction on tangential traction and vice versa are expressed by the following equations:

$$
\begin{aligned}
T_N &= T_N(\delta_N, \delta_T) = T_{0N} f(\delta_N) g(\delta_{Tmax}) \\
T_T &= T_T(\delta_N, \delta_T) = T_{0T} f(\delta_T) g(\delta_{Nmax})
\end{aligned}
\tag{2.31}
$$

The functions $f(\delta)$ and $g(\delta)$ are given below. f(δ) contains two additional parameters, δ_1 and δ_2, compared to the previously described laws, that characterise the stiffness of the cohesive element and the start of the decrease of traction leading to total failure of the elements, respectively. The influence of the choice of the two parameters δ_1 and δ_2 is studied in Chapter 6. The functions $f(\delta)$ and $g(\delta)$ are:

$$
f(\delta) = \begin{cases}
2\left(\dfrac{\delta}{\delta_1}\right) - \left(\dfrac{\delta}{\delta_1}\right)^2 & \text{for} \quad \delta < \delta_1 \\
1 & \text{for} \quad \delta_1 < \delta < \delta_2 \\
2\left(\dfrac{\delta - \delta_2}{\delta_0 - \delta_2}\right)^3 - 3\left(\dfrac{\delta - \delta_2}{\delta_0 - \delta_2}\right)^2 + 1 & \text{for} \quad \delta > \delta_2
\end{cases}
\tag{2.32}
$$

$$
g(\delta) = 2\left(\frac{\delta}{\delta_0}\right)^3 - 3\left(\frac{\delta}{\delta_0}\right)^2 + 1
\tag{2.33}
$$

For pure normal separation or tangential separation, the cohesive energy is determined based on:

$$
\Gamma_0 = \alpha T_0 \delta_0 \qquad \text{with} \qquad \alpha = \frac{1}{2} - \frac{1}{3}\frac{\delta_1}{\delta_0} + \frac{1}{2}\frac{\delta_2}{\delta_0}
\tag{2.34}
$$

The cohesive elements proposed by Scheider [81] account for local unloading. Local unloading can be achieved through a global unloading of the component or in the case of

multiple microcracks. The terms loading and unloading of the cohesive elements can be defined as: "loading and unloading are used in the sense of increasing and decreasing separation, respectively". Decrease of the traction with increasing separation after the maximum traction has been reached will be called softening hereafter. In ductile material, any reduction of the separation is elastic as characterised by the initial elastic stiffness as observed for example during a tensile test when unloading occurs. As a consequence, Scheider set the slope of the unloading curve parallel to the initial stiffness of the cohesive element (part of the TSL until δ_1, see Figure 2.7e. Moreover, he defined unloading of normal and tangential tractions separately. Numerically, the equations that govern the unloading of the cohesive elements are:

$$\begin{aligned} T_N = T_N(\delta_N, \delta_T) = T_{0N} f^*(\delta_N) g(\delta_{Tmax}) \\ T_T = T_T(\delta_N, \delta_T) = T_{0T} f^*(\delta_T) g(\delta_{Nmax}) \end{aligned} \tag{2.35}$$

with

$$f^* = \begin{cases} 2\left(\dfrac{\delta - \delta_{max}}{\delta_1}\right) + \dfrac{T^N_{max}}{T_0} & \delta < \delta_{max} \\ f & \delta > \delta_{max} \end{cases} . \tag{2.36}$$

The "ductile" unloading behaviour for both normal and tangential separations is displayed in Figure 2.8. Unloading of the element starts at point A. The separation δ reached at point A corresponds to the maximum separation attained so far: δ_{Nmax} and δ_{Tmax} for normal and tangential separations, respectively.
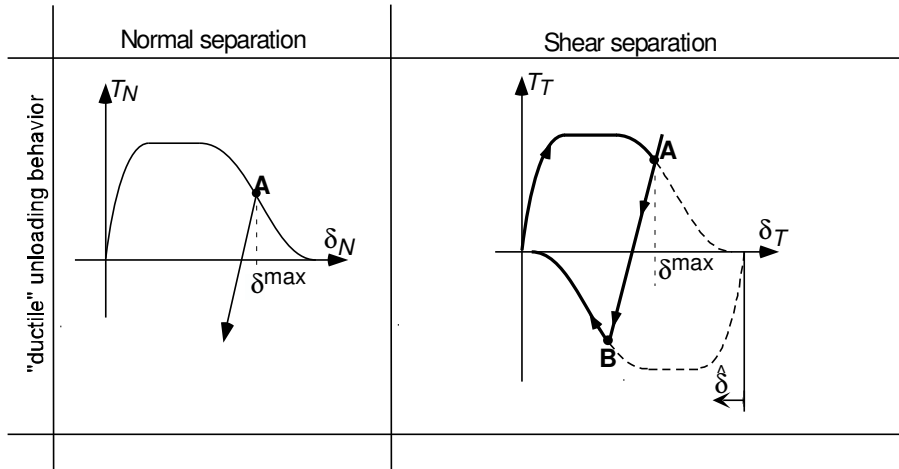

Figure 2.8: Unloading of the cohesive elements in ductile materials after [81]

Due to the nature of the cohesive elements as interface elements, the cohesive model is particularly adapted to simulate crack extension at an interface between two materials. Several authors have used a traction-separation law formulation to study the toughness of the interface between two elastic-plastic materials [108], two elastic substrates joined by a ductile layer [110], in composite materials [23] and in graded material [23]. In these various cases, the cohesive law that governed the interface contains both normal and tangential separations since at the crack tip, a pure normal opening stress is questionable.

The two models used in this work have been reviewed, namely the GTN-model and the cohesive law from Scheider. Both models have been selected for their relative "simplicity"

in simulating crack extension of homogeneous and welded sheet materials, compared to their respective extensions described above.

Chapter 3

Characterisation of Al6056 T78 laser beam weld

The aluminium, known since the beginning of the 19th Century, had received little interest until the simultaneous discovery of the electrolytic process for smelting aluminium in 1886 by P. Hèroult in France and C. Hall in the United States. This electrolytic process combined with the extraction of alumina from the ore bauxite (attributed to K. Bayer), is still used nowadays, and has promoted the expansion of aluminium. Further developments of aluminium took place after the discovery of age-hardening by A. Wilm who produced an aluminium-copper alloy known as Duralumin that possesses an increased tensile strength compared to pure aluminium.

Due to both the available quantity of aluminium on earth and its properties, aluminium has been, since this time, subject to a rapid growth and is nowadays used in various domains such as architecture, transport industries and packaging; packaging representing today the main market. The low density of aluminium is an asset for the transportation industry and particularly in aeronautics. Back to 1903, the Wright Bothers used an aluminium copper casting for the crankcase of their engine. Since then the aeronautical industry has driven the development of high strength aluminium alloys. Their main requirements are: high strength, corrosion resistance, durability, damage tolerance, low costs (both manufacturing and maintenance) ... [60, 99]. Heat-treatable alloys are often employed in this field: the 2xxx series (Al-Cu alloys) and 6xxx series (Al-Mg-Si alloys) are used for fuselage application where fracture toughness is the definite property, whereas 7xxx series (Al-Zn-Mg alloys) are used for aircraft wings where elevated strength is needed [33, 99].

Since the last decade, the 6xxx aluminium alloys are emerging and are of interest to both the automotive and the aeronautical industries as these alloys possess medium to high strength, good formability and good weldbality [43, 11]. The automotive industry is interested in their improved formability since complex shapes can be produced by sheet metal forming [62] whereas the good weldability might permit the aeronautical industry to reduce both weight and manufacturing costs compared to the traditional riveting techniques used in most aircrafts. However, one question remains open: does a welded joint serve as crack arrest similarly to a rivet?

Al6056 and Al6013 are considered as potential replacement alloys for the Al2024 traditionally used in fuselage panels; whose microstructure and properties are well documented

in the aluminium Handbook [28]. Al6056 and Al6013 possess a similar composition, the limits of chemical composition are given in Table 3.1, and they are produced by Pechiney (France) and by Alcoa (US), respectively. In those alloys, copper is added to enhance precipitation hardening [87], and therefore an improved strength is obtained.

	Si	Mg	Cu	Mn	Fe	Zn	Zr	Al
Al6056	0.7 - 1.3	0.6 - 1.2	0.5 - 1.1	0.4 - 1.0	< 0.5	0.1 - 0.7	0.07 - 0.2	Bal.
Al6013	0.6 - 1.0	0.8 - 1.2	0.6 - 1.1	0.2 - 0.8	0.5	0.25	0.05	Bal.

Table 3.1: Nominal composition of Al6056 and Al6013 (in weight %)

These two alloys are available in three age-conditions: T4 (naturally aged), T6 (peak aged) and T78 (overaged). Precipitation hardening in Al-Mg-Si alloys occurs through variants of β-Mg_2Si (fcc) and when Cu is added, as in Al6056, additionally through variants of λ or Q-$Al_5Cu_2Mg_8Si_6$ (hcp). The basic precipitation sequence in Al-Mg-Si alloys
GP zones $\rightarrow \beta'' \rightarrow \beta' \rightarrow \beta$ is then modified as
GP zones $\rightarrow (\beta'' + Q') \rightarrow (\beta' + Q) \rightarrow (\beta + Q)$.
The hardening on natural ageing in T4 occurs mainly by GP zones. The maximum in hardening is achieved in the peak aged condition T6 when mostly the needle shaped precipitates (β'') form, the extent of hardening decreases on overageing when lath or rod (β' or Q' or both), and plate shaped precipitates (β or Q or both) form [53, 34, 43]. Depending on the composition and on the temper, a mixture of metastable precipitates occurs in commercial alloys. Since such precipitates are partly coherent, in particular β'' and Q', depending on their size and orientation they may be sheared or by-passed during deformation. Despite the loss of strength and ductility following a T78 heat treatment, this temper is favoured to obtain improved intergranular corrosion resistance [30].

The microstructure of Al6056 is typical of the one of Al6xxx alloy. Two populations of large inclusions ($d > 1 \ \mu$m) and a single population of dispersoids ($0.1 < d < 1 \ \mu$m) exist. The large particles consist either of an intermetallic phase Mg_2Si or of an α-phase that is Fe-rich and contains (Al, Fe, Mn, Si). The α-phase is arranged in interdendritic channels and small dispersoids [31]. The small dispersoids contain Al-Mn-Si. High damage localisation has been observed around the coarse particles [37]. These particles can either fracture or debond from the matrix, depending on their size, morphology, etc...

One advantage of aluminium alloys and particularly of the 6xxx series resides in its weldability as any welding process may be employed. Al6xxx can be joined by non-conventional welding techniques such as Laser Beam Welding (LBW) and Friction Stir Welding (FSW). One great interest in these techniques results from the possible production of welds of similar or dissimilar materials with high quality [21, 20]. Moreover, the low energy density introduced into the workpiece during laser welding allows the formation of narrow fully penetrating welds. The reduced size of the weld helps limiting the inherent problems linked with power beam welding: microstructure changes, porosity formation due to gas entrapment, crack sensitivity (hot tearing and liquation cracking) and degradation of the tensile properties in the weld and heat affected zone (zone thermally affected by the welding process) [12].
The LBW process is also considered cost effective in spite of the elevated investment re-

quired when buying the equipment. Indeed high productivity rate can be achieved due to the ease of automation. High travel speed (in sheet metal > 1 to 10 m/min) and deep penetration weld by single pass can be achieved. Nevertheless, one difficulty resides in the material preparation (oxides have to be removed) and in the workpiece alignment in order to create the keyhole.

The laser produces a light energy that is absorbed by the material and converted to heat energy. The principle of the laser welding is sketched in Figure 3.1. The laser beam is focussed by an optics in order to obtain a beam of high power density and a small spot size to limit the size of the fusion zone. As the beam enters in contact with the material, metal vapor is produced and the material starts to melt. If the energy density is high enough keyholing takes place that allows deep penetration of the laser beam and melting of the material around the beam. Then the two materials mix as the temperature obtained in the keyhole is higher than the melting point of the respective materials. On the advancing side of the weld, this process takes place continuously whereas on the back side, the fused material solidifies quickly producing the weld. As a consequence, the weld metal is a combination of the two metals that have been welded; its microstructute is that of a casting since no additional rolling is applied.

Two sources are available for the laser beam: a solid state laser Nd:YAG or a gas laser CO_2. The Nd:YAG laser is made of a solid state yttrium aluminium garnet which is doped with neodynium. The CO_2 laser is constituted of CO_2, N_2 and He. Helium is used to suppress the plasma in order to avoid any loss of alloying elements (Mg loss in Al 6xxx alloys). The CO_2 laser is often used to weld high thickness material and steel as the beam quality and the beam power delivered to the workpiece are higher than with Nd:YAG laser. However, Nd:YAG laser could be favoured in the case of aluminium alloys since the absorption of the light by an aluminium alloy is higher for a YAG laser than for a CO_2 laser.

Laser beam welding does not necessarily require the use of filler material, however filler material can be employed to optimise the weld metal composition and therefore the weld metal properties. This is the case for aluminium 6xxx series in which the loss of strength in the heat affected zone (HAZ) can attain 50%. The selection of a proper filler material is therefore essential. For the Al6xxx alloys, two types of filler materials are recommended: Al-Si or Al-Mg alloys with a nominal content of 5% of the alloying element [38]. Nevertheless, filler materials rich in silicon are preferred since it produces lower porosity welds and limited decrease of tensile strength in both the FZ and HAZ than filler material rich in magnesium [19, 12, 13].

In this work, similar sheets of Al6056 T4 have been welded by the Institut de Soudure (Roissy, France) using a CO_2 laser beam weld to form the butt joints. An AlSi12 (4047) filler material is used to achieve the minimum loss of strength of the weld. The two sheets are 6 mm thick. The weld direction is parallel to the rolling direction. A post weld heat treatement T78 has been applied after welding to regain some strength in the HAZ. Characterisation of the weld is carried out in terms of microstructure (section 3.1), mechanical characterisation (section 3.2) and fracture toughness (section 3.3).
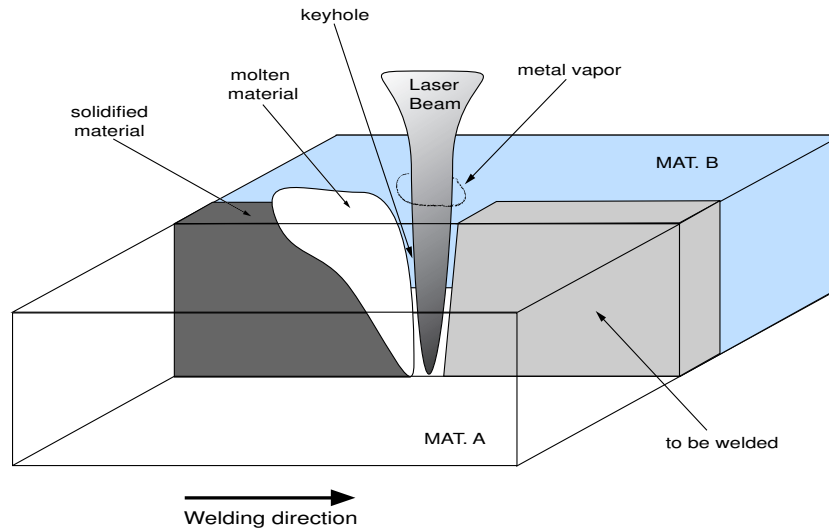
Figure 3.1: Principle of laser beam weld process

3.1 Microstructure of Al6056 T78 LBW

The laser beam seam generates a localised heating of the joint. Around the weld pool, the temperature gradient and the variation of solidification due to different cooling rates lead to different microstructure and metallurgical properties of the weld. Moreover, this new "microstructure" is also function of the process parameters such as: the use of a filler material, the choice of the incident laser beam (power, diameter), the speed of the laser beam across the substrate surface and the absorptivity of the aluminium alloys [28, 19].

The microstructure of the laser weld is investigated using polished specimens under optical microscope (OM) and scanning electron microscope (SEM). Some specimens have also been etched using a Flick etchant to reveal the grain morphologies. The pictures are taken in the plane ST which is relevant for fracture toughness characterisation.

A cross section of the Al6056 T78 laser beam weld is presented in Figure 3.2. Three main regions are visible: the fusion zone (FZ), the heat affected zone (HAZ) and the base material (BM). The fusion line: the boundary between the FZ and the HAZ is black and clearly apparent in the picture. The FZ, location of the fusion process, contains no apparent macroscopic porosity. Moreover, the weld is fully penetrated as the FZ extends across the entire sheet thickness. The fusion zone has a crater shape. Both ends of the weld being polished, the exact shape of the weld root and weld toe is not visible. The quality of the weld is therefore judged good. The HAZ is found on both sides of the fusion zone and results from the degradation of the base material properties. The resulting microstructure in the heat affected zone is thermally dependent. Outside the HAZ the unaffected BM is found.

Al6056 T78 base material

The microstructure of the Al6056 T78 base material is typical of that of 6xxx series aluminium alloys series, see Figures 3.2 and 3.3c. The base material possesses two populations of coarse particles and a population of dispersoids. Figures 3.4a and b show the base metal microstructure at two different magnifications. Figure 3.4b is unclear due to the high magnification employed. Nevertheless, the dispersoids are visible and correspond to the smaller white objects. The dispersoids are of the order of magnitude $0.1 < diameter < 1$ μm and the particles are larger than one micron.

The chemical composition of each type of constituents is determined by EDX analysis, see Table 3.2. The locations at which the measurements have been taken are indicated in Figure 3.4 by the numbers. The large particles are Fe-rich phase (Al, Fe, Mn, Si and Cu) and Mg_2Si-particles. The Fe-rich phase can be identified as the α-phase of Al-Mg-Si aluminium alloys. The intermetallics Mg_2Si are round whereas the α-phase possesses a variety of shapes. Under OM, the different constituents appear with different colours: the Mg_2Si particles are black whereas the FE-rich particles are dark grey and the matrix appears light grey. Since the Mg_2Si-particles are easily recognisable and their content is low their composition was not determined by EDX analysis. The smaller dispersoids are composed of Al, Mn and Si.

The grains in the BM are elongated due to rolling of the casting to achieve the required thickness with an aspect ratio (length/width) equals to 4.

Al6056 T78 fusion zone

In the studied Al6056 T78 the microstructure of the weld metal is not uniform. At the top, in the middle of the FZ, equiaxed grains (called epitaxial grains) are visible whereas the remaining part of the FZ contains columnar grains. These columnar grains are recognizable at the FZ/HAZ interface, see Figure 3.2. The presence of the two types of grains is due to the solidification process. Solidification processes in casting and in welding are similar. As the metal in the weld pool starts to solidify, epitaxial growth, as a primary growth, takes place. As the solidification process continues, the grains at the fusion zone boundaries grow parallel in a "predefined" orientation to form columnar grains whereas in the middle of the fusion weld, branches grow independently in an equiaxed fashion.

This type of microstructure in the weld with two populations of grains is typical of aluminium alloy welds and results from the combined effect of the high heat input and high welding speed producing a heterogeneous nucleation within the weld pool.

The dendritic structure of the weld metal, displayed in Figure 3.3a and in Figure 3.4c at two magnifications, is typical of that of a cast aluminium alloy that contains around 12 % silicon, [28]. The filler material used is AlSi12 and therefore the content of silicon is higher in the FZ than in the base material. Variation of the interdendritic arm spacing is visible but no measurements have been realised to determine this difference. Small particles nucleate around the dendritic arms. The composition of both the particles and the matrix in the FZ have been determined by EDX analyses. The results are presented in Table 3.2 and the locations of the measurements are displayed in Figure 3.4.

Al6056 T78 heat affected zone

The bounadry between the fusion zone and the heat affected zone is clear. The heat affected zone possesses microstructural features of both regions (i.e FZ and BM) as shown in Figures 3.2 and 3.3b. Close to the BM, the grains are elongated with an aspect ratio similar to the one of the BM whereas close to the FZ the grains become larger. In Al6000 welds, the HAZ is characterised by the growth of precipitates [28]. The precipitates found in the BM grow close the boundary FZ/HAZ and disappear in the FZ. This is visible in the middle of Figure 3.3b.

Nearby the fusion line in the HAZ, grain boundary liquation is apparent. Liquation cracking is also characteristic of aluminium alloys. This phenomenon develops at high temperature in a region that is partially melted and subjected to tensile load. As the metal solidifies, the grain boundaries separate and not enough metal is present to fill these cracks, they remain in the HAZ.
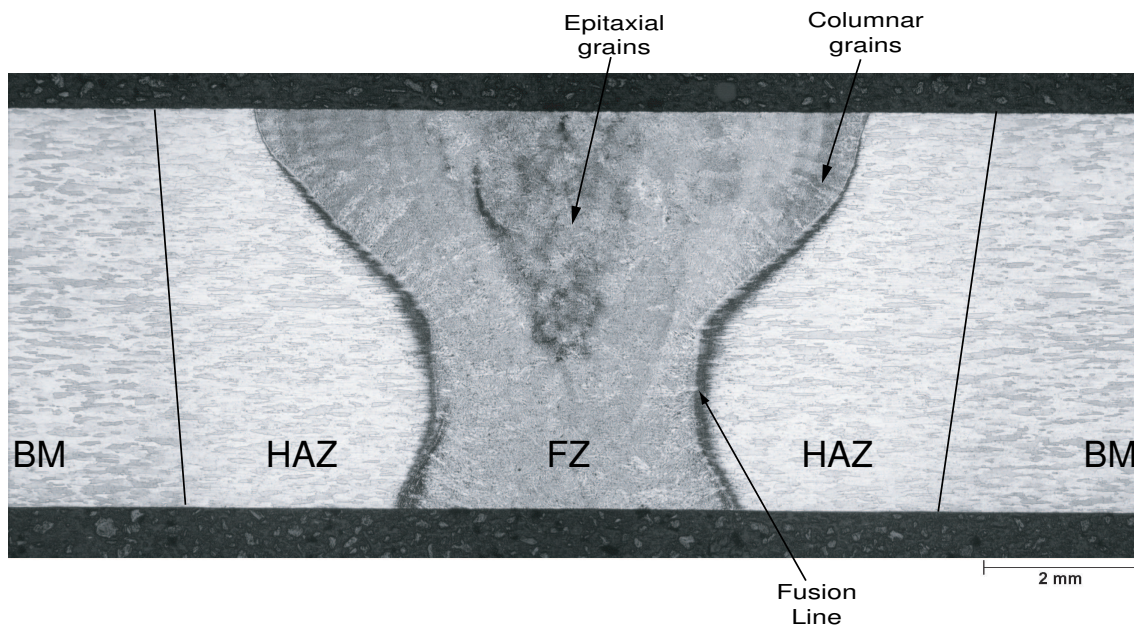
Figure 3.2: Cross section of the Al6056 T78 laser beam weld
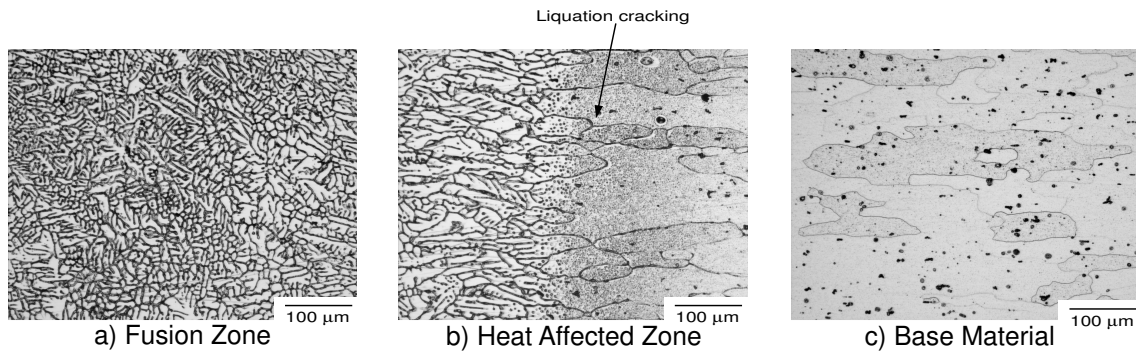
Figure 3.3: Microstructure of the three zones of the laser weld a) fusion zone, b) heat affected zone and c) base material
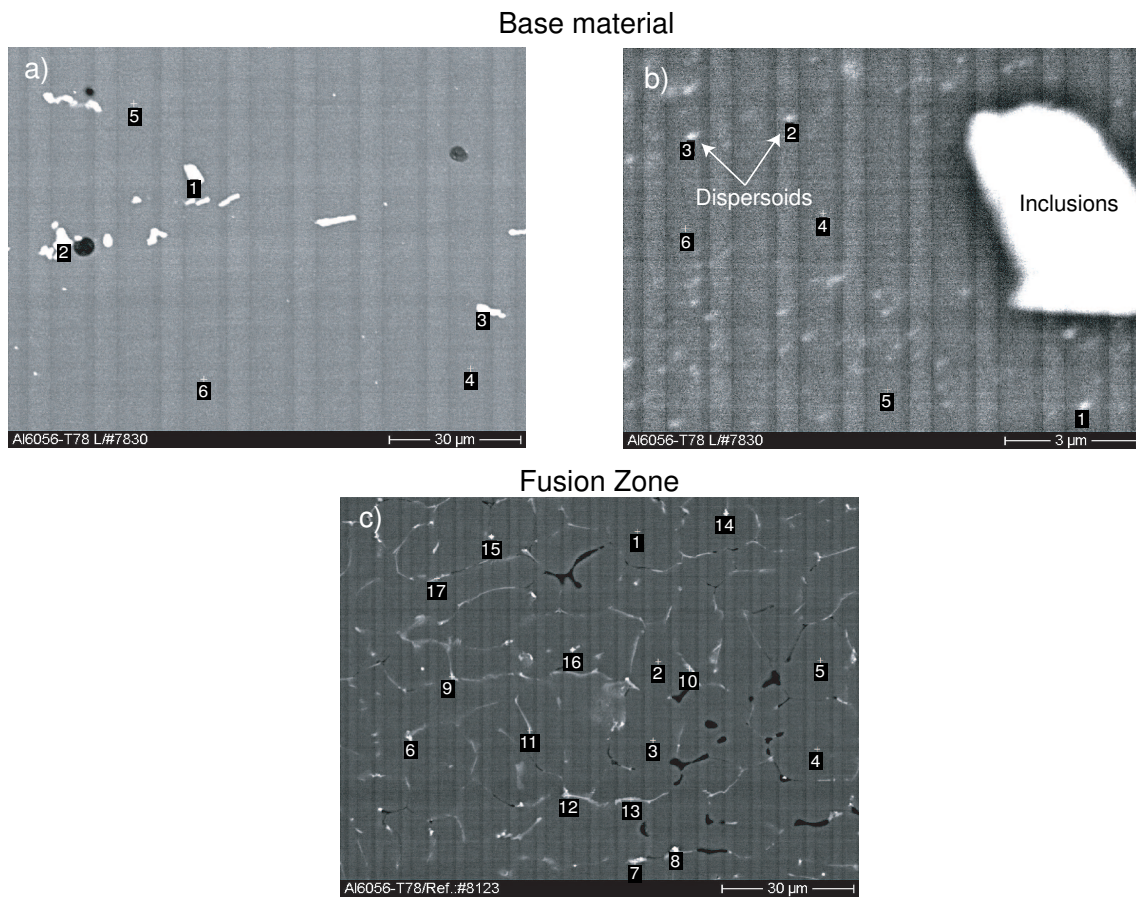
Figure 3.4: SEM pictures of the EDX analyses. The numbers indicate the locations of the measurements

	Al (%)	Mg (%)	Si (%)	Mn (%)	Fe (%)	Cu (%)
Matrix	98.37	0.31	0.68	0.41	0	0.22
in BM	± 1.8	± 0.2	± 1.1	± 0.1		± 0.4
Large	61.21	0	9.38	14.87	12.81	1.73
Particles (BM)	± 9.38		± 0.2	± 0.6	± 0.2	± 0.4
Small	93.88	0.79	1.99	2.49	0.25	0.60
Particles (BM)	± 0.5	± 0.1	± 0.1	± 0.5	± 0.2	± 0.5
Matrix	98.12	0.67	0.51	0.26	0	0.45
in FZ	± 0.2	± 0.03	± 0.07	± 0.2		± 0.3
Dendritic	70.31	0.91	15.02	6.94	4.90	1.91
arms (FZ)	± 7.7	± 0.7	± 4.5	± 2.2	± 3.1	± 1.7
Particles	63.25	1.14	5.71	1.23	0.90	27.77
(FZ)	± 11.7	± 0.6	±2.1	± 1.4	± 0.9	± 9.9

Table 3.2: EDX analysis of the phases in the Al6056 T78 base material (BM) and fusion
zone (FZ)

3.2 Mechanical properties of Al6056 T78 LBW

3.2.1 Microhardness

In order to identify the different zones of the weld, principally the FZ and the HAZ, the microhardness is measured across the weld. Previous hardness measurements on this weld revealed that the hardness is homogeneous through the sheet thickness, therefore only the results of the measurements in the middle of the sheet thickness is presented. For the test, a Vickers method is employed: a load of 200 N is applied during 10 seconds using a prism indenter. The print on the material surface is square and the two diagonals are measured. The Vickers hardness is proportional to the ratio (applied load) / (size of the print). Every 0.3 mm a measurement is realised. The hardness profile of the studied Al6056 T78 laser weld is plotted in Figure 3.5.
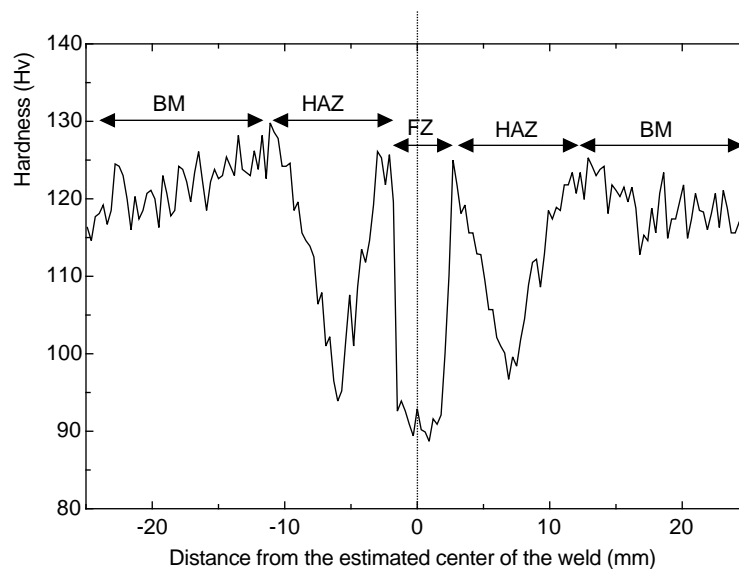
Figure 3.5: Microhardness profile across the laser weld

The weld metal has the lowest hardness - around 90 HV. At a distance of approximately 2.5 mm from the fusion zone middle, the hardness is that of the base material and it decreases again with its minimum ($HV = 95 - 98$) in the HAZ at a distance of 7 mm from the center of the fusion zone. After this valley, the hardness increases again to reach that of the BM at 10 mm. A slight difference in the hardness value is observed in the base material zones on each side of the laser weld. The increase of hardness close to the FZ, location of elevated temperature, is attributed to the dissolution of the particles into solid solution that will precipitate during cooling to form strengthening phases. The minimum in hardness is often referred to as overaged zone since this location has been subjected to temperatures in the range $290 - 450°C$ [28]. At such temperature the particles are not dissolved.

3.2.2   Tensile behaviour

For thin sheet material, round tensile specimens used to determine the tensile behaviour of the material cannot be machined due to their size requirements: the smallest standardised round specimen has a diameter of 2.5 mm and a head of 4 mm. Instead flat tensile specimens can be used and have been proven to give similar stress-strain curves as a round bar [119]. Therefore flat tensile specimens can be used to determine the hardening behaviour of sheet material and of inhomogeneous materials such as joints [83].

To fit the narrow size of a weld, micro flat tensile specimens (MFT) are used at GKSS Research Center [51]. Such specimens allow the determination of local stress-strain data and are advantageous in the presence of stress gradients in similar and dissimilar welds for example. The tensile behaviour of steel using either MFT or round specimens have been compared by Çam et al [20]. They found a good agreement between the two procedures. The MFT specimens have a thickness of 0.5 mm, a width of 2 mm and a gauge length of 9 mm, see Figure 3.6. Their extraction is done in two steps: first a pre-shaped block is extracted with the fusion zone in its middle and then each specimen is cut out using electro discharge machining.

MFT specimens of the analysed laser weld have been extracted from the 6 mm thick sheet materials, parallel to the butt joint as presented in Figure 3.6. The first specimen is taken at a distance of 1 mm from the estimated middle of the weld, then every 0.84 mm a specimen is machined. The tensile behaviour of each region of the weld is then characterised by many tests. An "image" of the gradient in tensile properties of the laser weld can thus be built up.

a) extraction of MFT specimen   b) Micro Flat Tensile (MFT) specimen
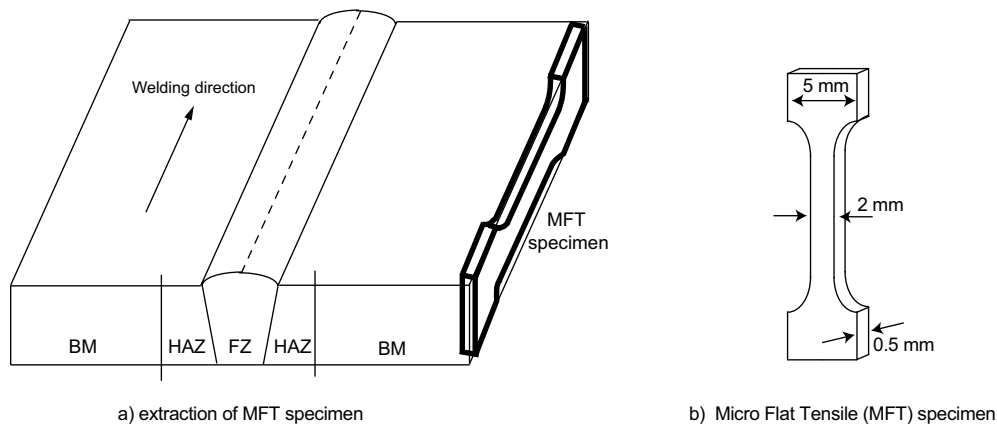
Figure 3.6: Micro flat tensile specimens: a) extraction of the specimens, b) dimensions of the specimens

Representative tensile results in terms of engineering stress vs. strain curves are plotted in Figure 3.7. Another way to present the results is displayed in Figure 3.8 by plotting the proof stress ($Rp_{0.2}$), the tensile strength (Rm) and the strain at rupture (A_{8mm}, 8 mm indicates the initial gauge length) as a function of the distance from the middle of the weld. In this case, each test result is displayed.

The weld metal is homogeneous in terms of tensile properties as the curves displayed in Figure 3.8 are symmetric regarding the middle of the weld. Nevertheless, variations of stresses and ductility are observed between the different regions of the laser weld. The

fusion zone has the lowest yield strength ($\sigma_{0.2FZ} = 200$ MPa) and fracture at low plastic strain: the ductility is around 2 %. Materials in the HAZ and BM show low strain hardening behaviour as well as low ductility. In both regions, the strain at rupture is around 10 %. High variation of yield strength and tensile strength is observed for the material in the HAZ, the scatter of these values is also represented by the grey area in Figure 3.7. A reduction of the stresses occurs at $\pm$ 7 mm from the estimated middle of the fusion zone. Such valley has also been observed in the microhardness profile, presented in Figure 3.5. Such feature is common for Al 6xxx weld. In spite of the reduced stresses, no reduced strain to rupture takes place in the HAZ. In the BM, the material appears to be homogeneous and the results obtained from the tensile tests show high reproducibility. The proof stress of the base material is $\sigma_{0.2BM} = 302$ MPa.
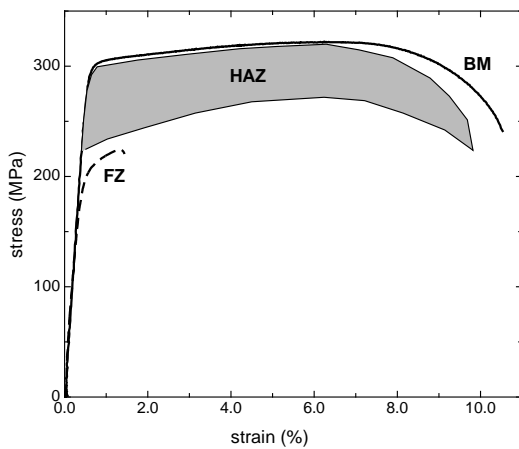
Figure 3.7: Yield curves of Al6056 T78 LBW
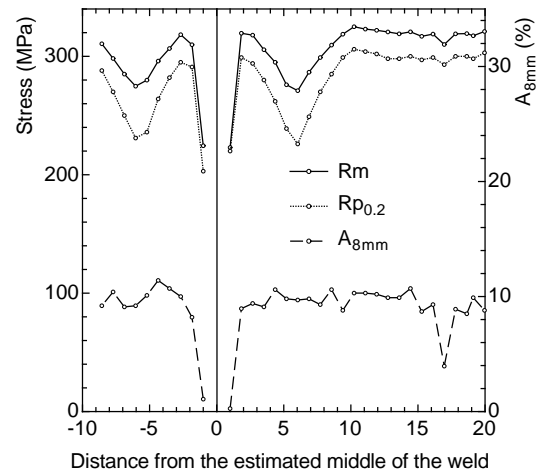
Figure 3.8: Variation of proof stress ($Rp_{0.2}$), ultimate stress (Rm) and ductility (A) across the Al6056 T78 laser weld

Since the material within the fusion zone possesses a lower yield strength than the base metal, the mismatch configuration of the laser weld is undermatched. The mismatch ratio expressed by the ratio of the yield strengths of the two materials is so smaller than one and equals $M = \sigma_{0FZ}/\sigma_{0BM} = 0.67$ for this particular weld.

3.3 Fracture behaviour of Al6056 T78 LBW

3.3.1 Fracture toughness tests

Fracture toughness tests of LBW Al 6056 have been carried out using compact tension specimens (C(T)-specimen, $W = 50$ mm, $a/W = 0.5$). Two thicknesses have been tested, namely $B = 4.2$ (the sheets have been machined down to 4.2 mm) and 6 mm. A sketch of the specimen is provided in Figure 3.9. The specimens were statically loaded perpendicular to the rolling direction. The initial crack was introduced in the BM (Figure 3.9a), in the middle of the FZ (Figure 3.9b) and within the HAZ (Figure 3.9c). To produce the initial crack of length a_0, a notch is first machined at the desired location using Electro Discharge

Machining (EDM) up to $0.4W$, then the specimen was fatigue loaded up to the initial crack length $a_0 = 0.5W$.

The test program consisted of 8 specimens with a thickness of 4.2 mm and of 3 specimens with $B = 6$ mm. The latter specimen thickness was tested only for the configuration with initial crack in BM and in FZ.
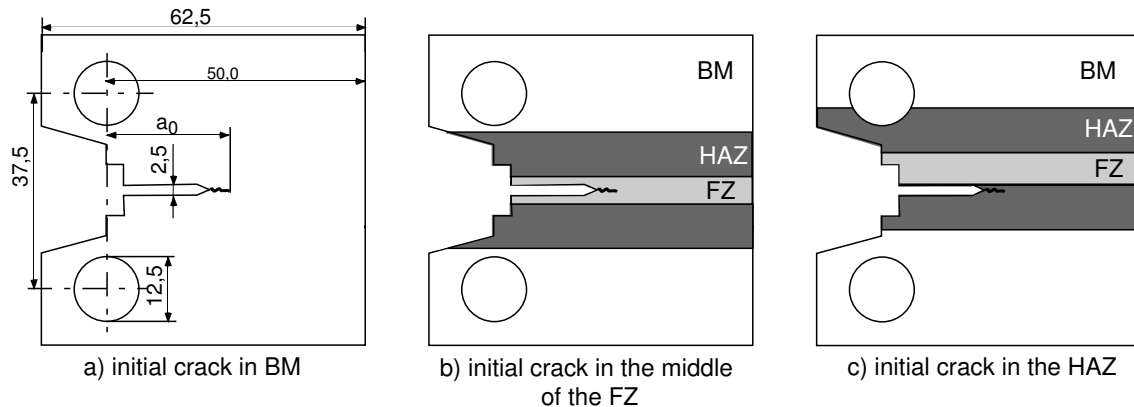
Figure 3.9: Initial crack configurations tested

The results of the fracture mechanics tests are presented in terms of force vs. Crack Mouth Opening Displacement (CMOD) and fracture resistance curve δ_5 vs. Δa for the three configurations studied, see Figure 3.10. The R-curve was constructed using a multiple specimen technique. The crack length was determined on the fracture surface of each broken specimen at the end of the test by measuring the difference between the initial crack tip and the final crack tip at various locations across the specimen thickness. An average value of the crack extension Δa is calculated using a weighted function [86]. For each initial crack configuration, a representative curve of the experimental results is plotted in Figure 3.10a in terms of force vs. CMOD.

As the butt weld considered here is undermatched, the crack initially in the FZ causes a lower load level than a crack in the BM. A crack running in the HAZ causes a response between the behaviour observed in FZ and BM. For both, FZ and BM locations of initial crack, crack extension is limited to the symmetry plane whereas in the case of a crack in the HAZ, crack path deviation occurs experimentally due to the tendency of the crack to extend into the region with the lowest yield strength: here the FZ. This phenomenon is also visible on the R-curve as the R-curves labeled HAZ and FZ merge together (Figure 3.10).

Independently of the location of the initial crack, a crack running in a thicker plate (from $B = 4.2$ mm to $B = 6$ mm) causes a higher load level during the test, but a similar fracture resistance curve as the stress state, hence the constraint, does not vary much between the two sheet thicknesses, thin sheet conditions still prevail $((W - a)/B \geq 4)$.
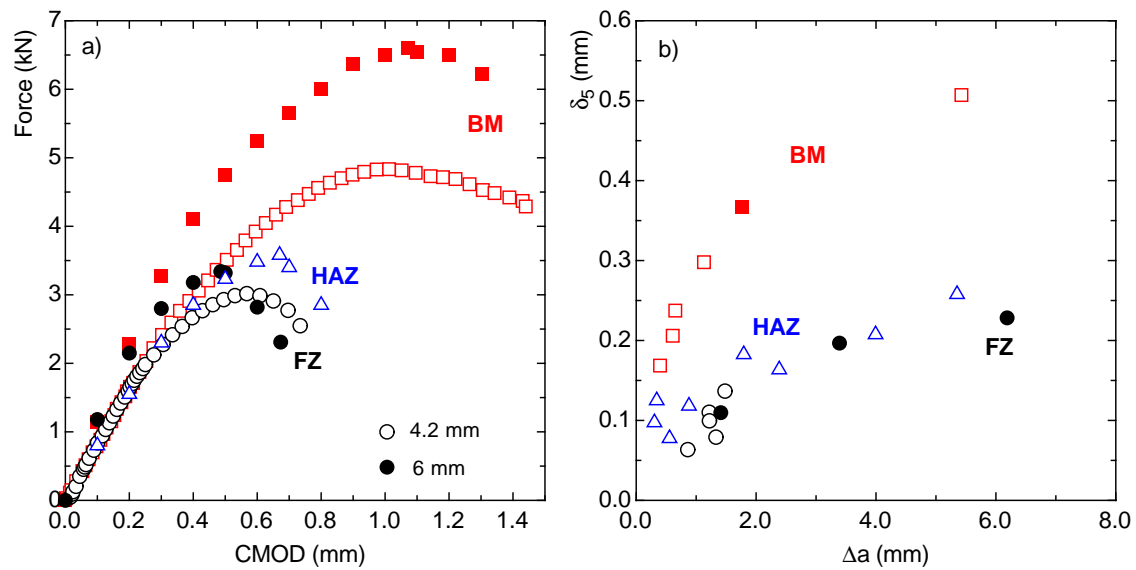
Figure 3.10: Fracture behaviour of Al6056 T78 LBW

3.3.2 Fracture surface analysis

Once the desired load level has been reached during the fracture toughness tests, the specimens were fatigue loaded to "mark" the region of stable crack extension as shown in Figure 3.11. The specimens were broken and the post test fractography analyses can be carried out for different crack lengths using Scanning Electron Microscope. The 4.2 mm thick specimen with the longest crack length was selected for the examinations for each initial crack configuration. The observations are discussed below. Figure 3.12 is a side view of an initial HAZ crack, showing crack path deviation into the low yield strength material, here the FZ. The white line indicates the location of the initial crack between the FZ and the HAZ.

Al6056 T78 base material

Stable crack extension within the base material shows a tunneled shape and in spite of the relatively thin thickness of the specimen the fracture surface remained normal to the loading direction, see Figure 3.11a. On the fracture surface presented in Figure 3.13a large equiaxed dimples are visible. At a higher magnification (Figure 3.13b) it is observed that these large dimples contain large broken particles that can be identified as Fe-rich particles; an example is indicated by the white square, see Figure 3.13b. A second population of smaller dimples are also observed that characterises micro-plasticity and which form a phenomenon of void sheet mechanisms. At higher magnification (displayed in Figure 3.13c) small particles are observed at their bottom which correspond to the dispersoids: Al-Mn-Si. They can be identified by their shape and size, since the dispersoids have an average diameter around 0.2 μm.

The fracture surface is characteristic of ductile fracture with void growth and coalescence.

Al6056 T78 fusion zone

Here, the crack propagates again in the specimen ligament plane having a triangular shape, Figure 3.11b. At low magnification, the fracture surface has irregular features. The fracture surfaces present small sheared elongated dimples which seem to possess an orientation. The sheared dimples indicate a non pure mode I fracture. At the bottom of the larger dimples (Figure 3.14), some elongated items are observed which might correspond to the elongated dendrites found in the study of the microstructure of the fusion zone. Moreover, intact dendrite arms can also be observed in that case as shown in Figure 3.14, meaning that the crack does not run in a fully plastified manner. Those dendritic branching can also be the result of cavity shrinkage caused by welding forming microporosity. The pores formed by the dendrites help justify the flat R-curve of the FZ crack configuration. However, the overall fracture behaviour is ductile and is characterised by void initiation, growth and coalescence, similar as in the BM initial crack configuration.

Al6056 T78 heat affected zone

In the case of crack growth within the heat affected zone, it is observed that the crack deviates into the fusion zone which possesses lower yield strength, see Figures 3.12 and 3.15. The crack starts to deviate as soon as crack extension occurs and no slanted crack is observed. Those two visual observations are confirmed by the fracture surface topography measurements. Topography measurements using laser equipment have been carried out to quantify the degree of crack kinking. The starting point of the measurement is at the surface of the specimen at the beginning of the fatigue pre-crack. Then the laser sensor measures the height of the fracture surface every 10 μm in x-direction (ligament direction) and every 50 μm in thickness direction (y-direction). The topography of the fracture surface of six specimens with different crack lengths was mapped. The results of the measurement for two different specimens having the longest crack extension are presented in the following. 3D images of the crack paths are presented in Figure 3.15. On Figure 3.16 two 2D plots are derived from the 3D topography measurements, the variation of height is plotted as a function of the ligament coordinate for three different locations across the specimen thickness, namely: $y = 0$, 2 and 4 mm; $y = 2$ mm being the mid-thickness plane. An average angle of crack kinking can be evaluated from these 2D plots, $\alpha_{av} = 17°$. The limiting angles of deviation of the crack are $\alpha = 10°$ and $\alpha = 25°$.

In addition, the fracture surfaces have been analysed post-test using SEM. Some pictures of the fracture surface are presented in Figure 3.17 at two different magnifications and for three locations on the fracture surface. The locations schematised at the top of Figure 3.17 represent various stages of crack extension: location 1 is near the initial crack tip, location 2 corresponds to the middle of the final crack length and location 3 is at the crack tip at the end of the test. A variation of the damage mechanisms with the location of the studied area is observed as the crack changes its extension plane. Location 1 and 2 are similar whereas at location 3, dendritic microstructure is recognisable and the dendritic orientation observed within the middle of the FZ is also visible. Independently of the studied area, the fracture surface presents mainly small dimples containing round or elongated particles and the features are similar to the one observed in the FZ initial crack configuration.
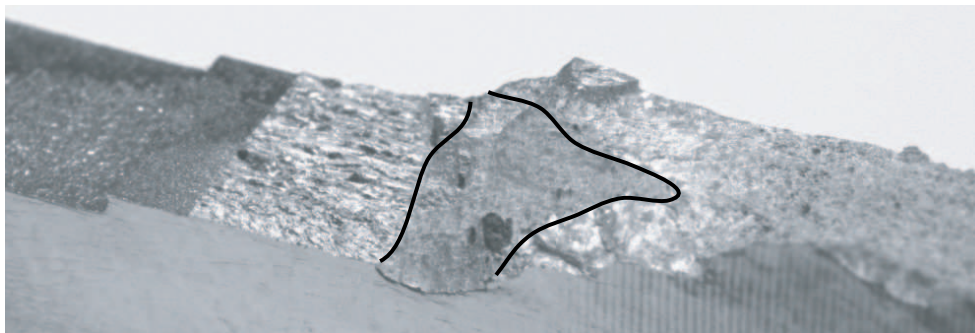The fracture surface features of initial crack within the HAZ are dependent of the "actual"

location of the crack either it is close to the BM or within the FZ and therefore possesses the characteristic of the zone in which the crack extends.
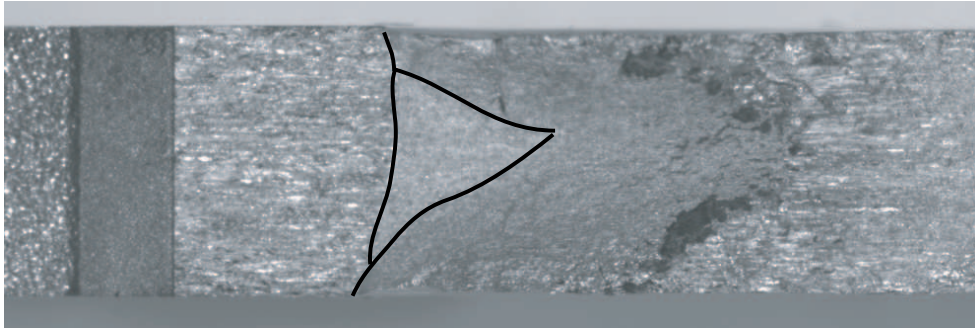
a) Crack extension in BM
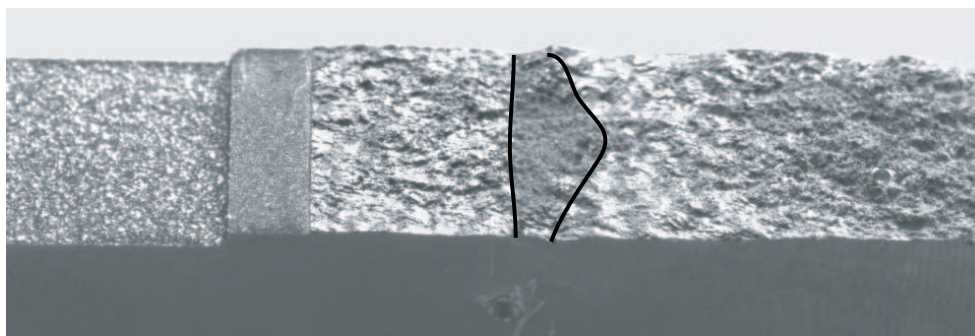
b) Crack extension in FZ

c) Crack extension in HAZ

Figure 3.11: Fracture surfaces of Al6056 T78 a) base material (BM), b) fusion zone (FZ), c) heat affected zone (HAZ)
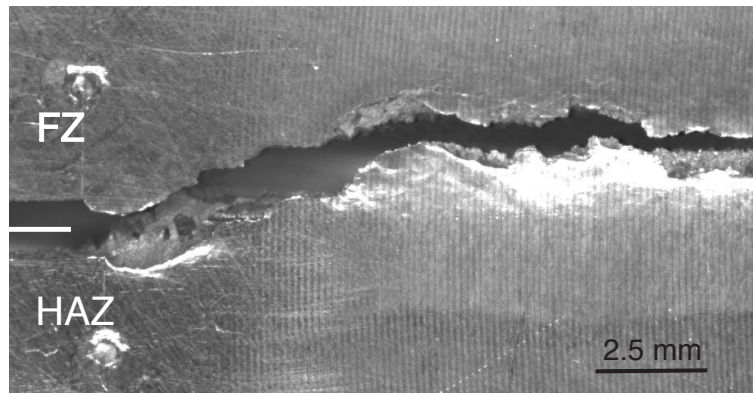
Figure 3.12: Crack path deviation of interface crack: view of the specimen side
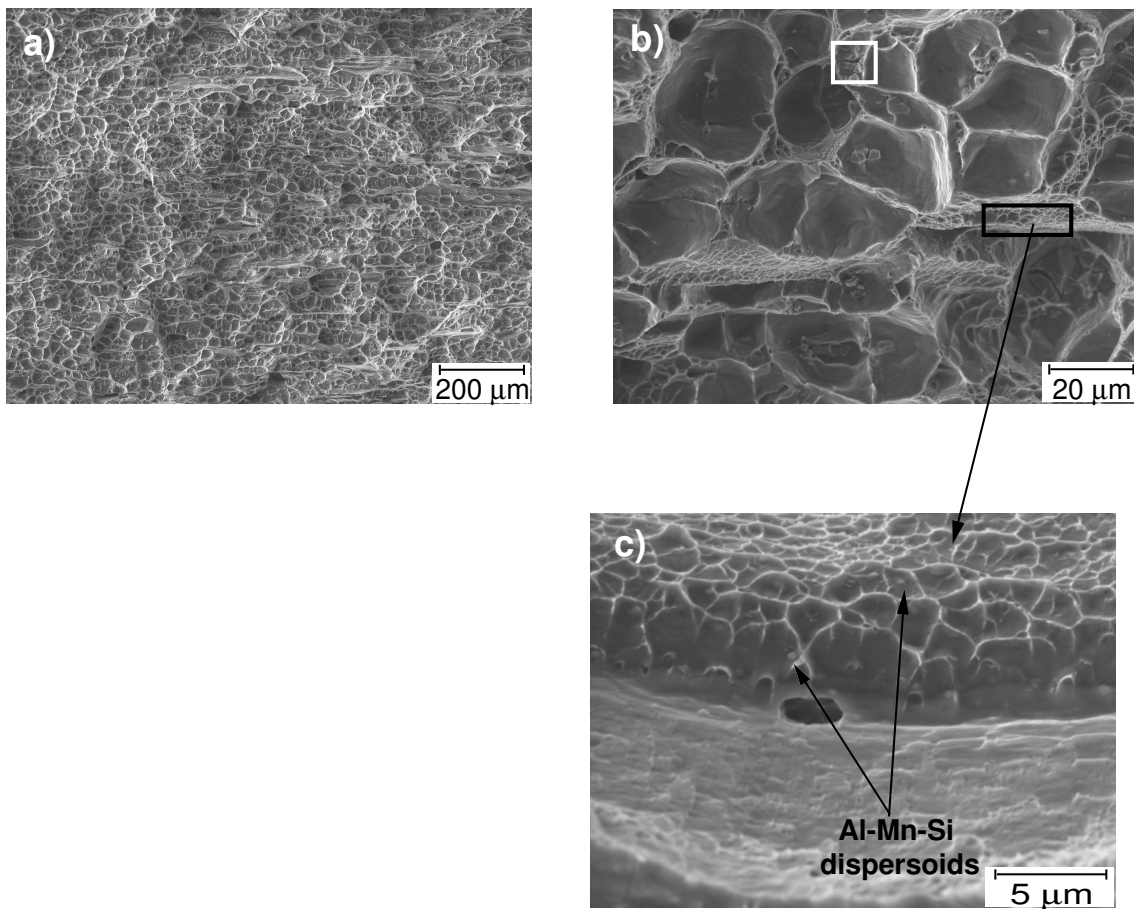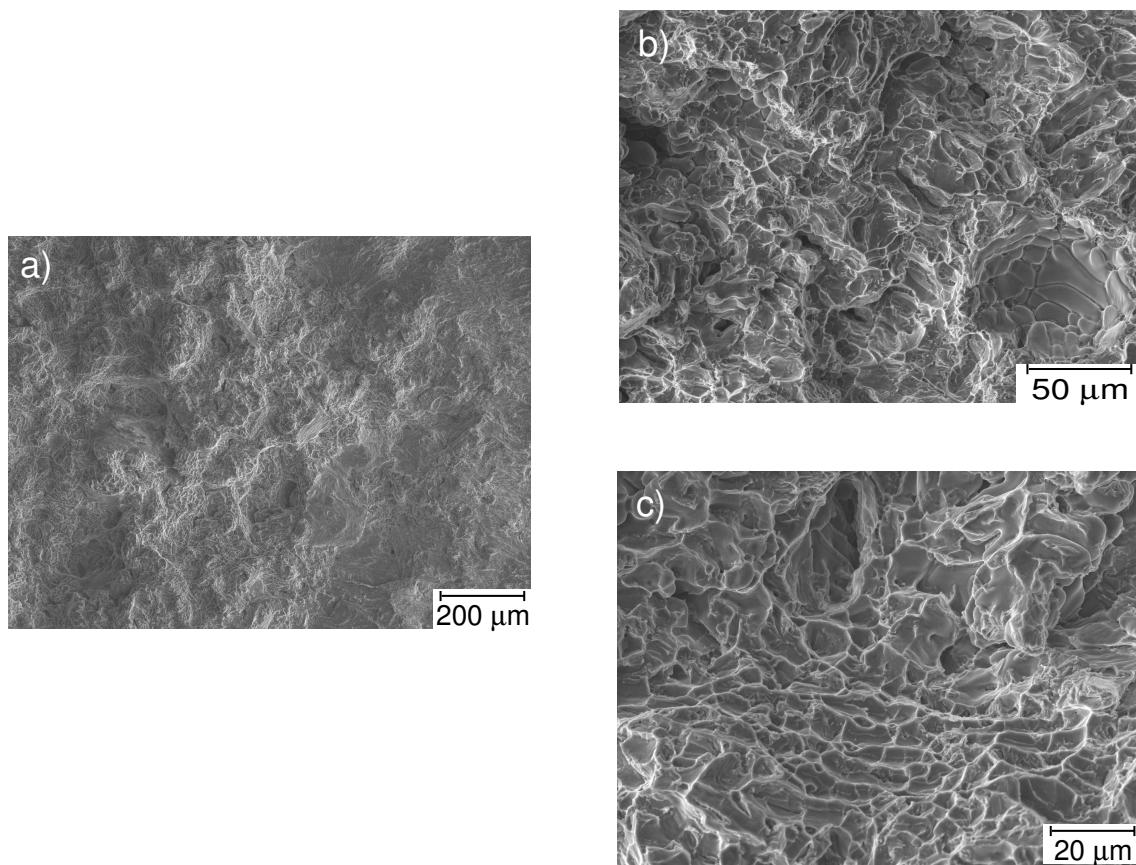

Figure 3.13: Fracture surfaces of Al6056 T78 base material

Figure 3.14: Fracture surfaces of Al6056 T78 fusion zone
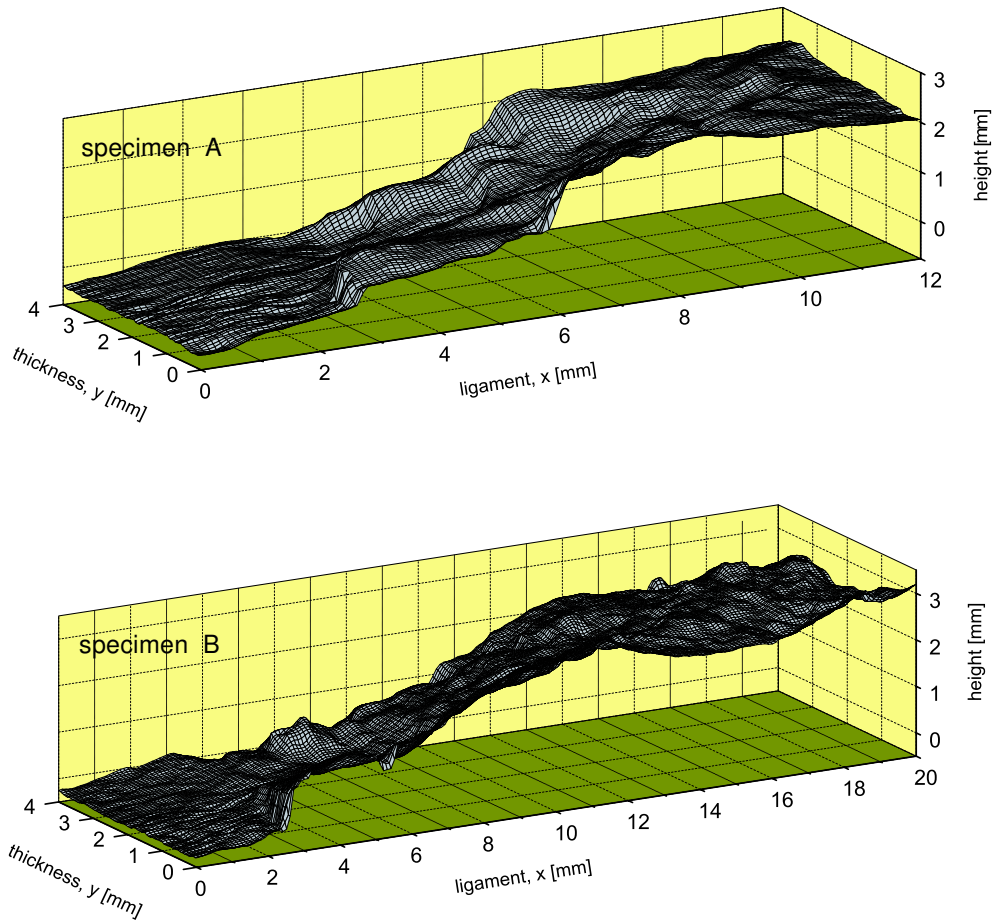
Figure 3.15: Topography of fracture surface of two Al6056 T78 heat affected zone speci-
mens
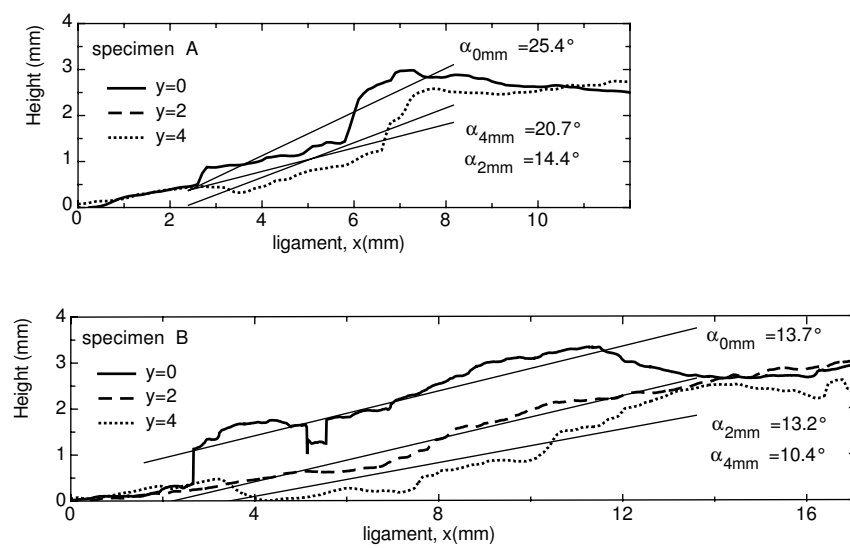
Figure 3.16: 2D representations of the angle of crack kinking
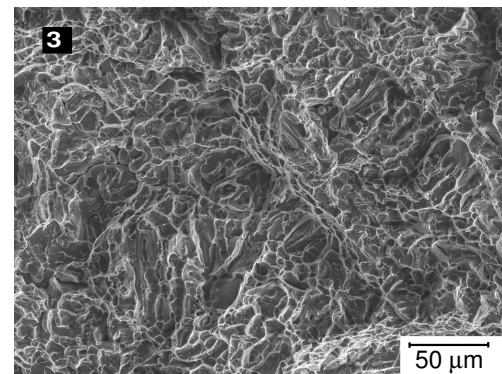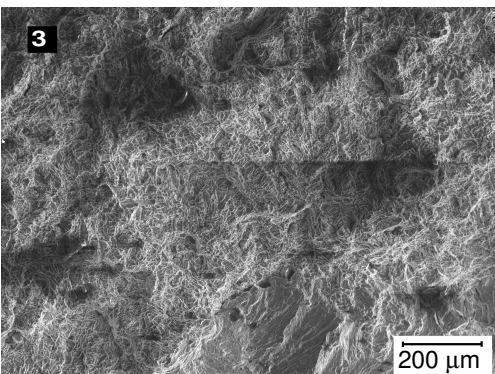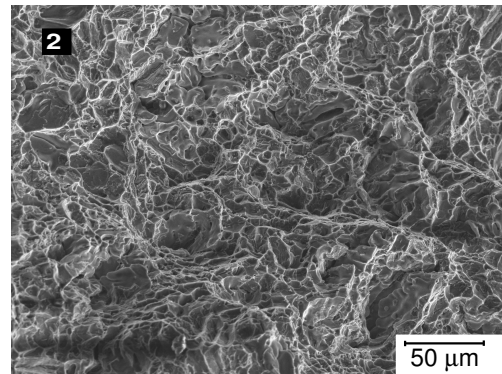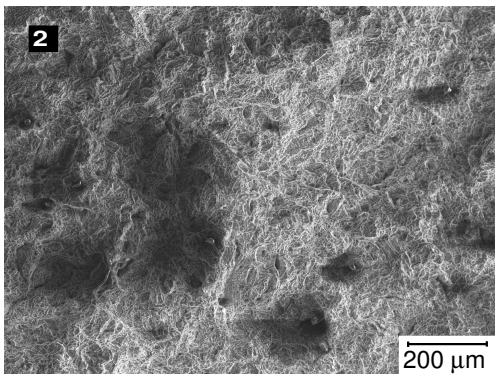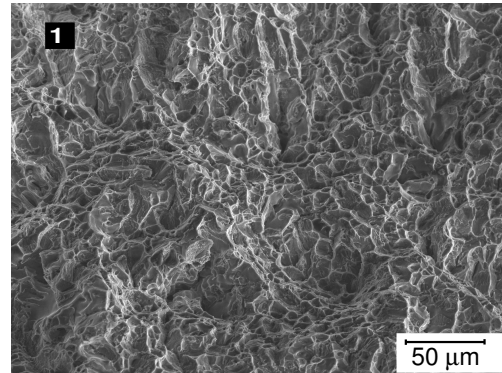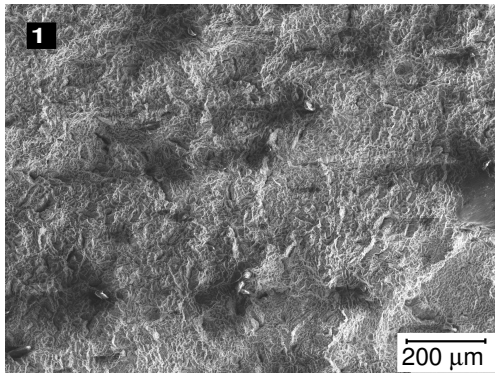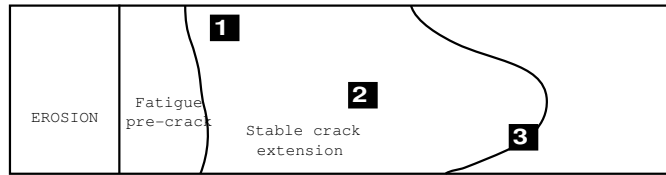
Figure 3.17: Fracture surfaces of Al6056 T78 heat affected zone

Chapter 4

Simulation of crack extension in homogeneous material - the GTN approach

In the following chapter, numerical simulations of crack extension using the Gurson-Tvergaard-Needleman model are carried out for cracks in homogeneous materials. The term homogeneous material refers to a material that possesses no variation of properties close to an eventual defect or crack. In fracture mechanics specimens, the crack tip has to be located within a single material without any interface. The following initial crack configurations, as described in Chapter 3, are analysed in this section:

- the initial crack is introduced within the base material (BM), no weld is considered. This configuration is sketched in Figure 3.9a,

- the initial crack is introduced in the fusion zone (FZ), in the middle of the butt weld, as drawn in Figure 3.9b.

The numerical simulations are performed for Al6056 T78 LBW whose properties have been identified in Chapter 3. The global fracture behaviour of the laser weld being ductile, see the previous chapter, the GTN damage model is employed to characterise the material degradation due to void nucleation, growth and coalescence.

4.1 Identification of the GTN-parameters

Assuming damage evolution due to void growth only in the GTN-formulation, the following parameters have to be determined for both Al6056 T78 base and weld metals:

- the initial void volume fraction f_0,

- the critical void volume fraction f_c and the acceleration factor κ,

- the model parameters q_1 and q_2,

- the strain hardening behaviour,

- a characteristic length, the size of the finite element at the crack tip, D.

The latter becomes clear by the following two arguments. Experimentally, in a homogeneous material, a crack, statically loaded, extends perpendicularly to the main loading direction in a planar manner within a zone having one to two void spacings in thickness [80, 115], see Figure 4.1a. This layer is characterised by intense plastic deformation in which void growth and coalescence take place. Taking into account this observation, Xia and Shih [115] introduced the concept of computational cells in the process zone ahead of the crack. The term computational cells emphasises the fundamental difference to a concept of finite elements as purely numerical entities. These cells are representative volume elements reproducing the micromechanims of void initiation, growth and coalescence in an energy equivalent way. Each cell within the process zone contains a single void of volume fraction, f_0, as sketched in Figure 4.1b. The voided cells are square of side length D, D is related to the nearest neighbour distance between two large particles. D is also of the order of the crack tip opening displacement, δ, which is several times the mean void spacing [115]. The material surrounding the process zone follows a von Mises plasticity potential. As deformation develops, the voids evolve and coalesce as presented in the left hand side of Figure 4.1b.

The mechanical work dissipated per increment in one finite element having the dimensions w (width), b (thickness) and D (height) by inelastic deformation results from

$$\Delta U_{dissipation} = \int_{\Delta V} \int_t^{t+\Delta t} \boldsymbol{S} \cdot \dot{\boldsymbol{\epsilon}}^{pl} dt dV = \int_{\Delta V} \boldsymbol{S} \cdot \dot{\overline{\boldsymbol{\epsilon}^{pl}}} dV = \overline{u}_{dissipation} \Delta V \qquad (4.1)$$

with the element volume $\Delta V = wbD$. The energy release rate per crack extension increment, $\Delta a = w$ i.e. one element width, is

$$\Gamma_0 = \frac{\overline{u}_{dissipation} \Delta V}{\Delta A} = \frac{\overline{u}_{dissipation} \Delta V}{b \Delta a} \sim D \qquad (4.2)$$

which is the specific "work of separation", see Siegmund and Brocks [96, 97]. By increasing the element height, more mechanical work is dissipated - or energy "released" - per increment of crack extension. This affects, of course, the global behaviour of a structure. Figure 4.2 presents the effect of the element height at the crack tip of a C(T)-specimen ($W = 50$ mm) in terms of force-CMOD curve and fracture resistance curve (δ_5 vs. Δa curve). Three values of element height are chosen: $D = 0.1, 0.15$ and 0.2 mm. An increase of element height increases the maximum load and the crack tip opening displacement at initiation. The R-curve is steeper for high elements at the crack tip, see Figure 4.2b. As the results are mesh size dependent, the element size becomes an additional material parameter.
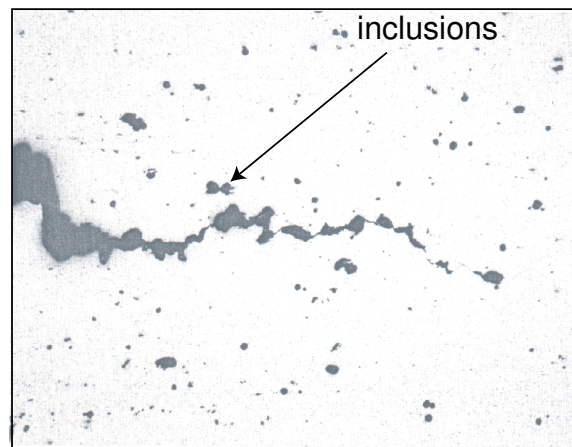
a) Ductile crack extension under static loading of
C(T)-specimen of Al6056
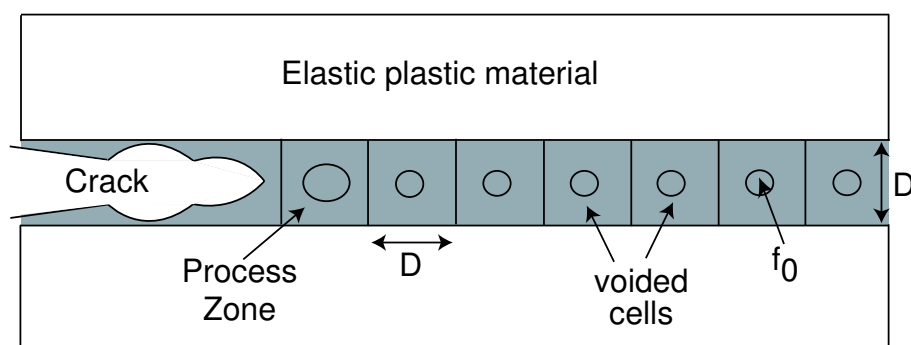
b) Sketch of the process zone and computational cells
concept

Figure 4.1: "Computational cells" concept

4.1.1 Identification of the microstructure related parameters: f_0, D

From the existing literature on 6xxx aluminium alloys series [37, 62], the large particles with diameters (d) larger than 1 μm are assumed as damage initiation sites. These large particles ($d > 1$ μm) are called inclusions hereafter. The dispersoids ($0.1 < d < 1$ μm) do not influence the fracture toughness of the aluminium alloy at low strain. The precipates being responsible for the hardening behaviour of the materials, both dispersoids and precipitates are therefore not taken into account as microstructural input parameter of the GTN-model for the Al6056 T78 alloy. The inclusions fracture or debond from the matrix at low strain, therefore the initial void volume fraction (f_0) - microstructural input parameter of the GTN-model - is assumed to be equal to the volume fraction of the inclusions present in the material.

Quantitative microstructural investigations are carried out to determine the volume frac-
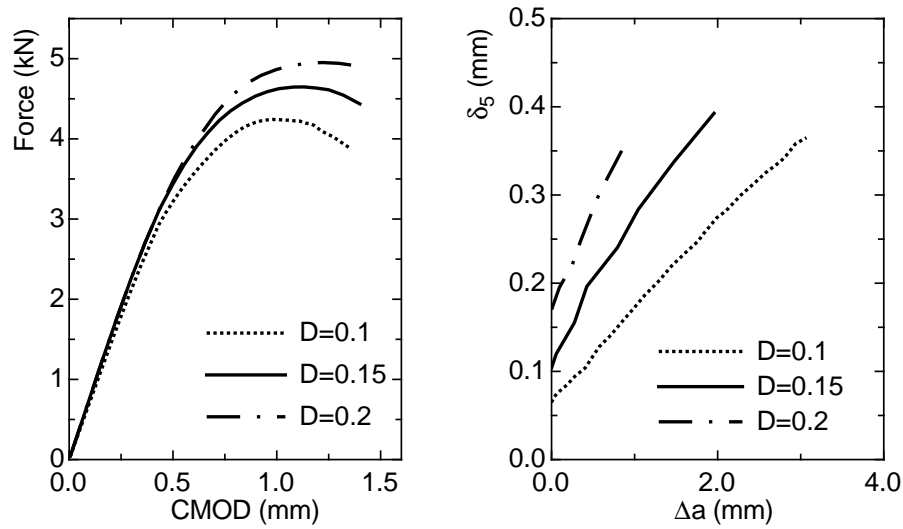
Figure 4.2: Influence of the element height (D in mm) at the crack tip in BM

tion of the inclusions (V_i), the dimensions of the particles (d) and the nearest neighbour distance between inclusions (NND). The quantitative analysis of the microstructure is realised using an image analysis software from IMTRONIC GmbH: Image C. A filter function is used to obtain a binary image from the original picture taken from the microscope, see Figure 4.3. The filter is based on grey-scale evaluation and the ranges of grey of interest have to be carefully selected by the operator. The binary image is further used in the quantitative analysis.

Figure 4.3: Binary representation of the microstructure

Having selected the criteria required (V_i, NND...) the analysis is automatically run by the software. The objects that are cut by the border of the analysed windows, represented in light grey in Figure 4.3, are removed from the results of the analysis. The entire shape of these objects being unknown, their addition may lead to some errors in the quantitative analysis as for example in the determination of the average size of the objects.

The diameter of the inclusions is determined using the average of the Feret diameters, Eq. (4.3). The Feret diameters are the dimensions of an object in thirty-six different orientations as demonstrated in Figure 4.4a for three preferential directions: 0°, 45° and 90°. The Feret diameters, in the software Image C, vary from 0° to 175° with an increase of 5° between two orientations. The diameter of the inclusion is therefore:

$$d_{object} = \sum_{i=1}^{36} Feret_i/36. \tag{4.3}$$

The nearest neighbour distance between two inclusions is depicted in Figure 4.4b. The distance between the two bodies is taken between the centers of gravity of two neighbouring objects.

a) Feret diameter (μm)   b) Nearest Neighbour
                                Distance (μm)
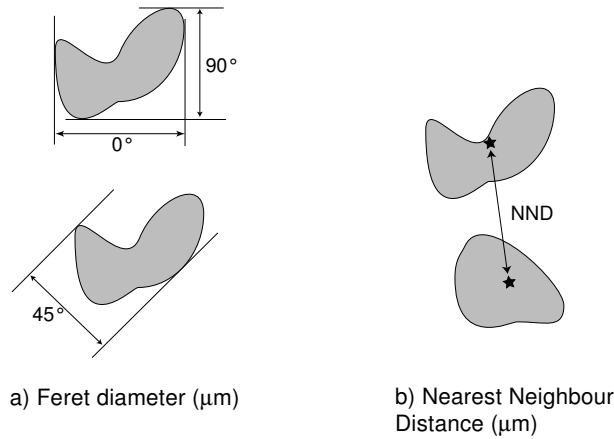
Figure 4.4: Schematic of microstructural quantities: a) Feret diameter, b) Nearest Neighbour Distance

In section 3.1, a qualitative analysis of the microstructure of the aluminum laser weld has been presented. Now, the microstructure of both Al6056 T78 base and weld metals is qualitatively analysed. Emphasis is given to the microstructural quantities that are required for the modelling activities, namely f_0 and D.

Several pictures have been taken of the BM and in the FZ at different locations to be representative of the materials. 9 pictures have been analysed in each case: 3 on the top of the material sheet, 3 in the middle and 3 at the bottom at small magnification. The statistical sample is small due to the limited amount of material available. For Al6056 T78 BM, only the inclusions with diameters $d > 1$ μm are analysed; whereas due to the reduced lengthscale observed on the fracture surfaces of Al6056 T78 FZ, all the particles are considered independently of their diameter for the weld material. The results of the quantitative analysis are presented in Table 4.1.

In the BM, the large inclusions that can be either Fe-rich phase or Mg_2Si particles are studied. Their average diameter is 3.5 μm and the maximal diameter is 18 μm. In the FZ, the particles are smaller and tend to nucleate around the dendritic arms. The particles measure in average 0.7 μm and 18 μm as maximum. The distributions of the particles diameter in BM and FZ are presented in Figure 4.5a and b, respectively. Both distributions represent normal distributions with the main part of the particles being smaller than 5 μm in BM and 2 μm in the FZ.

The distributions of the NND measurements for BM and FZ are presented in Figure 4.6a and b, respectively. The maximal nearest neighbour distance between two particles in FZ is four times smaller than the one in the BM.

Material	V_p (%)	$d_{inclusions}$ (μm)		NND (μm)
		average	maximal	
Al6056 T78 BM	1.15	3.46	18	< 40
Al6056 T78 FZ	3.5	0.7	18	< 10

Table 4.1: Quantitative microstructural analysis

In the modelling of crack extension in homogeneous materials, the initial void volume fraction is set equal to $f_0^{BM} = 0.0115$ for Al6056 T78 BM and equal to $f_0^{FZ} = 0.035$ for Al6056 T78 FZ. In fracture mechanics specimens, the element height at the crack tip (D) can be estimated by the NND by considering that the finite element height at the crack tip can be three to five times larger than the average nearest neighbour distance between inclusions [100]. The finite element height at the crack tip is 150 μm and 35 μm for Al6056 T78 BM and Al6056 T78 FZ, respectively.
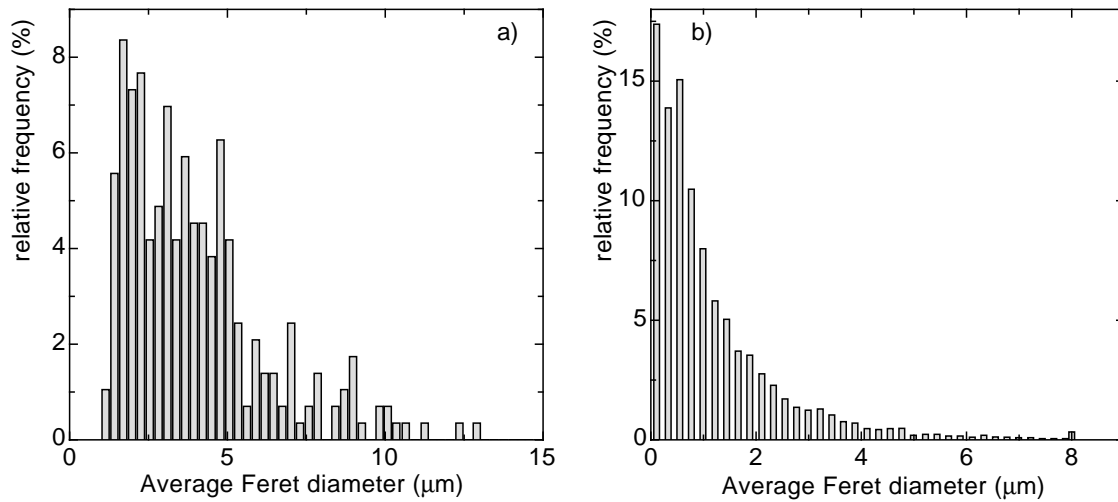
Figure 4.5: Distribution of the inclusions Feret diameter in Al6056 T78 a) BM, b) FZ
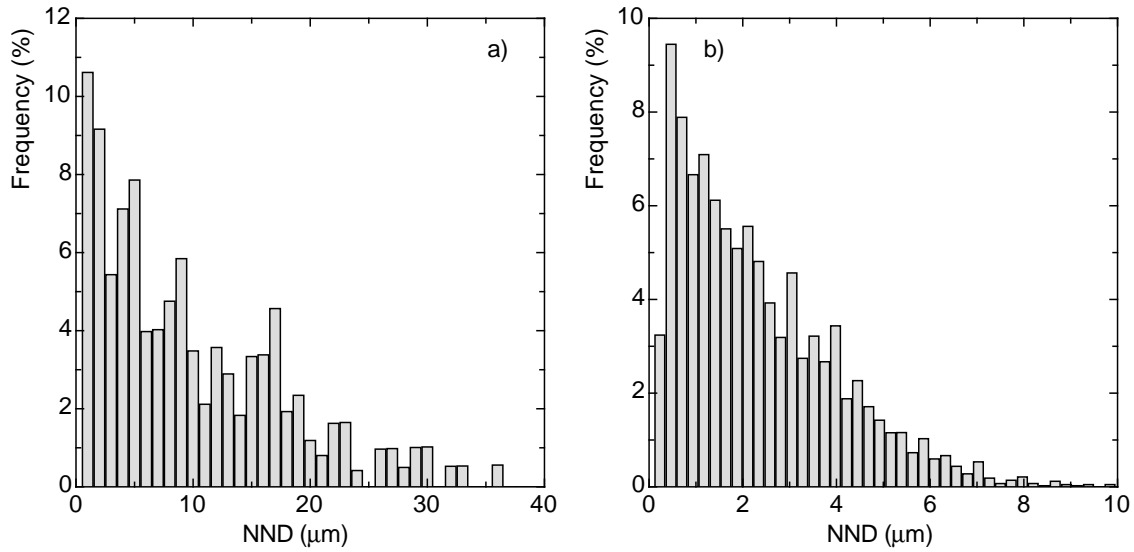
Figure 4.6: Distribution of the nearest neighbour distance between two inclusions in Al6056 T78 a) BM, b) FZ

4.1.2 Identification of the hardening behaviour

For the determination of the hardening behaviour expressed in terms of plastic strain - true stress data, a principal problem arises: the effect of the hardening behaviour due to precipitate strengthening and dislocation pile up at grain boundaries and the softening behaviour due to damage cannot be separated. The strain hardening behaviour is usually derived from the macroscopic response of a tensile test in terms of global elongation, Δl, and external force F. Hardening on the one side increases the load level at a given elongation, damage on the other side reduces the global material stiffness. Both effects interact and influence each other. FE-simulation can be used to study the respective influence on the macrocopic response by simply varying the hardening parameter, initial void volume fraction or other parameters of the GTN-model.

The Evolution Strategy (ES) algorithm is used to determine the hardening behaviour of the Al6056 T78 LBW. The ES method based on the Darwinian evolution laws is an iterative mathematical tool to optimise functions. The algorithm searches to minimise the difference between a target function and the function to be optimised. In this work, the target functions are the two experimental tensile results from the micro flat tensile tests of Al6056 T78 base material and weld material and the functions to be optimised are the results of the FE-simulation. The initial population of individuals consists of the pairs of force-displacement data resulting from the tensile test which are considered as parents. Each simulation of a tensile test represents a child within the evolution process. The children mutate and the "best" individuals are selected and serve as parents in the next generation. The selection of the individuals is made between both parents and children or between the children only depending on the strategy used. This loop is stopped once the difference between the solution and target functions attains a limit predefined by the operator.

For the discretisation of the MFT-specimen, plane stress finite elements are used, because the thickness to length or width ratio of the respective specimens is very small and the stress components in the thickness direction can be assumed to be small compared to those in the loading plane. The last assumption is confirmed by 3D calculation. The stresses in the thickness direction are quasi zero and can then be neglected. The results of the 3D calculation in the case of the base metal are presented in Figure 4.7.

The dimensions of the MFT specimens are given in section 3.2.2. The GTN-model is used to describe the yielding behaviour. The initial void volume fractions were fixed to the value reported in the previous section, namely $f_0^{BM} = 0.0115$ and $f_0^{FZ} = 0.035$. The parameters f_c and κ do not play a role for the simulations because they are particularly linked to the fracture behaviour which is not considered here. The values of q_1 and q_2 were set to 1.5 and 1.0, respectively, for the two configurations. The hardening behaviour of the respective material can therefore be optimised while taking into account damage evolution. As necking in the thickness direction observed in the experiment cannot be reproduced by the simulations due to the use of plane stress elements, the optimised yield curves meet the experimental ones up to the maximum load, see Figure 4.7. Although the void growth rate in the simulations is probably underestimated due to the limited triaxiality in plane stress elements, the effect of damage evolution at an early stage of deformation can be considered by this procedure.
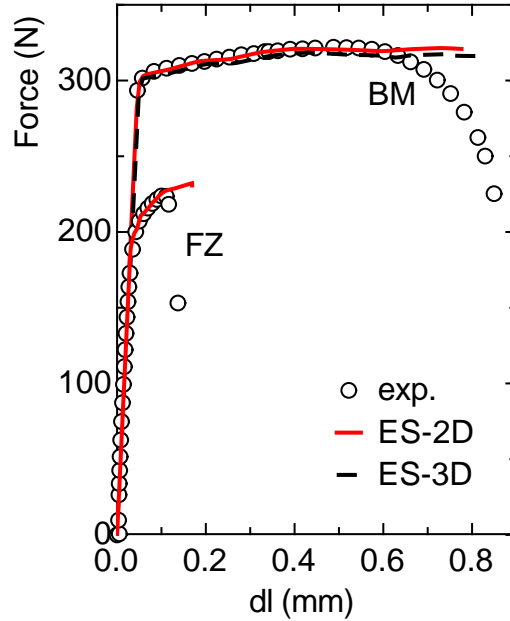
Figure 4.7: Results of the simulation of the MFT tests using hardening behaviour from the ES

The hardening behaviours obtained can be extrapolated using a power law from Ludwik. The Ludwik equation reads:

$$\sigma = \sigma_0 + K\epsilon_{pl}^n. \tag{4.4}$$

Both materials are low hardening. The strain hardening exponents are $n = 0.67$ for Al6056 T78 BM and $n = 0.25$ for Al6056 T78 FZ.

4.2 Crack extension in Al6056 T78 base material

Generally, sheet metals fracture macroscopically in a slanted manner with a void growth mechanism on the microscopic scale. The slant fracture occurs under a mixed mode I-III and originates from a flat fracture surface that has tilted by 45° to the main loading direction leading to a complex 3D state of stress. A neck is thus formed at the surfaces of the specimen.

Moreover, the triaxiality, lower in thin components compared to thicker ones, varies across the thickness of the specimen: the triaxiality being lower at the surface of the specimen (close to plane stress) than at the mid-thickness plane (close to plane strain). Sun et al [102] demonstrated that damage evolution occurs preferentially in the middle of the specimen thickness which is the location of elevated triaxiality. Therefore, simulation of crack extension in thin sheet metal using damage models requires the use of a 3D mesh as the triaxiality in plane stress elements is too low to activate void growth. Moreover, this time, the effect of void growth on the global behaviour of the specimen is desired, different from the previous section, in which only the hardening behaviour of the material was simulated.

Crack extension in Al6056 T78 of a compact tension specimen ($W = 50$ mm, $a/W = 0.5$, $B = 4.2$ mm) is simulated using the GTN-model. The GTN subroutine is implemented as a User Material (UMAT) in the commercial software ABAQUS [94]. In the FE-mesh, boundary conditions are applied on the ligament and on the mid-plane in thickness direction to constrain displacement due to the symmetry in material properties and geometry at the crack tip. Therefore a fourth of the C(T)-specimen is meshed using 8-node brick elements. A sketch of the C(T)-specimen as well as of the mesh used in the simulation is given in Figure 4.8. The 3D-mesh consists of a 2D-representation that has been extruded in the thickness direction divided into ten layers of identical thickness. The number of layers has been optimised to ensure enough mesh refinement in thickness direction to guarantee reliability of the numerical results. The finite elements at the initial crack tip have the following dimensions $200 * 150 * 210$ μm^3 ($w * D * b$). After this region of small finite elements that will ensure a maximal crack extension of 6 mm, the mesh is coarsened, Figure 4.8.

One finite element is defined by three dimensions: w, D and b. These dimensions are related to the dimensions of the fracture mechanics specimen as shown is Figure 4.8. w is the width of the finite element, dimension parallel to the specimen width W, D corresponds to the height of a finite element (in the main loading direction) and b is the thickness of one element, parallel to the specimen thickness B.

The optimised set of the GTN-parameters used in the simulation is: $f_0 = 0.0115$, $f_c = 0.0195$, $\kappa = 5$, $q_1 = 1.5$ and $q_2 = 1.0$. The results of the simulation are compared with the experimental data in terms of force-CMOD and CTOD-δ_5 vs. Δa, see Figure 4.9. The experimental force-CMOD curve is representative of various tests conducted in the experimental programme. Numerically, the crack extension is calculated using the model parameter f^*: the crack extends over one finite element when f^* has reached the value $f^* = 0.9 f_u^*$ at all element integration points. An average value of crack extension Δa over the specimen thickness is calculated similarly to the experimental one.

Both the load-deformation and the fracture resistance curves are well simulated even if the maximal force is slightly underestimated. The comparison of the two results presented in Figure 4.9 labeled "el-pl" and "GTN" indicates the influence of damage initiation and
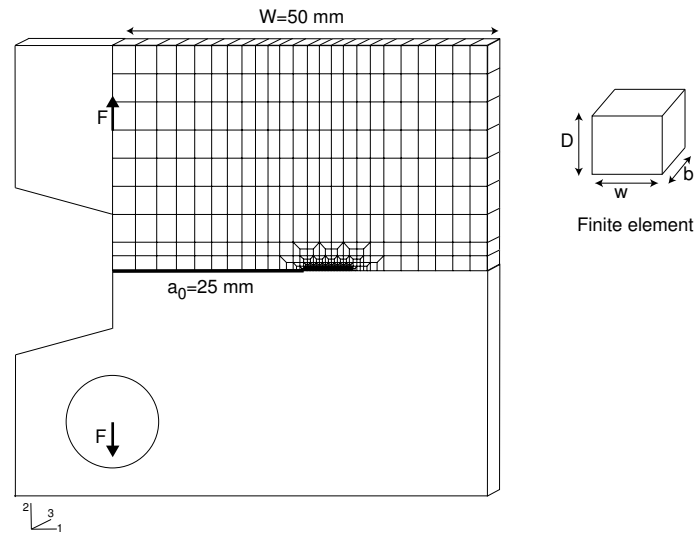
Figure 4.8: C(T) specimen with illustration of the mesh used for the simulation

evolution on the specimen global behaviour: a reduction in load carrying capacity. The force at which the two curves differ corresponds to the initiation of damage that takes place well below the maximal force.
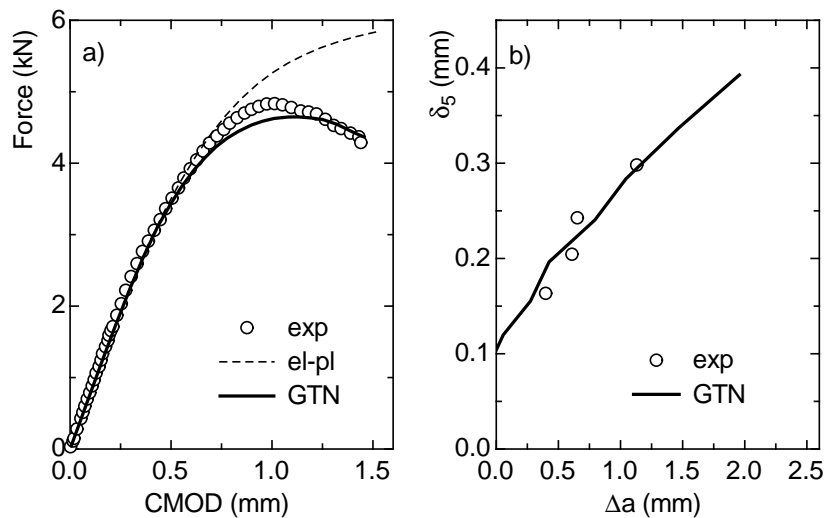

Figure 4.9: Comparison between experimental and numerical results in BM

A comparison of the crack shape between the experimental (in black) and the numerical (in white) results are presented in Figure 4.10 for an average crack extension $\Delta a \approx 1.13$ mm. Both cracks have a thumbnail shape with a longer crack in the mid-thickness plane than at the surfaces of the specimen. Numerically, the crack is symmetric regarding the mid-thickness plane and is a good representation of the experimental one. Figure 4.10 represents an instant in the damage evolution process, that corresponds experimentally to the end of a test. The development of the stable crack across the thickness of the specimen is displayed in Figure 4.11 for different load levels. Crack initiation, labeled by the number

1 in the figure starts in the middle of the specimen at a load of $F \sim 3.5$ kN, well below the maximal force. The location of damage initiation possesses the highest triaxiality ($\eta_{mid} = \sigma_h/\sigma_{eq} \sim 3$). At crack initiation the triaxiality at the surface is more than three times smaller than in the mid-thickness ($\eta_{surf} \sim 0.8$) hence no damaged elements are observed at the specimen surface. As the deformation increases and the difference in triaxiality between the surface and the mid-thickness plane decreases, the crack develops in a tunneling manner. After the maximal load, at event 4, damage has reached the surfaces of the specimen. The results plotted in Figure 4.9 and in Figure 4.11 are identical, note the difference in the CMOD values. To study the development of the crack, larger displacement was imposed in the second case to obtain longer crack. At point 5 in Figure 4.11 $\Delta a = 5.38$ mm.
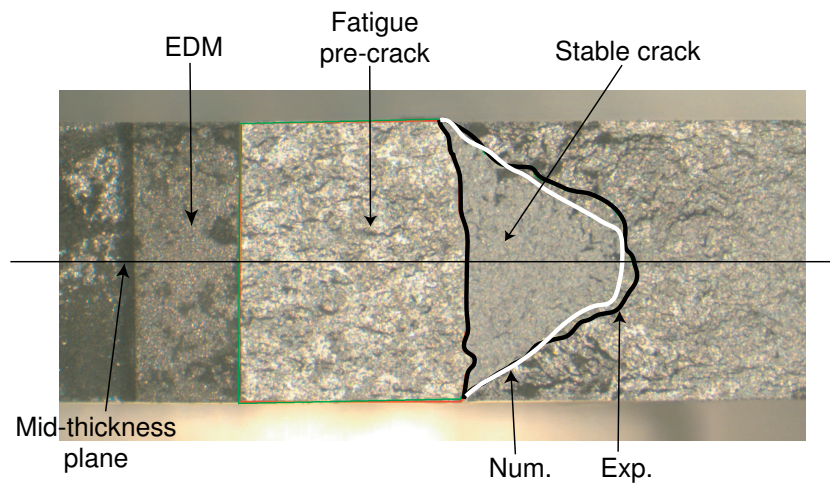
Figure 4.10: Comparison of the shape of the stable crack in Al6056 T78 BM (exp.: black line, FE: white line)
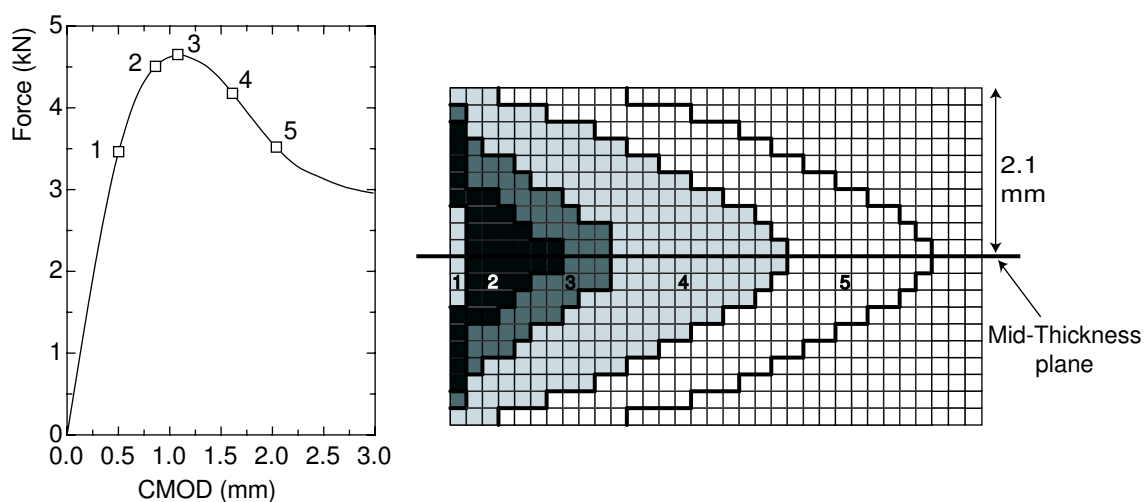
Figure 4.11: Evolution of the numerical crack shape with increase in deformation

4.3   Crack extension in Al6056 T78 fusion zone

In the configuration of crack extension in the fusion zone, the initial crack is assumed in the middle of the weld metal strip of a compact tension specimen ($W = 50$ mm, $a/W = 0.5$ and $B = 4.2$ mm), as schematically shown in Figure 4.12.

Again only a fourth of the C(T)-specimen is meshed because symmetry conditions can be applied. The crack is introduced in the middle of the FZ and the HAZ possesses identical shape, size and mechanical properties on each side of the weld. The shape of the FZ in the specimen thickness direction is simplified in the FE-mesh. The V-shape of the Al6056 T78 weld, as shown in Figure 3.2 is idealised by a simple strip model. Consequently, the 3D-mesh consists of a simple extrusion of the 2D-mesh displayed in Figure 4.12 in the specimen thickness direction divided into 10 layers. A 3D-representation of the FE-mesh is shown in Figure 4.12.
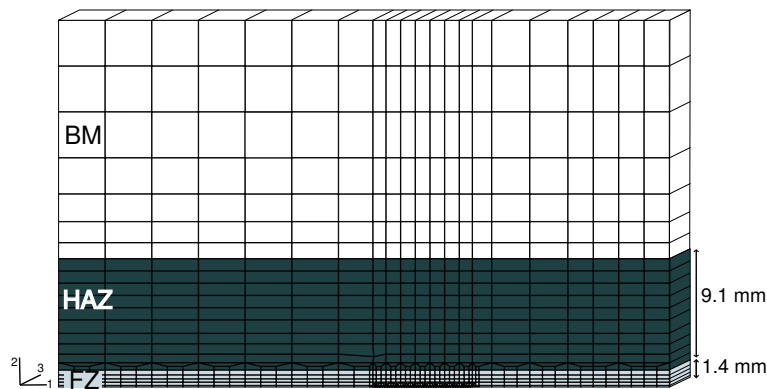
Figure 4.12: 3D-mesh used in the simulation of crack extension in the fusion zone

Three main zones are marked: BM in white, HAZ in dark grey and FZ in light grey. The HAZ is further subdivided into six smaller regions, named HAZ1 to HAZ6. HAZ1 and HAZ6 are adjacent to the FZ and to the BM, respectively. These 6 different zones of the HAZ reflect the variations of the mechanical properties of the experimental heat affected zone. Each HAZ region is chosen to be representative of a significant change according to the hardness measurement and to the tensile data. The dimensions of the various zones are determined from the hardness measurement, indicating changes in proof and ultimate strength. Figure 4.13 explains the selection process of the MFT results used to characterise the mechanical behaviour of the predefined regions. The dimensions of the various regions are given in Table 4.2. The real height of each zone corresponds to the height established from Figure 4.13, whereas the height used in the model gives the sizes used in the FE-mesh. The FZ measures 1.4 mm (half of the experimental FZ height) and the whole HAZ is 9.1 mm high, the remaining part of the C(T)-specimen is constituted of BM.
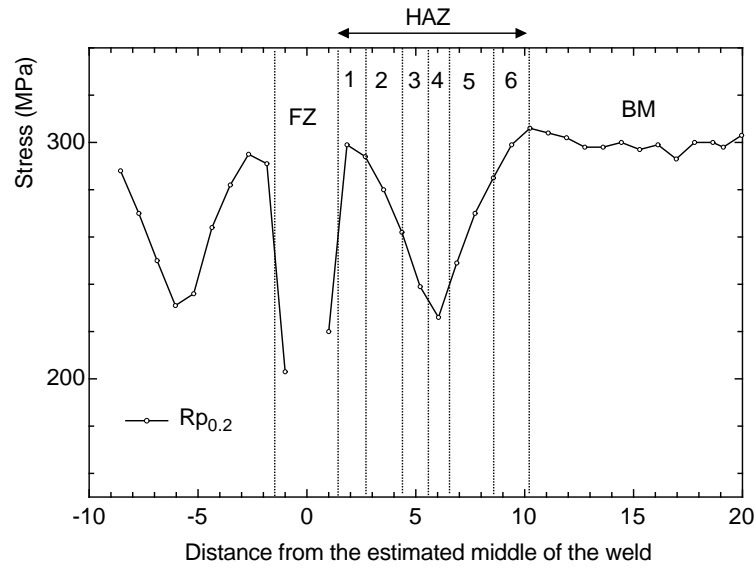
Figure 4.13: Schematic of the construction of the various regions within the laser weld used in the FE-simulations

Material designation	σ_0 (MPa)	real height (mm)	height used in the model (mm)	hardness Hv
FZ	200.0	2.8	1.4	90.7
HAZ1	294.0	1.28	1.3	106.8
HAZ2	280.0	1.68	1.7	117.2
HAZ3	239.0	1.14	1.1	108.4
HAZ4	226.0	1.0	1.0	99.9
HAZ5	270.0	2.06	2.0	102.6
HAZ6	299.0	1.68	2.0	113.6
BM	302.0			120.1

Table 4.2: Definition of the materials in the FE-model

For this configuration, the element size at the crack tip is 200*35*210 μm^3 ($w * D * b$). The element height is reduced compared to the one used in the previous configuration (crack in base material) due to the smaller nearest neighbour distance of particles present in the FZ (factor of 4), see section 4.1.1.

The GTN-model is applied to simulate the crack extension in the FZ. Experiments show that the crack extends within the fusion zone when initially introduced in the middle of the weld metal strip. Therefore, only the fusion zone is modelled using the GTN law, the materials in the HAZ and the base metal are considered elastic-plastic with variation of the hardening behaviour between each zone. The yield strength of each region is provided in Table 4.2. The BM hardening behaviour used in the simulation is identical to the one used in section 4.2. The true stress-plastic strain curves used in the simulations are presented in Figure 4.14. The hardening behaviour is considered identical for HAZ1, HAZ6 and BM and therefore only the BM curve is presented on the graph. Due to the low ductility of the

materials, extrapolation of the experimental data is required to ensure large scale yielding calculation. The extrapolation is realised using a power law following the Ludwik equation, see Eq. (4.4). In the FE-simulation, the plastic deformation is principally confined within the fusion zone and the maximal plastic strain observed in the other regions of the weld does not exceed 0.4%.
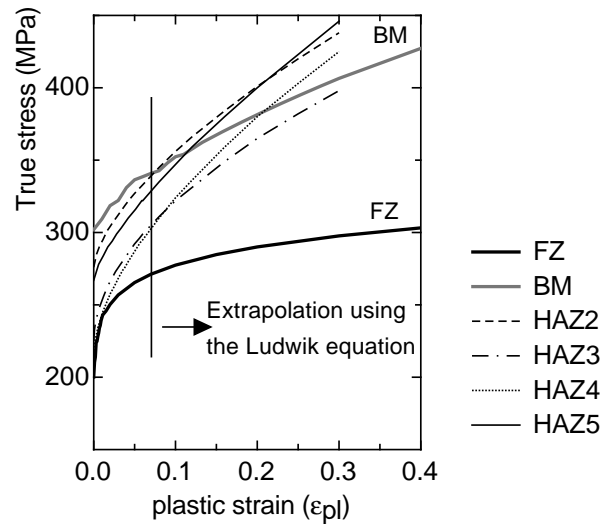

Figure 4.14: True stress vs. plastic strain for the various regions of the weld

The GTN-parameters used for the weld material are: $f_0 = 0.035$, $f_c = 0.16$, $\kappa = 3$, $q_1 = 1.5$ and $q_2 = 1.1$. Comparison of experimental and numerical results are presented in Figure 4.15 in terms of force-CMOD curves and δ_5-Δa fracture resistance curves. A calculation using elastic-plastic behaviour following a von Mises potential law is also shown in Figure 4.15a and labeled "3D-elpl". The load at which the two curves 3D-elpl and GTN differ is below the maximum load and corresponds to the initiation of damage. The numerical maximal load is again slightly underestimated, Figure 4.15a. However, the numerical obtained R-curve fits well the one taken from experiment, see Figure 4.15b.

The shape of the stable crack in Al6056 T78 FZ is presented in Figure 4.16 for a crack extension $\Delta a = 1.3$ mm. The whole specimen thickness is displayed. Tunneling of the crack occurs with a longer crack in the mid-thickness plane of the specimen. The simulated crack shape, in white in Figure 4.16 underestimates the tunneling of the crack but does also present a "triangular" crack shape.
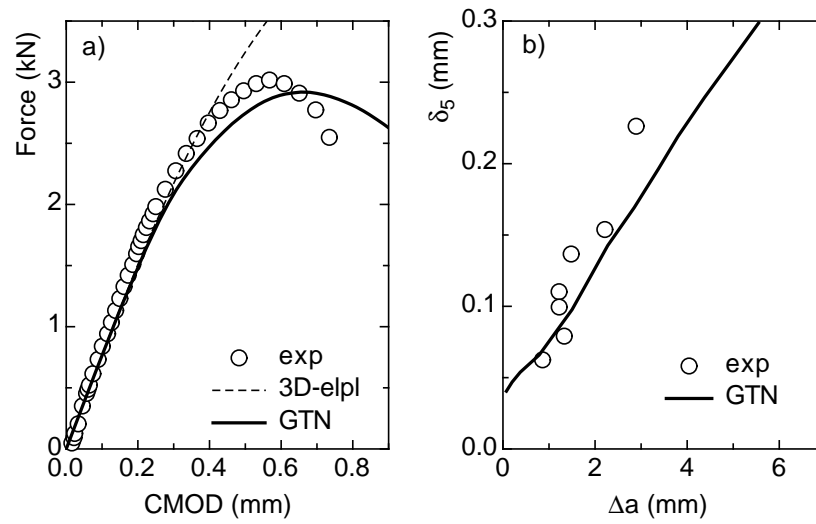
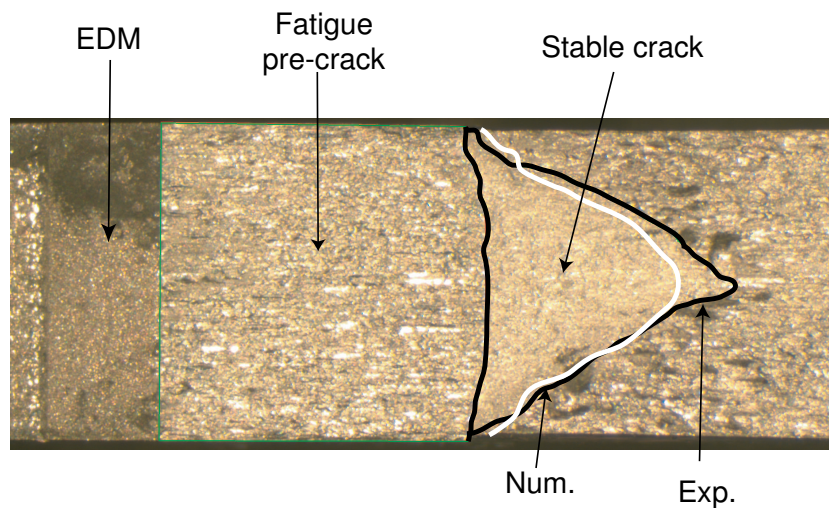Figure 4.15: Comparison between experimental and numerical results in FZ

Figure 4.16: Comparison of experimental (black line) and numerical (white line) crack shape in FZ

4.4   Transfer of GTN parameters between various specimens

Though several authors [15, 22] have successfully simulated various specimen geometries (tensile or bending; ligament length and specimen thickness variations) using a unique set of GTN-parameters, the question of the transferability of the GTN-parameters between different fracture mechanics specimen geometry and size is still open. Due to the concept of computational cells discussed earlier, the transfer of parameters between different structures is possible only by keeping the same FE-mesh ahead of the initial crack tip. The transferability of the GTN-parameters is studied using compact tension specimen of increased thickness ($W = 50$ mm, $a/W = 0.5$ and $B = 6$ mm) in comparison to the studies in sections 4.2 and 4.3. The two homogeneous cases: crack in the BM and crack in the FZ of Al6056 T78 are analysed for this new specimen thickness. The FE-meshes used in this section for BM and for FZ are the 2D-meshes presented in Figure 4.8 and in Figure 4.12, respectively, that are extruded up to a thickness of 3 mm using 15 layers of unique size, $b = 200$ μm. The finite elements at the crack tip have the same 2D dimensions as the ones used in the preceding sections: elements in BM and FZ differ only by their respective height, namely $D = 150$ μm for BM and $D = 35$ μm in the FZ. The GTN-parameters are $f_0 = 0.0115$, $f_c = 0.0195$, $\kappa = 5$, $q_1 = 1.5$ and $q_2 = 1.0$ for the BM configuration and $f_0 = 0.035$, $f_c = 0.16$, $\kappa = 3$, $q_1 = 1.5$ and $q_2 = 1.1$ for the FZ case.

Figure 4.17 shows a comparison between the experimental and numerical results for the two configurations described above in terms of force-CMOD and fracture resistance curve δ_5 vs. Δa. The force-CMOD curves are plotted only for the 6 mm thick specimen whereas the R-curves are plotted for the two specimen thicknesses ($B = 4.2$ and 6 mm). The black circles and the thick line are the data for the 6 mm thick specimens. Δa has been measured only for one 6 mm thick C(T)-specimen made of base metal. In the BM configuration, the load-CMOD curve is well simulated; whereas for an initial crack assumed at the middle of the FZ, the maximal load is slightly overestimated. Both R-curves are also well simulated and reduced fracture resistance curve is obtained for the thicker C(T)-specimens compared to the thinner ones ($b = 4.2$ mm).
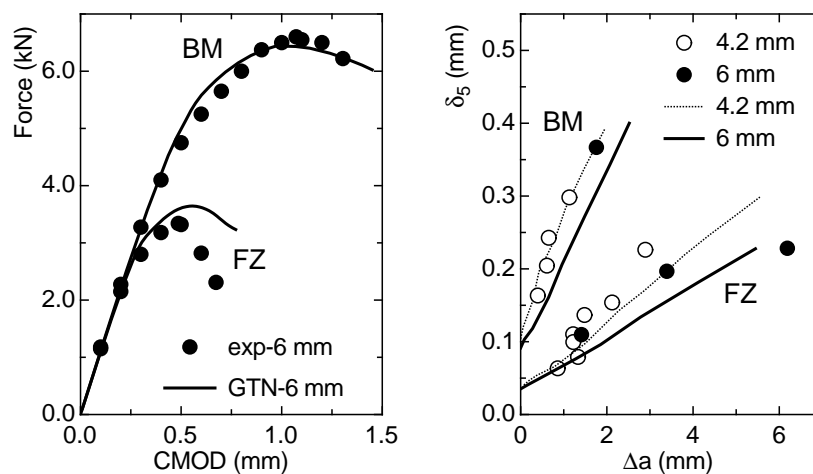

Figure 4.17: Comparison between experimental and numerical results for 6 mm thick C(T)-specimen for both BM and FZ

4.5 Concluding remarks

Crack extension in Al6056 T78 LBW is simulated using the damage model of Gurson, Tvergaard and Needleman (GTN). Two configurations are investigated: initial crack in the base material (BM) and initial crack assumed in the middle of the weld metal strip (FZ). These two cases represent crack extension in homogeneous materials.

The numerous parameters of the damage models are a critical issue. In the formulation used, considering that damage evolution is due only to growth of existing voids, the number of parameters can be reduced in comparison to the complete formulation which takes into account void nucleation, see Chapter 2. A common practice is to identify the initial void volume fraction from metallographic investigations. This initial void volume fraction is assumed to be equal to the volume fraction of the coarse particles present in the aluminium alloy. These large particles fracture or debond from the matrix at low strain. The microstructure in both Al6056 T78 BM and FZ is hence quantitatively examined in terms of particle volume fraction, particle diameter and inter-particle spacing. The amount of particles within the fusion zone is higher than in the base material ($f_0^{BM} = 0.0115$ and $f_0^{FZ} = 0.035$) and their average diameter is smaller than in the BM ($d_{FZ} = 0.7$ μm, $d_{BM} = 3.5$ μm). The established diameter of the inclusions in the BM is of the order of magnitude of data reported in the literature for aluminium 6xxx serie [62, 112].

Following the discussion given at the start of the chapter, the finite element height at the crack tip becomes an additional material parameter. The process zone ahead of the crack, constituted of "computational" cells of height D, is meshed by a unique layer of finite elements. D is dependent of the inter-particle spacing, therefore, the finite element height becomes a function of the particle nearest neighbour distance. Moreover, the R-curve is steeper for BM than for FZ which means that FZ requires less dissipated energy to fracture. The dissipated energy is a volume integral which is proportional to the finite element height. Consequently, the finite elements at the crack tip in the FZ are smaller than in BM. This is confirmed by the microstructural characterisation since the element height is somehow related to the material microstructure: the maximal particle nearest neighbour distance is 4 times smaller in the FZ than in the BM.

An Evolution Strategy algorithm (ES), a mathematical tool to optimise functions, is used to determined the hardening behaviour of both materials in terms of true stress-plastic strain. The ES can separate the respective effects of material hardening due to the strengthening mechanisms and material softening due to damage evolution. A set of model parameters and hardening behaviour is therefore determined for each case studied. i.e Al6056 T78 BM and FZ. The selected parameters provide for both configurations a good fit of the experimental fracture resistance behaviour as well as of the stable crack shape. Slight variations in the initial void volume fraction will have led to other acceptable parameter sets as Zhang [116] pointed out the non-uniqueness of the GTN-model parameters.

The sets of parameters determined on the 4.2 mm thick C(T)-specimen for both BM and FZ are transfered to a thicker specimen ($B = 6$ mm). The numerical fracture resistance curves, in the two cases studied: crack in BM and in FZ, are steeper for the thicker specimens. Regardless of the thin wall state of the two types of specimen ($B = 4.2$ and 6 mm) expressed by $(W - a)/B > 4$, the fracture of the specimens occurs normal to

the loading direction and does not show any crack slanting. In the case of flat fracture, it is expected to obtain a higher fracture resistance in the thinner specimens [85, 88]. Therefore, even if limited experimental data are available, the trend in R-cuves observed numerically is correct.

Comparing the fracture toughness results of the base material and of the weld metal, it appears that the weld material possesses the lowest toughness and a "flat" δ_5 R-curve. These two observations are the consequence of the undermatched weld condition ($M = \sigma_{0FZ}/\sigma_{0BM} = 0.67$). In such undermatched weld with a small fusion zone expressed by the weld slenderness ($(W - a)/H = 17$), the plasticity is confined within the fusion zone and the plastic zone extends out of this region only for long crack extension [59]. Moreover, the mismatch in mechanical properties at the fusion line implies an increase of the constraints at the crack tip. For the Al6056 T78 laser weld, the constraints have been quantified in terms of stress triaxiality $\eta = \sigma_h/\sigma_{eq}$. Within the first finite elements adjacent to the initial crack tip, the maximal triaxiality values, extracted from the simulations, are between 20 to 50 % higher in the FZ case than in the BM, depending on the locations over the specimen thickness. This elevated triaxiality favours damage evolution and "accelerates" crack extension.

The application of the GTN-model in this work may raise several questions as it is applied to thin aluminium panels and to a material in the FZ which does not show spherical voids. The Gurson model is derived for voids whose shape stays spherical as the deformation increases. Consequently, the GTN model has often been applied to thick plates that can be simulated using plane strain elements as the triaxiality is high enough to activate void growth. However, in thin section in which the triaxiality is close to plane stress, the spherical voids tend to grow in a prolate shape [52].
For thin metal sheets, the use of a 3D simulation coupled with an increase of the q_2-parameter is recommended. The 3D calculation allows to take into account the variation of the triaxiality across the specimen thickness and therefore provides a good approximation of the shape of the damage area as void growth takes place at elevated triaxiality locations. Even slant fracture can be simulated by the use of brick elements as demonstrated in Besson et al [10].
The q_2-parameter controls the influence of the hydrostatic pressure and therefore influences the void growth rate. In a unit cell containing a single void, the void growth rate is proportional to the cavity aspect ration [6]. Using the GTN potential to simulate damage evolution, the void growth is a function of the rate of plastic dilatation which is a quadratic function of the q_2-parameter [6, 98]. Thus, the q_2-parameter can be employed to introduce the void shape effect into the "classical" GTN-formulation.
Recent developements of the GTN-model take into consideration non-spherical voids. The plastic potential, as derived by Gologanu [41], introduces a function that accounts for the shape of the void.

The following chapter is dedicated to the study of crack extension of Al6056 T78 LBW in which the initial crack is assumed at the interface between the BM and the FZ. This configuration leads to a more complex state of stress at the crack tip which involves a deflection of the crack.

Chapter 5

Simulation of crack extension in gradient material - The GTN approach

The present chapter is dedicated to the numerical simulation of crack extension in gradient material using the Gurson-Tvergaard-Needleman model. Damage evolution simulated by the GTN-model results from the growth of existing voids.

In an aluminium laser weld, a narrow heat affected zone (HAZ) exists on both sides of the weld metal. The mechanical properties and the microstructure of the materials within the HAZ vary as a function of the distance from the fusion line depending on both the filler material and the weld process parameters. Different regions within the HAZ can therefore be defined in order to describe the gradient in mechanical properties as discussed in the previous chapters. An initial crack, introduced within the HAZ, does not extend perpendicular to the loading direction as in homogeneous materials but towards the softer fusion zone. Such phenomenon has been experimentally observed for the studied Al6056 T78 laser beam weld. The degree of crack deviation has been quantified by topographical investigations of the specimen fracture surfaces, the results are presented in Chapter 3. The location of the initial crack and the occurrence of crack deviation will influence the fracture and damage mechanisms ahead of the crack tip.

In laboratory test specimens, the exact position of the initial crack in the HAZ is not known precisely due to the crater shape of the fusion zone and to the processing methods. As a consequence, in the numerical analysis, the initial crack is positioned at an interface of infinitesimal width between two materials being part of the laser weld either FZ or HAZ or BM. Since the constraints at an interface between two materials are higher than in a homogeneous material, the growth of a crack is a more complex phenomenon. How does the plasticity develop ahead of the crack, which trajectory will be followed by the crack, are frequent questions that need an answer. Such aspects are investigated for the present Al6056 T78 laser weld using a compact tension specimen.

Due to asymmetry in specimen geometry and material properties regarding the crack tip in the (x,y)-plane, one half of the specimen (instead of one quarter as in Chapter 4) is meshed with boundary conditions in the mid-thickness plane. 3D-calculations using 8-node brick elements are carried out. Refer to Chapter 4 for the reasons of the use of 3D

calculations.

The crater shape of the FZ is not represented, the fusion zone is numerically idealised by a metal strip, see Figure 5.1. The width of the fusion zone, determined from the hardness profile, is $2H = 2.8$ mm, simply twice the dimension used in the FZ initial crack configuration.

5.1 Crack extension in Al6056 T78 heat affected zone

The quantitative analysis of crack extension in Al6056 T78 heat affected zone is first simulated using a bi-material configuration, displayed in Figure 5.1a. This configuration represents an idealised Al6056 T78 butt weld which is defined by two zones only: the base material and the fusion zone. The heat affected zone is omitted because, in the analysed Al6056 T78 weld, the material in the first zone surrounding the weld metal, labeled HAZ1 in section 4.3, possesses identical mechanical properties as the parent metal. The initial crack is then introduced at the interface between FZ and BM.

The mechanical properties of both BM and FZ are described in section 3.2.2 and their respective microstructure is detailed in section 3.1. The respective yield strengths of the two materials of Al6056 T78, given in Table 5.1, are $\sigma_{0BM} = 302$ MPa and $\sigma_{0FZ} = 200$ MPa. Their strain hardening exponents are reported in Table 5.1 and are $n = 0.67, 0.25$ for BM and FZ, respectively. These two materials correspond to the materials analysed in the two previous studies on crack extension in homogeneous materials. The mismatch ratio of the weld is $M = \sigma_{0FZ}/\sigma_{0BM} = 0.67$. The BM follows a von Mises law and the GTN-model is applied only in the fusion zone. This simplification is possible because the crack tends to grow from the interface towards the fusion zone even if the GTN-potential is applied in both zones. The GTN-model parameters established in section 4.3 for the fusion zone are transferred to this crack configuration. Consequently the FZ mesh design at the crack tip has to be conserved. The loss of symmetry in the simulation of crack extension at the interface BM/FZ leads to one layer of finite elements to be damaged. Thus the element height at the crack tip in the FZ is taken double compared to the one used in the simulation of crack extension in homogeneous material (Al6056 T78 FZ, section 4.3). The dimensions of the elements are: 70*200*210 μm^3 (height*width*thickness) in the FZ and 150*200*210 μm^3 in the BM zone, respectively. The initial void volume fraction of the weld metal is $f_{0FZ} = 0.035$, the others GTN-parameters are given in Table 5.1.

	zone	zone name	σ_0	n	f_0	f_c	κ	q_1	q_2
Bi-material	FZ	FZ-GTN	200	0.25	0.035	0.16	3	1.5	1.1
	BM	BM-elpl	302	0.67					
Tri-material	FZ	FZ-GTN	200	0.25	0.035	0.16	3	1.5	1.1
	HAZ	BM-GTN	302	0.67	0.0115	0.0195	5	1.5	1.0
	BM	BM-elpl	302	0.67					

Table 5.1: Hardening and GTN-parameters of the FZ, HAZ and BM

The results of the numerical simulations are compared with the experimental ones in Figure 5.1c, d in terms of force vs. CMOD and fracture resistance curve δ_5 vs. Δa. Experimental data of crack extension in HAZ are reported as the black circles. The open

symbols are results of tests on Al6056 T78 FZ. The numerical response is displayed under the name "GTN-bi". The experimental results are underestimated for both experimental plots in Figure 5.1c and b. The used parameters "FZ-GTN" have been determined for a homogeneous material configuration at the crack tip. Because a material mismatch is introduced at the crack tip, characterised by undermatching ($M < 1$), the increased constraint at the crack tip favours crack extension leading to the present results: less fracture resistant material resulting in an overall lower load level.

The significanty higher maximal load obtained from the experimental crack extension "exp-HAZ" compared to "exp-FZ" could also be explained from an initial crack lying in a zone adjacent to the FZ. In fact as the zones change smoothly the assumption of having an interface of infinitesimal width appears unrealistic. To account for this phenomenon, a tri-material configuration is analysed.

In the tri-material configuration, displayed in Figure 5.1b, an additional zone is introduced between FZ and BM in the FE mesh to represent the materials in the HAZ. This additional zone is modelled by a single region which is assumed to follow the GTN constitutive law and whose tensile properties are those of the BM ($\sigma_0 = 302$ MPa and $n = 0.67$) for the following reasons:

- The first region adjacent to the FZ has the main influence on the crack extension of Al6056 T78 heat affected zone. This region called HAZ1, possesses the tensile properties of the BM.

- The yield strength in the HAZ does not increase monotonically from FZ to BM, as depicted in Figure 3.8, but possesses its minimum in the middle of the HAZ. To consider the hardening behaviour of the BM is then conservative because the local mismatch, defined by $m_{local} = \sigma_{0WM}/\sigma_{0HAZ}$ [72], is the lowest possible one resulting in a maximum reduction of fracture resistance of the joint.

- The GTN-parameters have already been established in section 4.2 for the base metal.

Hence two zones (FZ and HAZ) allow for damage evolution. Hereafter, this additional zone is called BM-GTN. A summary of the hardening and the GTN-parameters is given in Table 5.1 for the three materials considered.

To account for uncertainties of the location of the initial crack within the BM-GTN zone, two different zone heights are assumed: using a single finite element layer resulting in a 150 μm high zone or two layers producing a twice as high BM-GTN region: $h_{BM-GTN} = 300$ μm. The first case is labeled "GTN-tri-1" and the second one "GTN-tri-2". In the simulations the crack is forced to initiate in the tougher zone (BM-GTN). Later the crack tilts and propagates into the weaker FZ. This leads macroscopically to a higher load level and a steeper fracture resistance curve, see Figure 5.1c, d. This effect is even more pronounced for the higher zone of tougher material ($h = 300$ μm). The crack has to deviate across two layers, which macroscopically leads to a delayed crack initiation.

Using parameters established for simulating crack extension in homogeneous materials for both BM and FZ, the global behaviour in terms of force vs. CMOD and the fracture resistance in terms of δ_5 vs. Δa of an Al6056 T78 butt joint can be quantiavely predicted being in good agreement with experimental data. However, the results are very sensitive to the location of the initial crack and the crack does not deviate towards the middle of
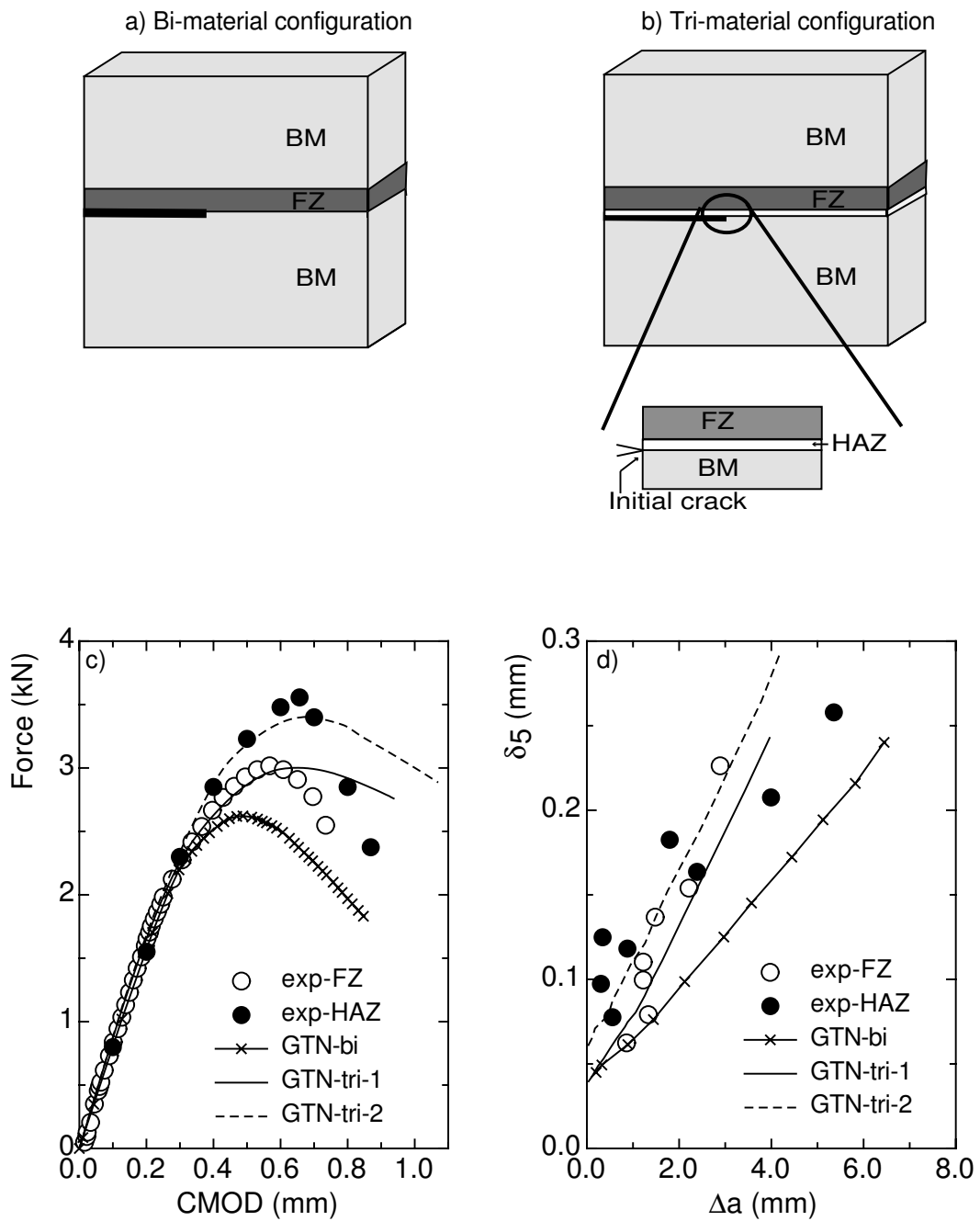
Figure 5.1: Quantitative analysis of HAZ crack, a) schematic of bi-material configuration, b) schematic of tri-material configuration, c) Force-CMOD curve, d) δ_5 vs. Δa R-curves

the fusion zone but extends within the first layer of finite element in the FZ. The rest of the chapter is dedicated to study the numerical occurrence of crack path deviation. First the effect of the numerical parameters such as the GTN-parameters or the mesh design at the crack tip on both the crack trajectory and the fracture toughness of the weld are analysed. Then, the properties of the weld itself in terms of the local mismatch and of the size of the fusion zone are studied.

5.2 Parameter study

The parametric study is carried out using two material configuration: a bi- and a tri-material configuration. The bi-material configuration is identical to the one used in section 5.1 and displayed in Figure 5.1. It allows for reduction of computational time as only a small region, the FZ, is damaging. Since this configuration is used to investigate the influence of the GTN-parameters and the FE-mesh on the fracture behaviour of the joint as well as on the crack trajectory, both the element size at the crack tip and the model parameters will be given in the respective sections.

The tri-material configuration is different from the one used in section 5.1. It is sketched in Figure 5.2. The initial crack is not introduced at the interface HAZ/BM as previously but at the interface FZ/HAZ. The following study being focussed on the damage mechanism taking place within the fusion zone as a function of the weld properties, the material in the HAZ is therefore assumed to be non-damaging. To differentiate this tri-material configuration to the one used in section 5.1, the present configuration is labeled hereafter "tri-material FZ/HAZ configuration".
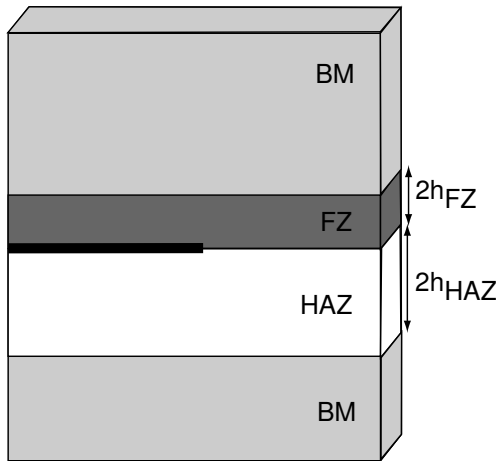
	σ_0 (MPa)	n
FZ	200	0.25
BM	302	0.67
HAZ	variable	variable

Figure 5.2: Tri-material FZ/HAZ config-
uration

Table 5.2: Properties of the materials in the tri-material FZ/HAZ configuration

The width of the HAZ is assumed to be twice as the one of the FZ ($2h_{HAZ} = 2*2h_{FZ} = 5.6$ mm). Von Mises plasticity characterises the material behaviour within the HAZ and the BM, whereas the GTN-model is applied only to the weld metal. Base material and weld metal have mechanical properties described in Chapter 4. The hardening behaviour of the different regions of the tri-material FZ/HAZ configuration are provided in Table 5.2. The GTN-parameters of the weld metal are $f_0 = 0.035$, $f_c = 0.1$, $\kappa = 4$, $q_1 = 1.5$ and $q_2 = 1.0$. The elements at the crack tip are identical in FZ and HAZ ($200*150*210$ μm). It will be shown that this element pattern in the FZ promotes crack path deviation. The use of large finite elements at the crack tip allows also a reduction of the computational time.
The tri-material FZ/HAZ configuration is used to study the influence of the mechanical properties of the material within the HAZ on the fracture behaviour of the weld. The

material within the HAZ is investigated by variation of its yield strength and its hardening behaviour.

Figure 5.3 presents the numerical trajectory of a deviated crack. A 2D view of the mid-thickness plane of the whole mesh is displayed in Figure 5.3a. The elements in the FZ are coloured in blue and the ones in the BM are white. The damaged elements with $f^* \geq 0.9 f_u^*$, marked red in the figures, are zoomed in Figure 5.3b in a 3D representation as the crack extends in all 3 directions. Numerically, the crack extension pattern is given by the discretisation of the finite element mesh. Due to the use of brick elements, the crack deviates from its original plane by moving to an upper layer of finite elements producing steps. The crack trajectory presented in Figure 5.3 is formed by five layers of damaged elements forming four steps.

Each step of deviation will be indicated by a solid circle on the respective fracture resistance curve in the following.
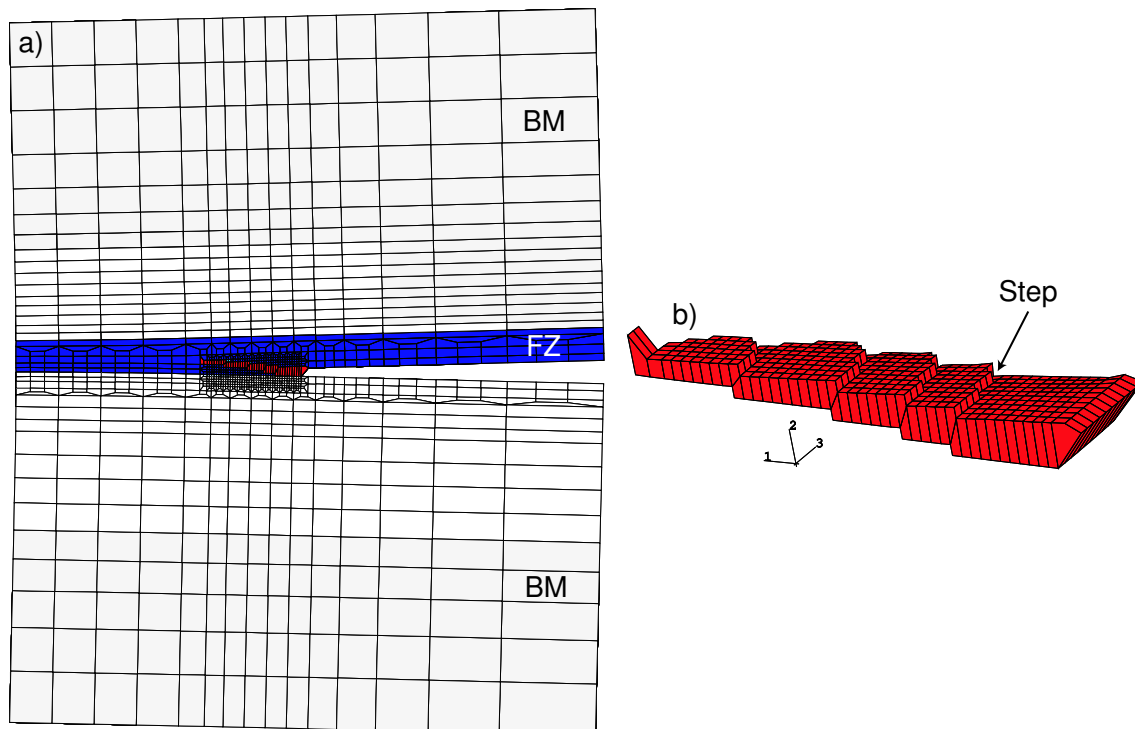
Figure 5.3: Numerical crack extension in FZ showing crack path deviation, a) deformed FE mesh, b) damaged area

Figure 5.3b also shows the "tunneling" of the crack in the specimen centre. An average value of crack extension over the specimen thickness is calculated for the presentation of the fracture resistance curves, $\delta_5(\Delta a)$.

It is worth mentioning that the "true" crack extension is calculated instead of the projection, as it is done in testing, see Figure 5.4. For a deviation angle of 17°, as it is observed on the fracture surfaces (see section 3.3.2), the difference between true and projected crack extension is around 4.5 %, so that any comparison to experimental results is not significantly affected. The deviation angle observed in the numerical simulations is even smaller than 17°.
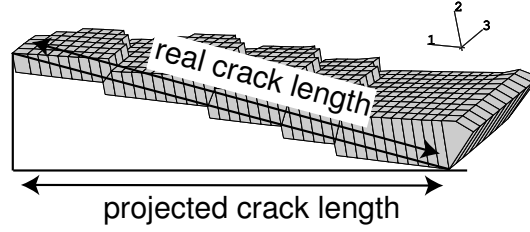
Figure 5.4: Real and projected crack extensions for a deviated crack

5.2.1   Influence of the GTN-parameters on crack path deviation

To verify under which circumstances the crack-path deviation can be reproduced in the numerical simulation, a study of the influence of three GTN-parameters (f_c, q_1 and q_2) on both crack kinking occurrence and on the mechanical response is carried out using the bi-material configuration. These three model parameters are studied because they affect particularly the fracture behaviour.
The FE-meshes are kept as simple as possible and are identical in all cases reported in this section in order to avoid any effects of different mesh discretisations as reported in [9, 104]. At the crack tip, the finite elements have a width (w) of 200 μm, a height (D) of 150 μm and a thickness (b) of 210 μm and they are identical in both zones.

These three GTN-parameters were introduced into the original potential of Gurson [44] by Tvergaard and Needleman [111]. f_c, critical void volume fraction, corresponds to the limit above which void interaction starts, numerically simulated by a phenomenological acceleration of damage governed by κ. The q_i-parameters have been introduced by Tvergaard [107, 106] to bring shear band bifurcation predictions of the Gurson model closer to those observed in numerical analyses of an array of spherical voids in a round tensile bar. By varying q_i, the shape of the yield function is modified. Several authors argued that the q_i-parameters are dependent on the hardening behaviour of the material through both the hardening exponent and the ratio σ_0/E [36, 106]; the strain hardening exponent having the main influence on the q_i parameters. q_1-parameter is involved in the calculation of f_u^* through

$$f_u^* = \frac{q_1 - \sqrt{q_1^2 - q_3}}{q_3} = \frac{1}{q_1} \qquad \text{with} \qquad q_3 = q_1^2 \tag{5.1}$$

thus influencing void coalescence. An increase in q_1, reduces f_u^*, the ultimate value of f^*. The acceleration of damage evolution is also reduced. The q_2-parameter plays a key role in the simulation of crack extension in sheet material as it regulates the influence of the hydrostatic pressure that promotes crack extension.

Influence of f_c

Four values of f_c are analysed, namely $f_c = 0.039, 0.055, 0.075, 0.1$, the other GTN-parameters are kept constant and are: $f_0 = 0.035$, $\kappa = 4$, $q_1 = 1.5$, $q_2 = 1.0$. $f_c = 0.039$ is primarily chosen because such GTN-parameter set gives the best fit between experimental and numerical results for the configuration with an initial crack in the FZ when the finite elements at the crack tip are 150 μm high. The results in terms of δ_5 - Δa fracture

resistance curve are presented in Figure 5.5a. An increase in f_c increases the fracture resistance of the material, the R-curve for $f_c = 0.1$ is the top one, see Figure 5.5a. At crack initiation, the opening of the crack, represented by the δ_{5i} value, is larger for high value of f_c than for smaller ones: $\delta_{i0.1} > \delta_{i0.039}$. The crack extension is easier for low values of f_c.

Crack deviation occurs numerically only for the highest f_c value, for which void growth is large prior to coalescence. In this case, $f_c = 0.1$, the crack deviates twice from layer 1 to layer 2 and further into layer 3, see black dots on the respective curve. The layer 1 corresponds to the ligament layer, layer 2 and 3 are layers above the first layer within the FZ.

The value of $f_c = 0.1$ is chosen to continue the parametric study as this value activates crack path deviation.

Influence of q_1

Variation of the q_1-parameter on the occurrence of crack path deviation is analysed using $q_1 = 1.0, 1.25$ and 1.5 that give $f_u^* = 1.0, 0.8, 0.67$, respectively. The other GTN-parameters are kept constant and are: $f_0 = 0.035$, $f_c = 0.1$, $\kappa = 4$, $q_2 = 1.0$. The results are presented in Figure 5.5b in terms of (δ_5 vs. Δa) curves. An increase of q_1 decreases the f_u^* value, thus the final void volume fraction f_f decreases and fracture of finite element occurs for a lower void volume fraction. Reduced crack tip opening displacement at initiation occurs for large values of q_1 ($\delta_{5i-1.5} > \delta_{5i-1.0}$). Variation of fracture resistance is also observed for the various values of q_1, the extension of the crack is facilitated for large value of q_1, $q_1 = 1.5$. At a given δ_5 value, the crack extension is longer for $q_1 = 1.5$ than for $q_1 = 1.0$.

Decreasing the q_1-parameter triggers crack path deviation (represented by the black circles in Figure 5.5b. For $q_1 = 1.5$ the crack deviates twice towards the third layer, whereas for the two other q_1-values the crack deviates four times towards the fifth layer of finite elements.

As all analysed q_1 values activate the deviation of the crack, the "standard" value of $q_1 = 1.5$ as introduced by Tvergaard is selected for the rest of this section.

Influence of q_2

The q_2-values are $q_2 = 1.0, 1.1$ and 1.2, the other GTN-parameters are: $f_0 = 0.035$, $f_c = 0.1$, $\kappa = 4$, $q_1 = 1.5$. The results are presented in Figure 5.5c in terms of δ_5 vs. Δa. An increase of q_2 influences slightly the crack initiation (δ_{5i}) on the R-curve, but increases dramatically the extension of the crack. This effect can be explained by the increased "triaxiality" consequently to the introduction of the q_2-parameter into the GTN potential, see Eq. (2.26). A high stress triaxiality state promotes crack growth. For the chosen values of q_2, for a given δ_5, up to twice the crack extension is observed between $q_2 = 1.2$ and $q_2 = 1.0$. An increase in q_2 predicts a less fracture resistant material.

Crack deviation occurs numerically for the two smaller q_2 values as presented in Figure 5.5c by the black circles. For $q_2 = 1.0$ the crack deviates twice, from layer 1 into layer 2 and further into layer 3, whereas for $q_2 = 1.1$ crack path deviation occurs only once, from layer 1 into layer 2. At high q_2, the first occurrence of the deviation of the crack takes place at a longer crack extension (Δa) than for smaller q_2 value. This difference in crack

extension was not observed in the case of q_1.

The effect of q_2, on the fracture resistance curve is stronger than the effect of q_1 as the values of q_2 vary only from $q_2 = 1.0$ to $q_2 = 1.2$.
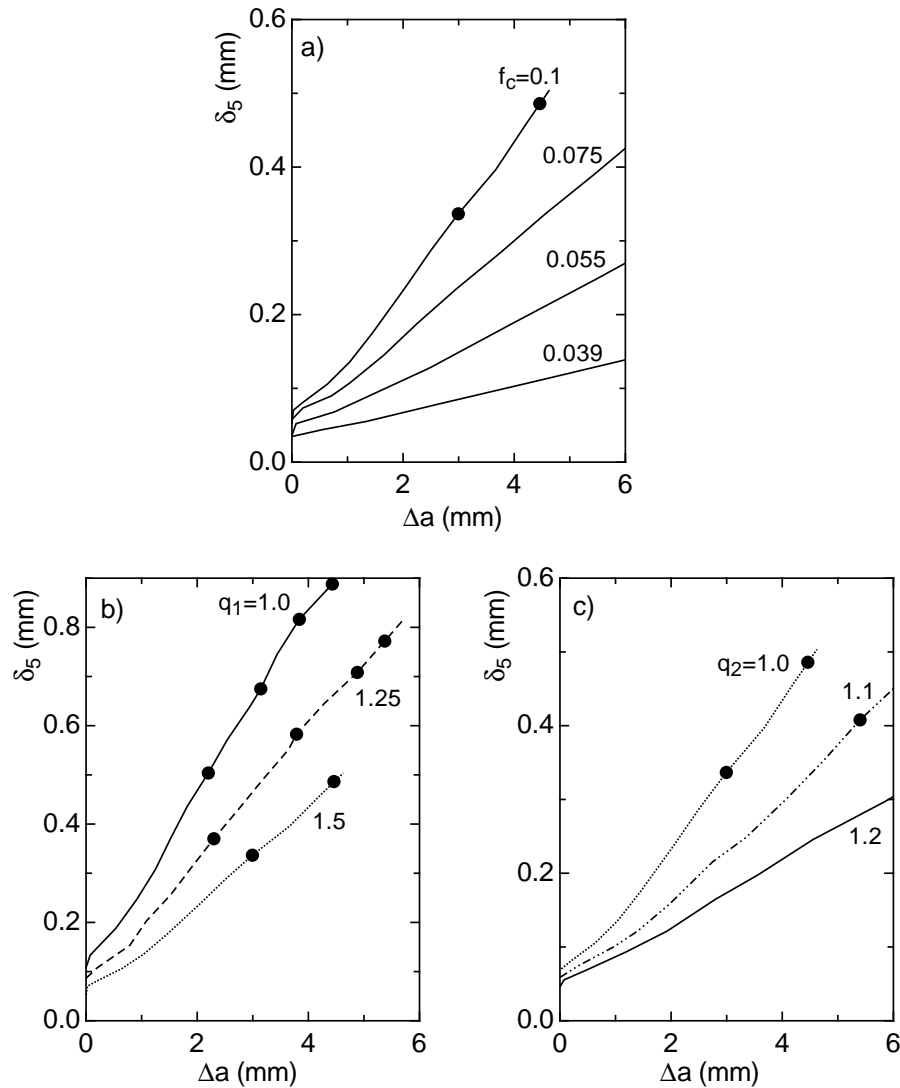

Figure 5.5: Influence of the model-parameters on δ_5 vs. Δa fracture resistance curves, a): f_c, b): q_1-parameter, c): q_2-parameter, • indicates crack path deviation

5.2.2 Reasons for crack path deviation

Crack extension is caused by a combination of hydrostatic pressure and equivalent plastic strain. Due to the low hardening of the Al6056 T78 LBW alloy, a small increase in von Mises stress leads to a large variation of the plastic strain. Therefore both triaxiality and equivalent plastic strain are studied in the following as a function of crack extension with and without crack deviation in order to understand the mechanisms responsible for crack deviation. Both quantities are monitored in the first three layers of the FZ at the mid-plane of the specimen thickness. The mid-plane of the specimen is the location of

intense crack extension and deviation of the crack due to the elevated triaxiality. These two entities are analysed for two of the calculations presented in the previous section in which the occurrence of crack path deviation has been studied with regard to the GTN-model parameters. Crack path deviation is triggered via the parameter q_2, see Figure 5.5c: $q_2 = 1.1$ to let the crack in the simulation deviate from its straight path, $q_2 = 1.2$ to suppress the deviation.

In Figures 5.6a and 5.6b the distribution of the equivalent plastic strain ahead of the crack tip is presented for crack extension with and without kinking of the crack, respectively. Three distributions are presented in Figure 5.6a that correspond to a crack extension of $\Delta a = 0.325$ mm (black), 5.05 mm (red) and 7.4 mm (green). $\Delta a = 5.05$ mm is equivalent to the time increment prior to the deviation of the crack. When no crack path deviation takes place, two extreme crack extensions are considered, namely: $\Delta a = 0.075$ mm (black) and 7.55 mm (green). At the bottom of the figure, in the case of deflection of the crack, the damaged elements are shown for a crack extension of around 7.5 mm. A single step of crack deviation is observed.

The plastic strain is maximal in the layer containing the actual crack tip. At the onset of crack extension, in both cases, the plastic strain is higher in the first layer of finite elements in the FZ than in the layers above. For longer crack, in Figure 5.6a, the equivalent plastic strain becomes highest in the second layer. This coincides with crack deviation. At a distance of ~ 7.5 mm, the plastic strain is higher in the third layer suggesting the formation of a second step of crack kinking. For the configuration with straight crack, Figure 5.6b, the maximum plastic strain remains in the first layer. "Crossing" of plastic strain between layer 1 and layer 2 is observed for a crack extension of 9 mm. This might cause crack path deviation for further crack extension, $\Delta a > 9$ mm, but the calculations have not been run for such crack extension.
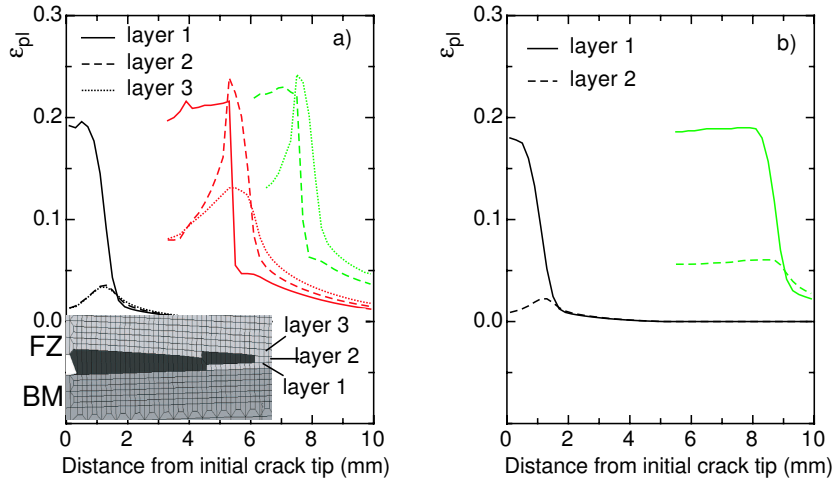
Figure 5.6: Plastic strain at the crack tip with crack path deviation (a), without crack path deviation (b)

The distribution of the triaxiality is plotted in Figure 5.7 versus the distance from the initial crack tip for the two configurations analysed. As the distance from the crack tip increases, the triaxiality level decreases. This observation is general for any fracture mechanics specimen made of material with homogeneous or mismatched mechanical properties.

A value of $\eta = 3.0$ is common at the crack tip of a C(T)-specimen at the mid-thickness plane. At crack initiation, the triaxiality is highest in layer 1. As the crack extends and deviates into the third layer, Figure 5.7a, the triaxiality is lowest in the first layer. Crack extension in layer 1 is not possible anymore, as void growth is limited and localisation of strain takes place within the layer 2 and further 3. Figure 5.7b corresponds to the non deviation case. The triaxiality has its highest value in layer 1 throughout the whole crack extension process. For any crack extension, no crossing of the triaxiality state is observed.
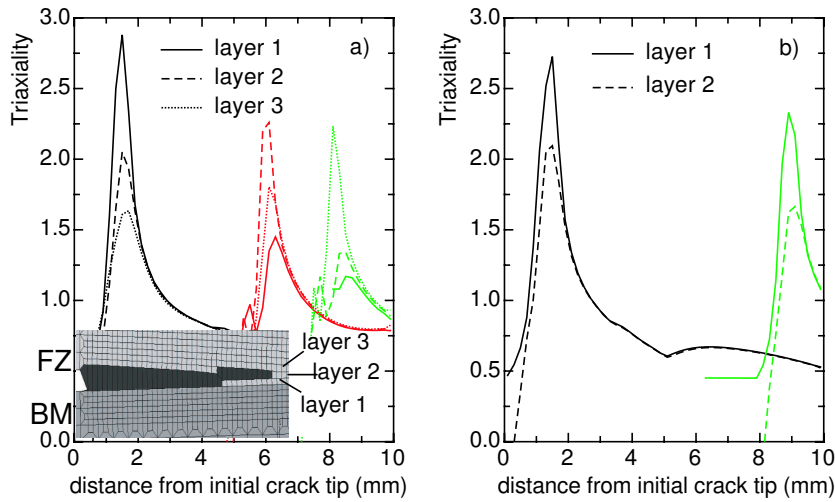
Figure 5.7: Triaxiality at the crack tip with crack path deviation (a), without crack path deviation (b)

5.2.3 Influence of the mesh design at the crack tip

Crack trajectories are numerically controlled by the discretisation of the finite element mesh ahead of the crack tip independently of the type of damage models employed [29, 9, 104]. Using porosity based models, Besson et al [9, 10] found that deflection of the crack as in slant fracture, is achieved by the preferential use of quadratic elements rather than of triangular elements.

The effect of the finite element dimensions ahead of the crack tip is therefore analysed for 8-node brick elements using the bi-material configuration. Variations of the element height (D) and width (w) are considered. They influence, respectively, the energy dissipated per crack extension increment and the stress and strain gradients at the crack tip [8]. The thickness (b) of the elements is identical in the four mesh designs studied, $b = 210 \; \mu$m. In the following, the dimensions of the elements within the base material zone at the crack tip are fixed $(200 * 150 \; \mu$m, $w * D)$; only the size of the elements within the fusion zone varies. Four different finite element patterns are meshed in the FZ, their dimensions are given in Table 5.3 and the element patterns are outlined in Figure 5.8. The white elements are part of the BM whereas the light grey ones belong to the FZ. $D = 70 \; \mu$m corresponds to the height of the elements at the crack tip in the FZ initial crack configuration mesh when no boundary conditions in the specimen ligament are applied. In the case of element

patterns b and c, in which the element widths at the crack tip are different on each side of the interface, a "TIED" function is employed. The "TIED" function implemented in ABAQUS permits to join together elements of different size by assembling the element surfaces and not as traditionally the elements nodes. More details on this function can be found in the ABAQUS standard manuals [45].

element pattern	w (μm)	D (μm)	b (μm)	aspect ratio h/w
a	200	150	210	0.75
b	70	150	210	2.14
c	70	70	210	1
d	200	70	210	0.35

Table 5.3: Dimensions of the finite elements in the FZ

Again, the BM follows a von Mises plasticity law, the weld material is the site of damage evolution and therefore, the GTN-model is applied only within the FZ. The parameters that trigger crack path deviation, determined in section 5.2.1 are used and are: $f_0 = 0.035$, $f_c = 0.1$, $\kappa = 4$, $q_1 = 1.5$ and $q_2 = 1.0$
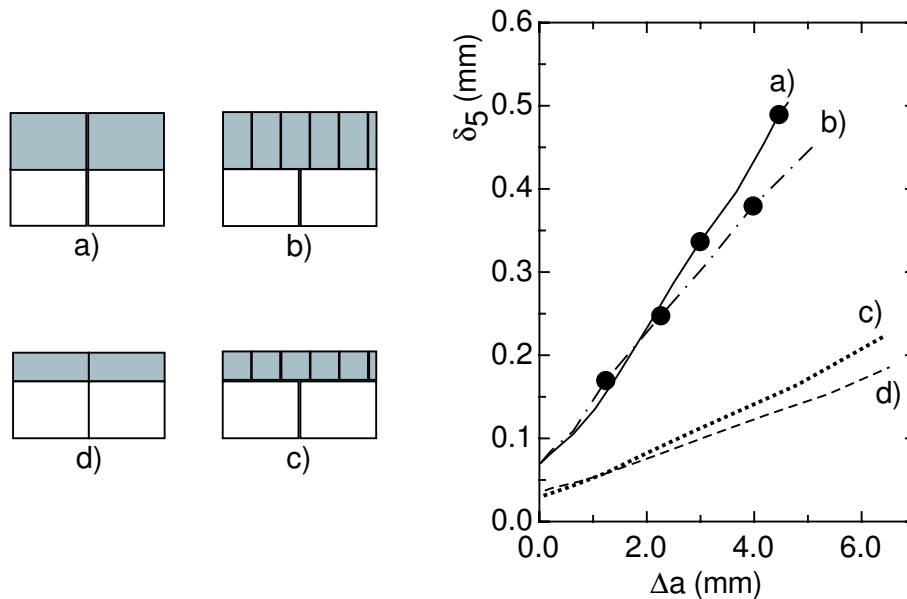
Figure 5.8: Influence of the finite element size at the crack tip on δ_5 vs. Δa curves

The fracture resistance curves in terms of δ_5 vs. Δa are presented in Figure 5.8 for the four finite element patterns analysed. As expected for a constant set of model parameters, the crack initiation value δ_{5i} is smaller in the flatter elements ($D = 70$ μm) than in the tall ones ($D = 150$ μm) due to the reduced dissipated energy in the flat elements. The flat elements have required less mechanical work to separate the two surfaces of the growing crack than the taller ones (for a given crack extension, $\delta_{5-flat} < \delta_{5-tall}$). Therefore the R-curve for the tall elements is steeper than for the short ones. For a given element height, the fracture resistance curves are only slightly influenced by the finite element width.
Crack path deviation occurs only for the taller elements, patterns a and b. For the element pattern a, the crack deviates twice, whereas for elements pattern b, the crack deviates three

times suggesting that vertically elongated elements with an aspect ratio $D/w > 1$ promote the deviation of the crack.

5.2.4 Influence of the position of the initial crack tip

The influence of the position of the initial crack within the fusion zone on the occurrence of crack path deviation is studied using the bi-material configuration. The distance d between the fusion line and the initial crack, sketched at the top of Figure 5.9, defines the exact location of the crack. d takes the values: $d = 0$, 0.6, 0.75, 0.9, 1.2 and 1.4 mm. The two extreme values, $d = 0$ and $d = 1.4$ mm correspond, respectively, to an initial crack introduced along the fusion line (interface between FZ/BM) and in the middle of the fusion zone.

Model parameters are identical as in the previous section, namely: $f_0 = 0.035$, $f_c = 0.1$, $\kappa = 4$, $q_1 = 1.5$ and $q_2 = 1.0$. Since the element pattern b, introduced in section 5.2.3, has been found to promote crack path deviation, such finite elements are applied here at the crack tip within the FZ.

No results in terms of fracture toughness or fracture resistance curves are presented because it was shown experimentally that the fracture resistance curves of the FZ initial crack configuration and HAZ crack case are identical after a small amount of crack extension and any differences in the numerical R-curve could result from numerical artefact. Emphasis is then put on the numerical crack paths which are plotted in Figure 5.9 for the different distances d studied. The damaged elements are displayed in red in the pictures.
The distance $d = 0.9$ mm is found to be a limit above which no more deviation of the crack takes place. For $d < 0.9$ mm, several steps of crack kinking are observed: 5 for $d = 0$ mm, 2 for $d = 0.6$ mm and only 1 for $d = 0.75$ but once $d = 0.9$ mm is reached, the crack develops only in the specimen width direction (x-direction). For distances $d \geq 0.9$ mm, the crack extends within a single finite element layers, again only in the x-direction. The case $d = 1.4$ mm is particular: the initial crack is introduced at the specimen symmetry plane in y-direction. Damage starts within two finite elements on each side of the initial crack. Then, after some crack extension, the crack selects a single layer for its extension, see Figure 5.9.

From this study, it is clear that deviation of the crack is also influenced by the position of the initial crack within the fusion zone of an undermatched weld. When the crack is close to the middle (about 1/3) of the low yield strength region, no more deviation occurs due to some kind of symmetry in mechanical properties and in constraints.
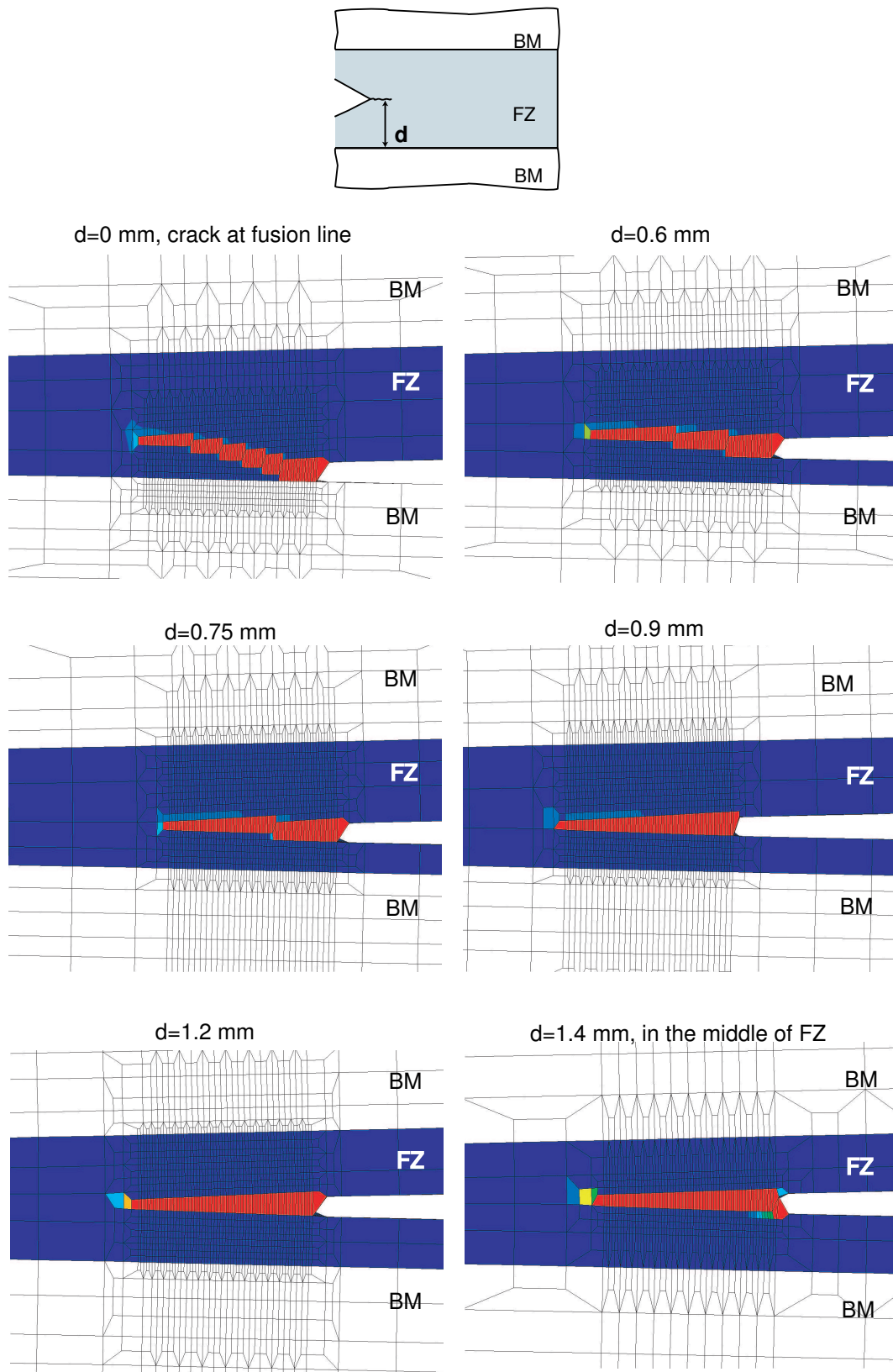
Figure 5.9: Influence of the location of the initial crack as function of the distance from fusion line

5.2.5 Influence of yield strength in the heat affected zone

To study the influence of the yield strength of the material within the heat affected zone, the tri-material FZ/HAZ configuration is used. From the tensile results of micro flat tensile specimens presented in section 3.2.2, the heat affected zone possesses two limits in terms of tensile behaviour: an upper bound corresponding to a material similar to the BM and a lower bound corresponding to the material in the FZ. Yield behaviours ranging between these two boundaries are possible.

The hardening behaviour of the material in the FZ is chosen as reference and three values of yield strength ($\sigma_0 = 200, 250$ and 302 MPa) are analysed. The hardening behaviour is defined by the Ludwik Eq. (4.4) with a strain hardening exponent n, $n = 0.25$. The values of the yield strength are summarised in Table 5.4 and the stress-plastic strain curves for the respective materials are presented in Figure 5.10. The local mismatch ratios varies from evenmatch to undermatch ($m_{local} \leq 1$).

σ_{0HAZ}	σ_{0FZ}	σ_{0BM}	m_{local}	m_{global}
200	200	302	1.0	0.67
250	200	302	0.81	0.67
302	200	302	0.67	0.67
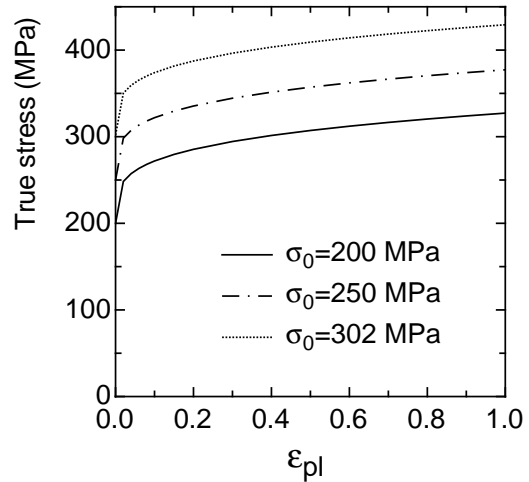
Table 5.4: Material properties of the weld models

Figure 5.10: Strain hardening curve for three values of yield strength: $\sigma_0 = 200, 250$ and 302 MPa

Figure 5.11 presents the δ_5 vs. Δa curves for the three values of yield strength. The strength of the material in the HAZ has little influence on the crack tip opening displacement at crack initiation. As the material in the HAZ becomes stronger (high yield strength), the crack extends more easily within the FZ. For a given δ_5-value the crack extension is longer for $\sigma_{0HAZ} = 302$ MPa than for $\sigma_{0HAZ} = 200$ MPa. A saturation of the influence of the yield strength in the HAZ on the R-curve is observed above $\sigma_{0HAZ} = 250$ MPa. A small variation exists between the two R-curves of the stronger materials ($\sigma_{0HAZ} = 302$ MPa and $\sigma_{0HAZ} = 250$ MPa), whereas between the two softer ones ($\sigma_{0HAZ} = 250$ MPa and $\sigma_{0HAZ} = 200$ MPa), the difference is much more pronounced. A strong material within the HAZ triggers deviation of the crack, represented by the black circles in Figure 5.11. Up to 4 mm crack extension, no deviation of the crack occurs for the two softer materials, whereas for the strongest one with $\sigma_{0HAZ} = 302$ MPa, 5 steps of crack path deviation are observed up to a crack extension of 5 mm. The first occurrence of deflection of the crack takes place at a crack extension of $\Delta a \sim 2.5$ mm. The soft material

configuration can be regarded as a homogeneous configuration as the crack tip is at the interface of two materials having the same hardening behaviour (identical yield strength and strain hardening exponent), hence no deflection of the crack is expected.
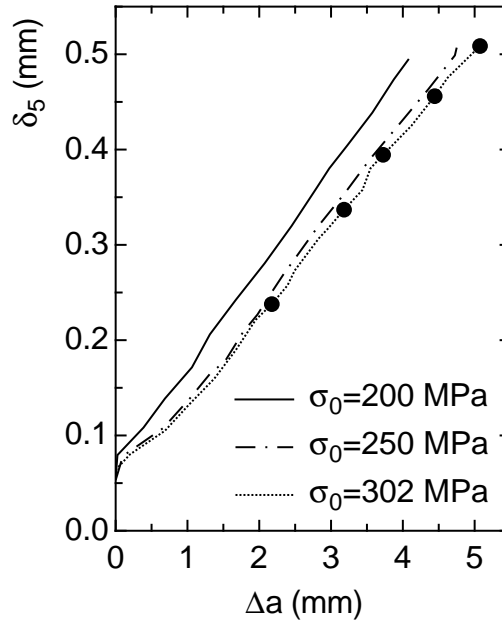
Figure 5.11: Influence of the yield strength in the HAZ on fracture resistance δ_5 vs. Δa curves

The contours of $\epsilon_{pl} = 0.1$ equivalent plastic strain are presented in an undeformed mesh configuration for the three materials analysed, for two crack extensions, namely: $\Delta a = 1$ mm and 3.5 mm, see Figure 5.12. The equivalent plastic strain is measured at the mid-thickness plane of the specimen. As the equivalent plastic strain has low values in the HAZ, for the soft material (black in the figure), no contours are visible except for a long crack extension. Due to the material mismatch, the plastic zone ahead of the crack is not symmetric. At low deformation, the plastic zone is confined within the FZ with an equivalent plastic strain 5 times larger in the FZ than in the HAZ or BM.

For small crack extension, $\Delta a \sim 1$mm, the three plastic zones are nearly identical. The small differences come from the fact that the crack extension is not exactly equal to 1 mm for the three cases studied. Variations of the plastic zones are visible for large crack extension, $\Delta a \sim 3.5$ mm. For the softer material in the HAZ, the plastic zone extends parallel to the interface within the first layers of finite elements. For the strong material for which 6 layers of finite elements are damaged, the plastic zone differs from the two others at a distance of 2 mm from the initial crack tip and reaches the middle of the fusion zone. In the case of the mid-strength material in the HAZ ($\sigma_{0HAZ} = 250$ MPa), the plastic zone tends to deviate also from the interface and therefore for longer crack extension, deviation of the crack would take place.
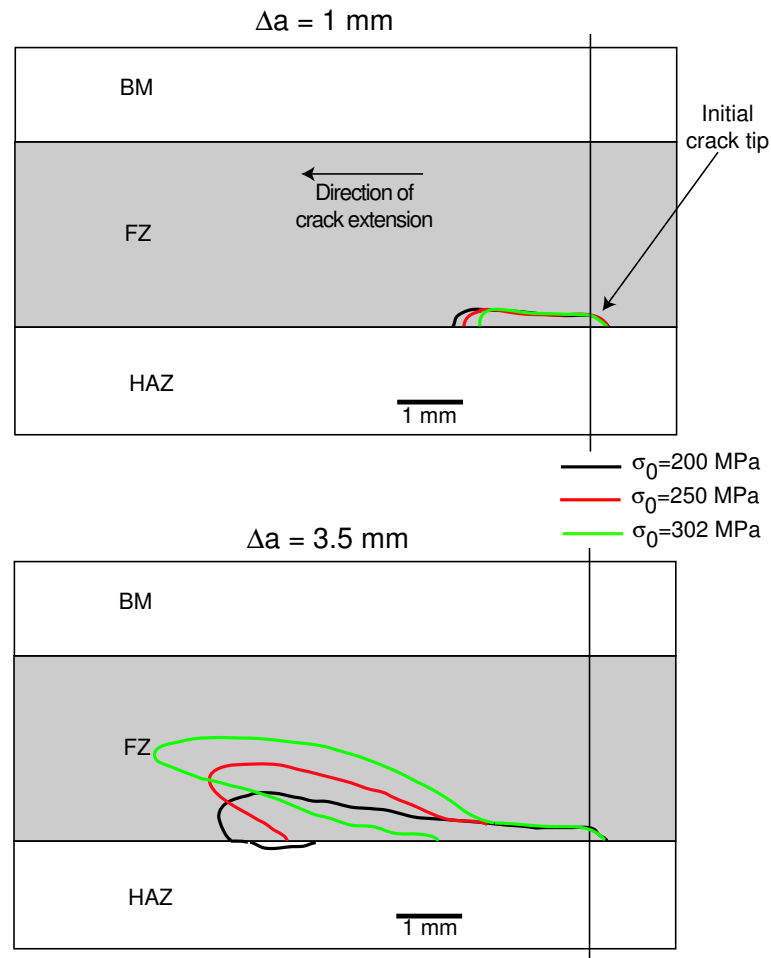
Figure 5.12: Contour of 0.1 plastic strain at the crack tip in the FZ for 2 mm crack extension

5.2.6 Influence of the strain hardening exponent in the heat affected zone

Again, the tri-material FZ/HAZ configuration is used here. The yield strength of the material in the HAZ is kept constant ($\sigma_{0HAZ} = 302$ MPa) and the strain hardening exponent of the Ludwik equation is varied, $n = 0, 0.25$ and 0.67. The stress-plastic strain curves for the three configurations analysed are presented in Figure 5.13a. Both local and global mismatch ratios are identical and undermatched with $m_{local} = m_{global} = 0.67$.

The strain hardening exponent influences slightly the fracture toughness of the weld, see Figure 5.13b. However, the deflection of the crack depends on the strain hardening exponent n. Only one step of deviation is produced by the perfectly plastic material in the HAZ whereas more steps occur for the hardening materials: 2 steps for $n = 0.67$ and 5 steps for $n = 0.25$.

From the two previous investigations, both the yield strength of the material in the HAZ and its strain hardening capacity influence the occurrence of crack path deviation. However, only the strength of the material in the HAZ affects the weld fracture toughness.
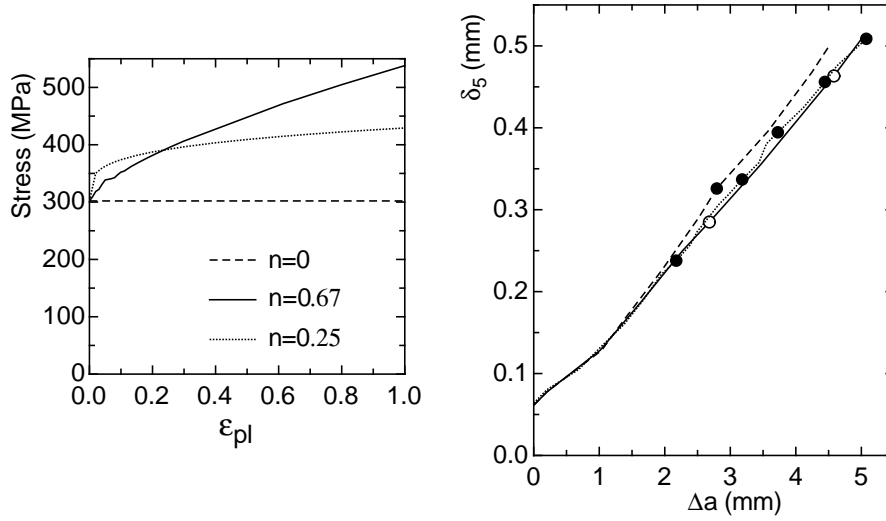
Figure 5.13: Influence of the hardening behaviour in the HAZ on fracture resistance δ_5 vs. Δa curves

5.2.7   Variation of the width of the fusion zone

The size of the FZ depends on the parameters used during the welding process, principally the speed of welding and the laser beam spot size. To consider this effect, the width of the FZ is varied in the following part using the tri-material FZ/HAZ configuration. The reference size of the fusion zone is the one found experimentally: $2h_{FZ} = 2.8$ mm, smaller and larger zones are analysed, namely $2h_{FZ} = 1.4$ and 4.2 mm. The weld slenderness expressed by $(W - a_0)/h_{FZ}$ is another way to describe the size of the fusion zone, $W - a_0$ being the specimen ligament size. The weld slenderness is 35.7, 17.8 and 11.9, respectively. A slender or narrow fusion zone is expressed by an elevated ratio value. The materials within the FZ and the BM are identical as in the preceding section: $\sigma_{0FZ} = 203$ MPa, $n_{FZ} = 0.25$; $\sigma_{0BM} = 302$ MPa, $n_{BM} = 0.67$. The material in the HAZ has been selected according to the precedent results in order to activate crack path deviation. It is characterised by $\sigma_{0HAZ} = 302$ MPa and $n = 0.25$.

The numerical fracture resistance curves in terms of δ_5 vs. Δa are presented in Figure 5.14. The width of the FZ does not influence the crack tip opening displacement at initiation but influences the fracture resistance of the weld. A crack can easily extend within the 1.4 mm wide FZ. For a given δ_5 value, the crack extension is nearly double in the 1.4 mm FZ than in the larger ones. The weld that possesses a large FZ is more fracture resistant than a weld that contains a narrow FZ. A saturation of this effect is observed from a FZ width of 2.8 mm, a small difference in fracture resistance curve exists between the two larger FZs (2.8 and 4.2 mm).

Up to the crack extension calculated, deviation of the crack is observed only for the wider FZs. More steps of deviation occur in the 2.8 mm FZ than in the 4.2 mm one. The crack deviates 5 times in the 2.8 mm FZ and only 3 times in the larger zone (4.2 mm). However, up to 4 mm crack extension, deflection of the crack occurs for identical crack extension in

the case of the two larger zones.

The detrimental loss of fracture resistance of a component with a narrow fusion zone results from the plasticity constraints within the FZ.
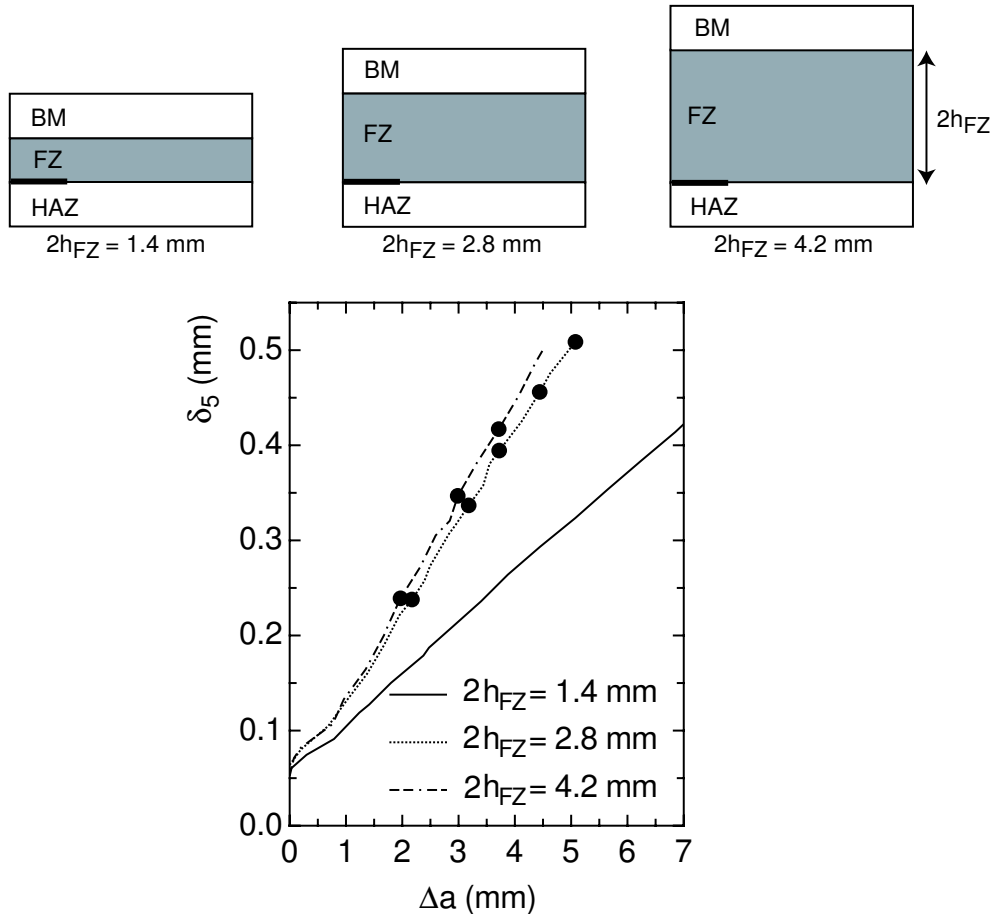
Figure 5.14: Effect of the width of the fusion zone on fracture resistance δ_5 vs. Δa curves

Several contours of equivalent plastic strain are presented in Figure 5.15. The two contours ($\epsilon_{pl} = 0.05$ and $\epsilon_{pl} = 0.1$) are plotted for three crack extensions ($\Delta a = 1.8, 4.5$ and 7.25 mm) for the two extreme sizes of the FZ, namely: $h_{FZ} = 1.4$ and 4.2 mm. The equivalent plastic strain within the HAZ is really small and therefore no contours of $\epsilon_{pl} = 0.05$ are visible on the graph below independently of the FZ width. In the 1.4 mm wide zone, the contours grow in the whole FZ as the crack extends. At $\Delta a = 7.25$ mm, the contour $\epsilon_{pl} = 0.05$ has reached the interface FZ/BM. Contours of equivalent plastic strain smaller than 0.05 could be seen within the BM but are not presented. Moreover as the crack continues to extend, the plastic zone would penetrate into the BM region. For the 4.2 mm large fusion zone, the two contours deviate shortly after the initial crack tip towards the middle of the zone due to the occurrence of deflection of the crack. Once the middle of the FZ is reached, the plastic zone extends mainly in the x-direction. Since the growth of damage is activated by elevated plastic strain, the present results corroborate the ones obtained by analysing the position of the initial crack in section 5.2.4. This phenomenon is even more pronounced for longer crack, see the contour plot of the 4.5 mm crack. However,

contrarily to the narrow zone case, the plastic zone stays within the FZ and does not reach the BM above the weld.
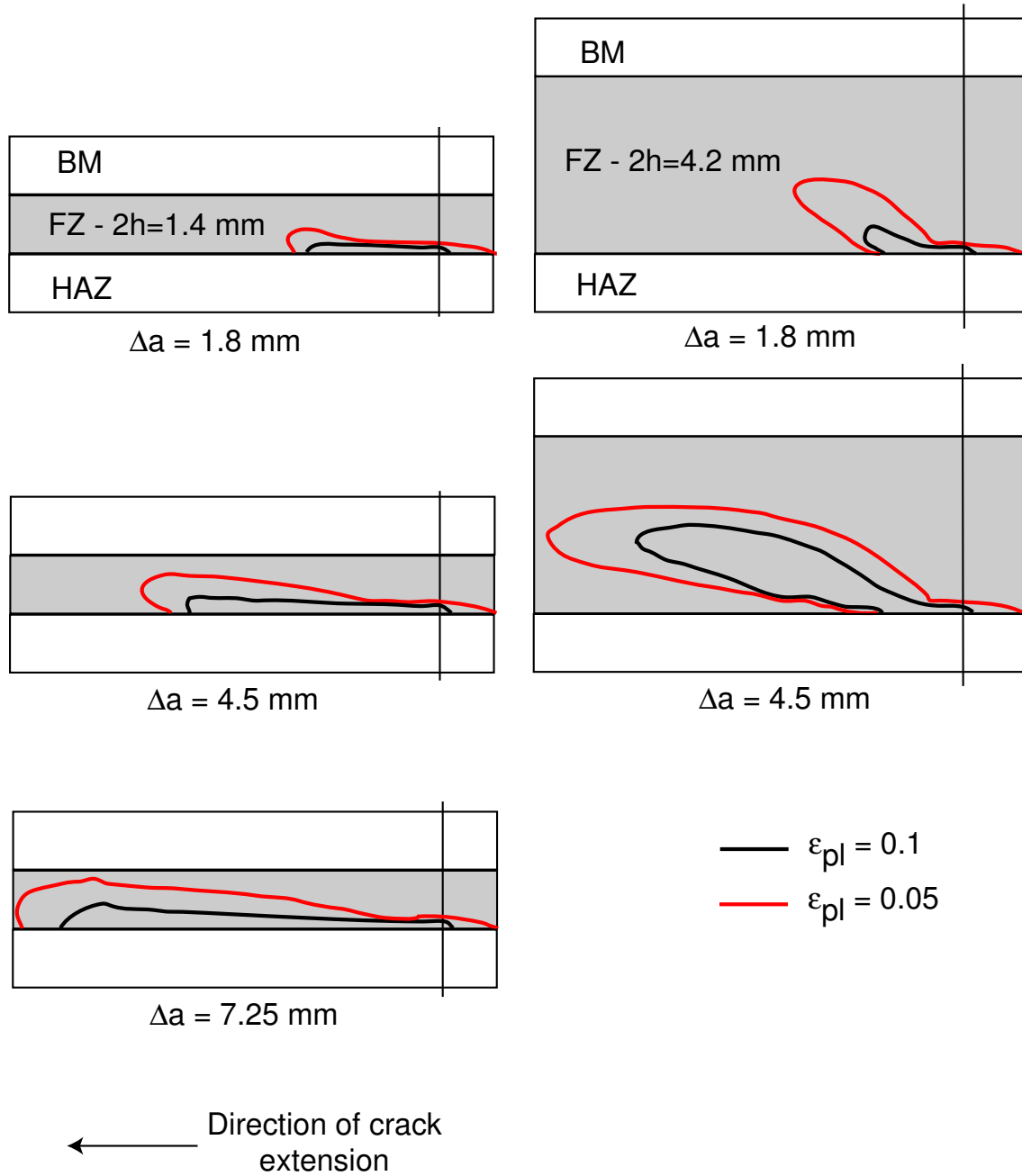
Figure 5.15: Contours of plastic strain (ϵ_{pl}=0.05 (black), ϵ_{pl}=0.1 (red)) for various crack extensions for two different sizes of the FZ

5.3 Concluding remarks

Crack extension along an interface between two material zones has been simulated using the Gurson-Tvergaard-Needleman model. Such configuration represents the case of an initial crack located in the heat affected zone (HAZ). This is of particular interest and practical relevance as cracks in welded components may deviate into regions of lowest strength, i.e the base material for overmatched welds or the weld metal for undermatched welds. Any deviation of the crack path from an orientation normal to the loading significantly affects the macroscopically measured fracture toughness. As the material properties in the HAZ vary quite a lot and the exact location of initial cracks in the tests is not reproducible, numerical simulations have been performed assuming either a bi-material or a tri-material model with an initial crack located at the interface between two material zones.

The investigations demonstrate that crack extension can be successfully simulated by the GTN model for quite sophisticated problems such as welded joints. The fracture resistance of the experimental HAZ crack problem can be quantitatively reproduced by a tri-material configuration in which two regions account for damage evolution, namely the FZ and the HAZ. The HAZ possesses the elastic-plastic damage properties of the BM and the model parameters of the two regions have been determined in the case of homogeneous cracks and transferred to the tri-material configuration. The element height at the interface-crack is however double as the symmetry of the model is lost. The condition of symmetry to the ligament applied in the homogenous configurations means that two rows of elements are actually damaged and thus the total crack extension energy per crack increment is doubled. This model fits the experimental load-CMOD curve and, in particular, the initiation of crack extension quite well for Al6056 T78 LBW.

Numerically, both crack path deviation and fracture resistance of the laser weld are highly influenced by the chosen GTN- parameters and by the mesh design at the crack tip. In this work, deflection of the crack takes place for steep fracture resistance curves which mean high fracture resistant weld. Elevated fracture toughness is obtained for high finite elements at the crack tip. The deviation of the crack occurred here only for the 150 μm high elements and is promoted by vertically elongated elements with an aspect ratio $D/w > 1$, which agrees with the findings of Østby [69].

The three parameters investigated are the critical void volume fraction, f_c and the q_i-parameters with respect to their influence on the load carrying capacity of the weld. For an elevated value of f_c the main part of the damage evolution is the growth of cavities as the coalescence of the voids takes place at large deformation. The fracture resistance curve is therefore steep for high values of f_c and the deviation of the crack is favoured. Furthermore, the crack deviates from its straight path preferentially for small value of q_1 and q_2. The effect on the weld fracture toughness is stronger for the q_2 parameter than for q_1. Variations of q_2 influence the hydrostatic pressure and thus void growth leading to crack extension, whereas variations of q_1 affect the acceleration of damage through κ. Moreover, Faleskog et al [35] demonstrated by unit cell calculations that q_2 affects the collapse of a voided cell. This result was later confirmed by Steglich [100].

Several quantities - element height, f_c and q_i-parameters - affect independently the initiation of the crack in terms of the value of CTOD at initiation: δ_{5i}. The main influence originates from the element height at the crack tip. Moreover, it has been demonstrated

by Xia and Shih [115] and confirmed in this work that the element height is related to the microstructure of the material, is a function of the particle inter-spacing distance . As a consequence, the mesh is first designed and then the model parameters are established. Once the size of the element at the crack tip is fixed, the GTN-parameters have only a slight influence on the δ_{5i} values.

A crack extends preferentially in the direction of high stress triaxiality and elevated plastic strain. Those two quantities affect therefore the deflection of the crack. The crack deviates from its original path if both triaxiality and plastic strain have higher values in the layer adjacent to the one containing the initial crack. Otherwise the crack will propagate in a straight manner within the ligament (first layer of finite elements). Before crack path deviation can take place, a change of the ratios of triaxiality and equivalent plastic strain between the two adjacent layers has to occur.

In order to account for the presence of the HAZ observed experimentally in laser beam welds, an additional zone is introduced between the BM and the FZ. The crack is assumed at the interface FZ/HAZ and therefore the mechanical properties of the material in the HAZ affect the fracture behaviour of the component. Tensile properties of this material are examined by variation of its yield strength and strain hardening exponent. A strong material within the HAZ raises the fracture resistance curve and promotes deflection of the crack. Burstow and Howard [18] and Lin et al [59] analysed the fracture behaviour of various material mismatch ratios of a bi-material crack interface. They found that as the mismatch ratio decreases, i.e. from overmatched ($M = \sigma_{0FZ}/\sigma_{0BM} > 1$) to undermatched welds ($M < 1$), the fracture toughness decreases. Similar effects have been observed here: as the yield strength of the material in the HAZ increases, the local mismatch ratio defined by $m_{local} = \sigma_{0FZ}/\sigma_{0HAZ}$ decreases and flattens the fracture resistance curve. The strain hardening exponent influences the occurrence of crack deviation and does not affect the fracture resistance of the weld.

The strength of the material in the HAZ is important and determines the resistance to fracture of a tri-material interface crack problem. Zhang et al [118] analysed a T-joint and found also that the strength of the material within the HAZ of an aluminum weld influences the loading level of the weld, hence its fracture resistance.

For an interface crack between two materials, the plastic zone is not symmetric, as also reported by Tvergaard [73], due to the mismatch in material properties. In soft materials plasticity will be activated at a lower von Mises stress than in stronger ones. Little plasticity is observed within the HAZ of the studied weld but the dominant plastic zone develops in the fusion zone. Moreover, the plastic zone penetrates the BM, opposite the HAZ, for large crack extension and narrow fusion zone ($h_{FZ} = 1.4$ mm). Lin et al [59] pointed out the importance of the slenderness of the weld ($(W - a)/h_{FZ}$) on the size of the plastic zone ahead of the crack. Similar to here, in an undermatched weld, they found that the plastic zone will extend outside a narrow weld whereas it will spread in a large fusion zone.

The deviation of the crack, promoted by high fracture resistance is related to the plastic strain ahead of the crack tip. The shape of the plastic zone is therefore a function of the crack trajectory. The plastic zone is elongated and close to the interface for straight crack paths whereas in the case of crack deviation the plastic zone grows similarly to the crack, towards the middle of the fusion zone.

Chapter 6

Simulation of crack extension in Aluminium laser weld - Application of the Cohesive Model

Similarly to the simulations carried out with the Gurson-Tvergaard-Needleman model, the fracture toughness of the aluminium Al6056 T78 laser beam weld is simulated using the cohesive zone model considering the three previous initial crack configurations: a crack in homogeneous material is discussed in the two first sections and crack extension at an interface is discussed in section 6.3. The material microstructure and mechanical properties of the different zones of the laser weld have been presented in the previous chapters. Identical hardening behaviours of the materials of the various weld regions as in Chapters 4 and 5 are used. All the following numerical simulations are carried out for a compact tension specimen (C(T)-specimen, $W = 50$ mm, $a/W = 0.5$) with a thickness $B = 4.2$ mm.

6.1 Crack extension in Al6056 T78 base material (BM)

6.1.1 Parameter study

As detailed in section 2.4, the cohesive model possesses two independent parameters: the cohesive energy Γ_0 and the cohesive stress T_0. The separation of the crack surfaces is derived from the two quantities using Eq. (2.30). In this section, the model parameters are kept constant, however two aspects are emphasised: the type of continuum elements adjacent to the cohesive elements and the shape of the traction-separation law.

One fourth of the specimen is meshed using adequate boundaries as discussed in the preceding chapters. The cohesive elements are introduced in the ligament of the C(T)-specimen. The various studies presented below are compared in terms of force-CMOD curve and δ_5 vs. Δa fracture resistance curve. The crack has extended over one entire cohesive element when the element has lost its stress carrying capacity at all Gauss points:

($T = 0$ MPa and $\delta = \delta_0$). Applied to 3D meshes, a physical value of crack extension is determined according to the EFAM GTP procedure on post mortem surfaces [86].

Influence of the Traction-Separation Law

As discussed in section 2.4, the form of the traction-separation law (TSL) has to be defined by the user and might influence the behaviour of the component [109]. For ductile fracture several shapes have been proposed: cubic and exponential by Needleman [64, 65] and a so-called constant stress function by Scheider [81]. The traction-separation law proposed by Scheider has been used throughout this study. Keeping both the cohesive stress and the cohesive energy constant, the parameters δ_1 and δ_2 are varied to change the shape of the TSL.
The different shapes of the TSL are plotted in Figure 6.1, the analysed values of the δ_i parameters are also indicated. The results of this study are plotted in Figure 6.2. It is clear that the shape of the TSL slightly influences both the macroscopic results and the fracture resistance of the material. This variation is even more pronounced in the case of a material that possesses a higher hardening behaviour as observed by the author on non-published numerical simulations. These results are in agreements with the findings from Scheider [82].

Because the analysed Al6056 T78 LBW materials show low ductility: the strain at rupture is around 10 % for the base metal and around 2 % for the weld metal, the TSL displayed in Figure 6.1 by the full line with $\delta_1 = 0.01\delta_0$ and $\delta_2 = 0.05\delta_0$ is used until the end of this chapter to make comparisons between numerical and experimental results.
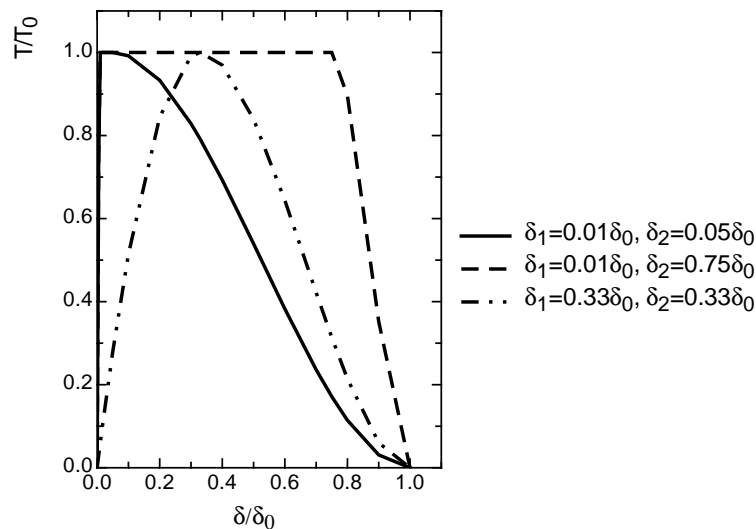
Figure 6.1: Traction separation laws as functions of δ_1- and δ_2-parameters
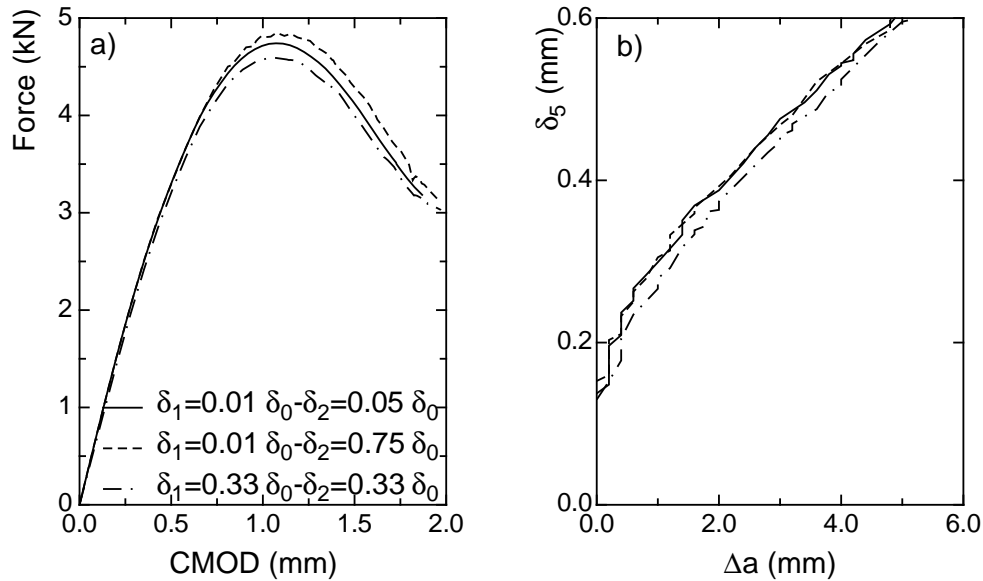
Figure 6.2: Influence of the traction separation law on force vs. CMOD (a) and δ_5-Δa resistance curve (b)

Influence of the continuum elements

Crack extension within the base material is simulated using different continuum elements. First, a convergence study regarding the width of the finite elements at the crack tip is presented. Then the influence of the stress state is considered by using either 2D or 3D elements. The elements are all linear elements with full integration.

To study the influence of the width of the finite elements at the crack tip, two element sizes are analysed: $w = 100 \ \mu m$ and $w = 200 \ \mu m$. The results of the simulation are presented in Figure 6.3. Since there is convergence of the results for both the force-CMOD curve and the fracture resistance curves, the larger elements $w = 200 \ \mu m$ have been selected in the following.

Three types of continuum elements: plane strain elements (CPE4), plane stress elements (CPS4) and 3D elements (C3D8) are used. The names indicated in brackets refer to the denominations used in ABAQUS [45]. The results of the simulation are plotted in Figure 6.4. The initiation of the crack is indicated by the asterisk in Figure 6.4. As expected, the 3D results lie between the two plane calculations. The plane stress and 3D calculations have similar stiffness which is lower than the stiffness of the plane strain simulation. Crack initiation and crack extension are functions of the stress triaxiality at the crack tip, which is higher in the plane strain simulation than in the two others. At the crack tip, the maximal triaxiality is 0.64, 1.11 and 1.75 for plane stress, 3D and plane strain calculation, respectively. The elevated triaxiality in the plane strain elements implies an acceleration of damage producing a rapid crack extension. The plane stress calculation overestimates the results of the 3D calculation since the average triaxiality of the 3D problem is higher than 2/3: the triaxiality introduced by the plane stress elements.
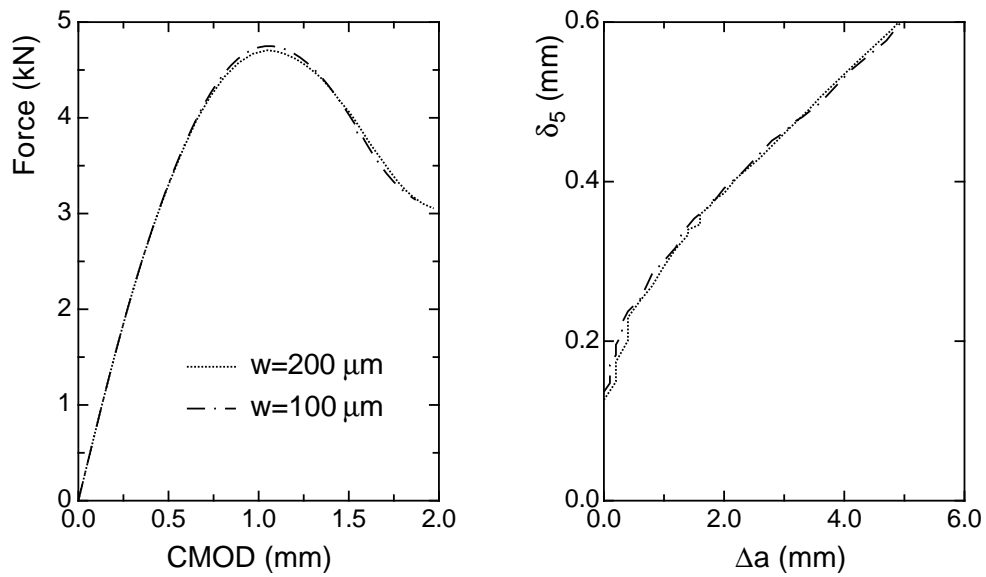
Figure 6.3: Influence of the width of the finite element at the crack tip
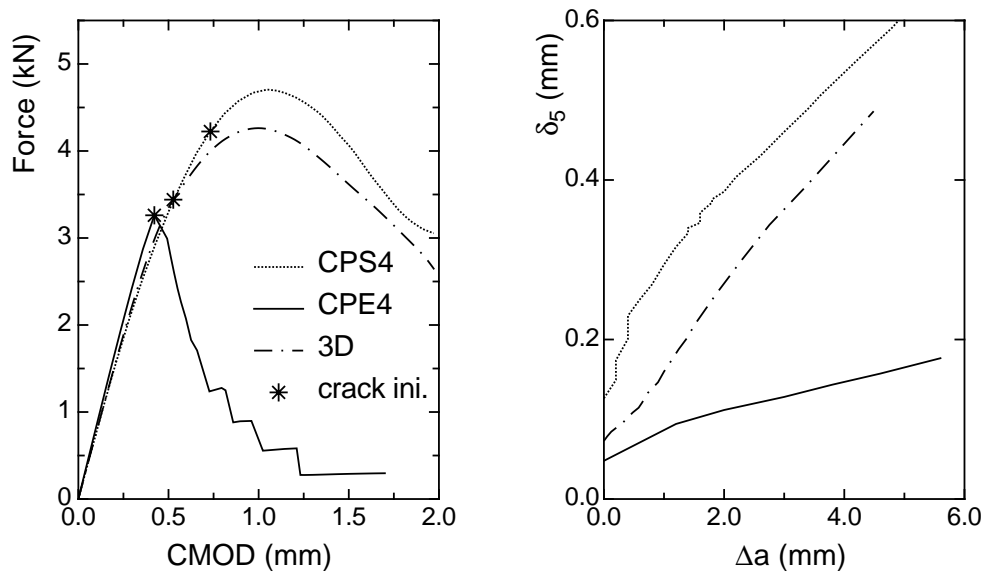
Figure 6.4: Influence of the continuum elements

6.1.2   Comparison with experimental data

3D calculations using C3D8 elements are carried out to simulate the crack extension in the base material of a compact tension specimen (W=50 mm, a/W=0.5, B=4.2 mm). The base material whose properties are described in Chapter 4 is low hardening and its yield behaviour is represented by $\sigma = \sigma_0 + K\epsilon_{pl}^n$, with $\sigma_0 = 302$ MPa and $n = 0.67$. The 2D mesh is identical to the plane mesh used with the GTN-model as shown in Figure 4.8. The cohesive elements are introduced in the ligament of the C(T)-specimen.

Since few experimental data are available to determine the parameters of the cohesive model according to the procedure described in [26] based on experimental tests carried out on mini-bend specimens and mini flat bars specimens with ISO-V notches, some of the information needed is taken from the simulations using the GTN-model, described in Chapter 4. The cohesive energy Γ_0 can be estimated from the value of the J-integral at crack initiation, J_i. In ABAQUS, the contour integral option allows the evaluation of the J-integral values, at each increment, during the calculation. In a 3D analysis, a contour is drawn for each layer in the thickness direction. The value of the J-integral is then calculated as an average value over the thickness. At crack initiation, the J-integral can be calculated this way. If symmetry conditions are applied, $\Gamma_0 = 1/2 * J_i$.

The second parameter to be determined is the cohesive stress, T_0. Unit cell calculations at constant stress triaxiality containing an initial spherical pore have shown that as the imposed triaxiality increases, the maximal mesoscopic stress increases also [7, 95]. At elevated triaxiality as found in thick components, the ratio of the mesoscopic stress over the material yield strength can attain four whereas for smaller triaxiality, around T=1, the maximal mesoscopic stress is around twice the yield strength. Moreover, considering the stress state ahead of the crack tip in thin sheet material, Li and Siegmund [57] established that the opening stress expressed by σ_{yy} is twice the yield strength of the material. Based on these two observations, the cohesive stress is taken as a first approximation twice the base material yield strength: $T_0 = 2\sigma_{0BM} = 600$ MPa.

The preceding approach is macroscopic. A microscopic approach has been proposed in [95] and [97]. The cohesive energy Γ_0 and the cohesive stress T_0 are determined from cell calculations using the GTN-model. At a given triaxiality, the response of the plane strain cell is analysed in terms of σ_e vs. ϵ_e and σ_I vs. ϵ_e. σ_e and ϵ_e are equivalent stress and strain respectively and σ_I is the stress applied in the direction I. The cohesive energy is calculated by $\Gamma_0 = D \int \sigma_e d\epsilon_e$ with D the dimension of the cell. The cohesive stress T_0 equals the maximal value of σ_I. This microscopic approach has not been used in this work.

The results of the simulations are compared with the experimental data in Figure 6.5. The set of parameters: $\Gamma_0 = 25$ N/mm and $T_0 = 600$ MPa produces a too low resistance curve even though the maximal load is well fitted. A better set of cohesive parameters that represents adequately the R-curve is $\Gamma_0 = 30$ N/mm and $T_0 = 570$ MPa. Nevertheless, the reduction of the global behaviour due to damage is underestimated and this for any parameter set tested using 3D simulation. As seen in section 6.1.1, the established set of parameters is valid only under 3D conditions.

6.2 Crack extension in Al6056 T78 fusion zone (FZ)

This initial crack configuration corresponds to an initial crack lying in the middle of the fusion zone. The material within the FZ is characterised by $\sigma_0 = 200$ MPa and $n = 0.25$. Similarly as in section 4.3, the variation of material properties within the HAZ is modelled by six zones. The dimensions of the zones are given in Table 4.2 and the mechanical properties of each region are displayed in Figure 4.14.

Due to the mismatch introduced by the weld, the stress state at the crack tip cannot be well represented by either only plane stress or only plane strain conditions. The simulation
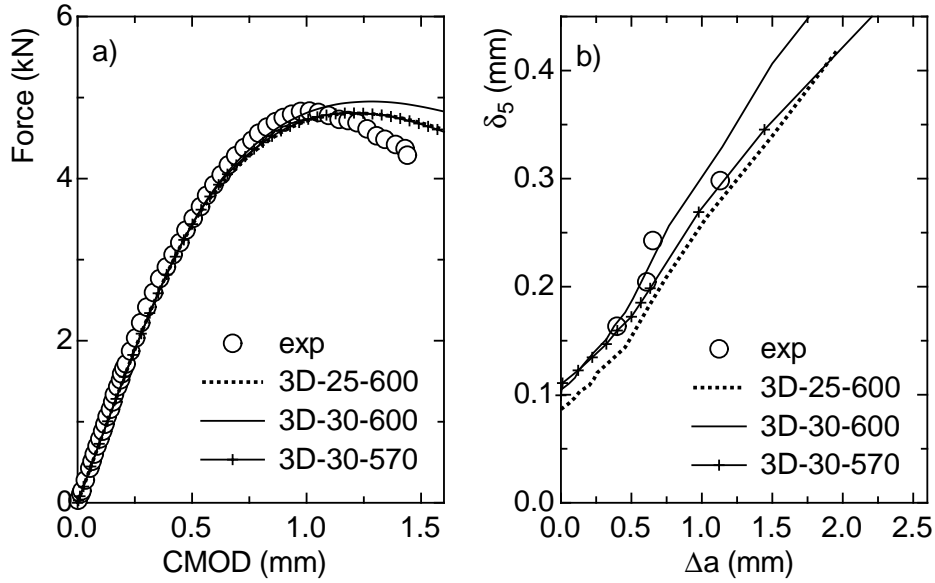
Figure 6.5: Comparison between experimental and FE results in BM

is therefore done using one fourth of the specimen meshed by 3D elements (C3D8). The cohesive elements are implemented as in section 6.1.2 along the specimen ligament. The cohesive parameters have been chosen following an identical procedure as the one used in section 6.1.2. The parameters are $\Gamma_0 = 8$ N/mm and $T_0 = 440$ MPa. The cohesive stress is a little more than twice the yield strength of the material within the fusion zone. The result of the simulation of crack extension in a C(T)-specimen is compared with experimental data in Figure 6.6 in terms of Force vs. CMOD and δ_5 vs. Δa fracture resistance curve. The global behaviour is not well fitted: the maximal load is underestimated and the softening due to damage is underestimated, however, the experimental fracture resistance is well matched.

6.3   Crack extension at the interface FZ/BM

This section is dedicated to the numerical analysis of crack extension using the cohesive model for a crack initially introduced within the heat affected zone of Al6056 T78 LBW of a compact tension specimen (W=50 mm, a/W=0.5, B=4.2 mm).

The tensile properties of the various regions of the Al6056 T78 laser weld have been described in section 3.2.2 and extrapolations of the test results to account for large deformation have been presented. The zone adjacent to the fusion zone and labeled HAZ1 is characterised by the hardening behaviour and yield strength of the base metal. This first region close to the weld metal possesses the main influence on the fracture behaviour of the FZ as local and global mismatch ratios are identical ($m_{local} = \sigma_{0FZ}/\sigma_{0HAZ} = m_{global} = \sigma_{0FZ}/\sigma_{0BM} = 0.67$). As a consequence, the HAZ is omitted in this study and a bi-material configuration is analysed with the initial crack lying at the interface FZ/BM, similarly as was done with the GTN-model. Moreover, this configuration permits to reduce the number of mesh constraints: a fine FE-mesh to represent the different regions in the HAZ is
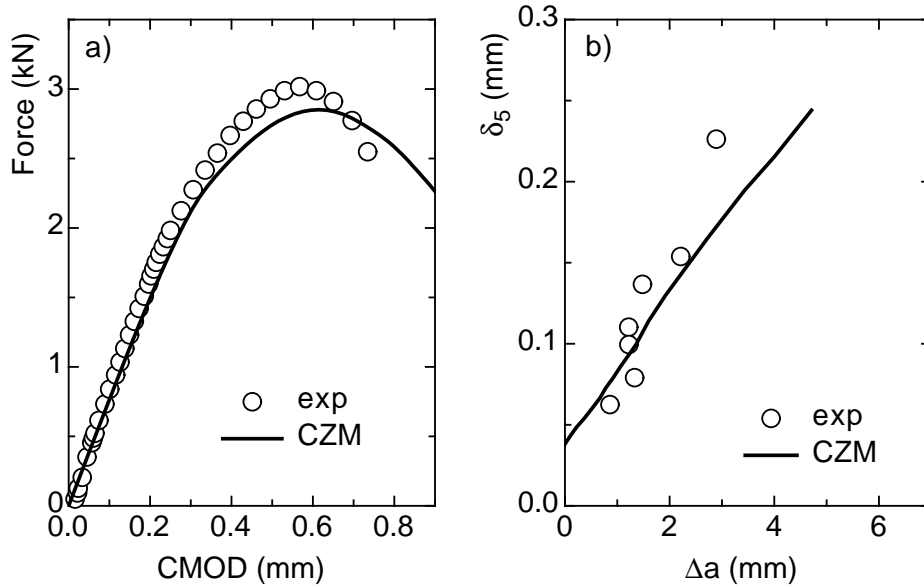
Figure 6.6: Comparison between experimental and numerical results in FZ

not needed. The saved "space" can be allocated to optimise the FE-mesh at the crack tip.

In the FE-mesh, no symmetry conditions are applied in the specimen ligament because of the mismatch in mechanical properties at the crack tip. Therefore, the whole specimen is meshed in the (x-,y-)-plane. Since the crack initially in the heat affected zone deviates experimentally into the weld metal as crack extension takes place, the FE-mesh must also permit deviation of the crack from its original straight path. Therefore, triangular finite elements are used at the crack tip within the fusion zone. Three main crack orientations are possible: along the ligament, normal to the ligament and along a pre-imposed angle given by the finite element aspect ratio. The angle of experimental crack deviation has been identified by topography measurements of the specimen fracture surfaces, its average value is 17°. The triangular elements are then designed in such a way that the desired angle of 17° is formed by the element base and side. An example of the FE-mesh is displayed in Figure 6.7.

Since the pre-processor FEMESH [84] used as mesh generator does not allow for triangular prism elements, no 3D simulations have been performed for this numerical study. An hybrid plane stress-plane strain model is therefore used based on the results of the numerical simulations using the GTN-model and presented in Chapter 5. In the process zone ahead of the crack tip, the stress in the thickness direction, σ_{33}, is nonzero and thus the triaxiality becomes larger than 2/3. The only way to account for this effect in a 2D model is to postulate a plane strain state in the process zone and a plane stress condition in the other part of the specimen. The correct size of the plane strain region becomes an important issue. In order to determine the area of the "plane strain domain", the stresses ahead of the crack tip are analysed based on the 3D calculation of the same interface crack problem with the GTN-model. Since plane stress and plane strain are two limiting cases regarding the stresses in the thickness direction, only σ_{33} is important. If stresses in thickness direction are negligible, plane stress state can be applied. In the other cases, plane strain condition is considered. Due to the constraint in the harder base metal, in
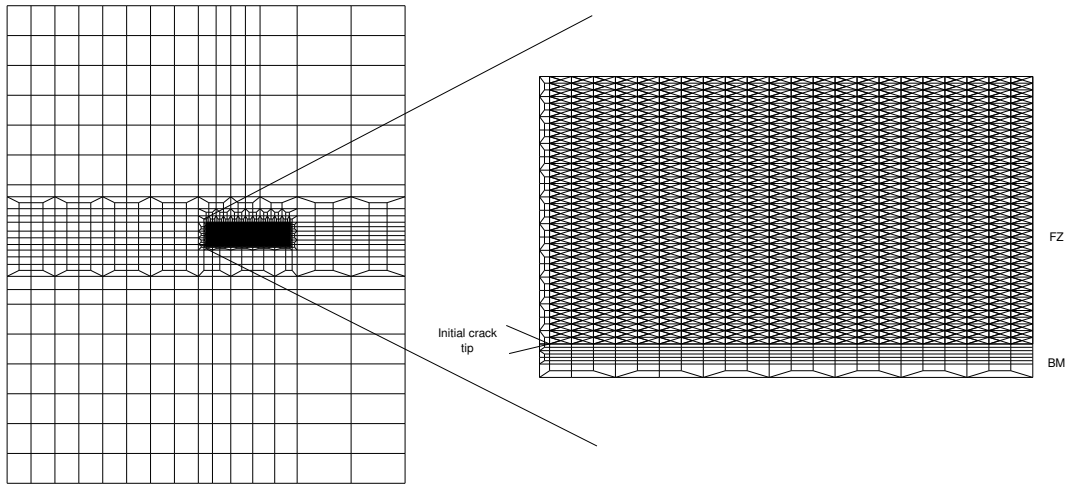
Figure 6.7: Finite element mesh for the initial crack at the interface FZ/BM showing a 17° orientation of the continuum elements

the whole FZ the stresses σ_{33} cannot be ignored. Above the FZ, negligible stresses in the thickness direction are observed. On the other side of the interface, σ_{33} diminishes as the distance from the interface increases. The domain of plane strain finite elements is then defined down to $-0.7 \leq y \leq 2.8$ mm with y being the coordinate perpendicular to the interface ($y = 0$ is the location of the interface).

6.3.1   Comparison with experimental data

To determine the model parameters, the cohesive elements are first introduced only along the 17° direction as presented in Figure 6.8, this configuration is from now labeled "17L". The crack direction is known and imposed in order to eliminate any mesh dependency effect of the results. The parameters are chosen to fit the experimental results of crack extension in HAZ in terms of both force vs. CMOD and fracture resistance curves. Again, the "true" crack extension has been numerically determined. Both tangential and normal separations are considered since the fracture mode is not pure mode I due to the occurrence of crack kinking. The cohesive energies are set identical for both separation modes: $\Gamma_{0N} = \Gamma_{0T} = 20$ N/mm. The tangential stress is lower than the normal one and is taken $T_{0T} = 0.4T_{0N}$ with $T_{0N} = 500$ MPa and $T_{0T} = 200$ MPa. The results of the simulation are presented in Figure 6.8. The level of the maximal load is well fitted. However, the decrease of load due to crack extension is overestimated. No better fit could be achieved, however.

An advantage of the cohesive model resides in the fact that the crack path can be a-priori unknown by the use of special mesh techniques to produce non-ordered mesh. As interface elements, the cohesive elements can be introduced everywhere in the component to be modelled leading to the possibility of multi crack propagation. Tijssens et al [104] and Barpi and Valente [5] pointed out some difficulties by introducing a high amount of cohesive elements within the component: mesh orientation dependency, loss of uniqueness of the equilibrium path and loss of stability.
In the fusion zone, cohesive elements are now introduced between each continnum element as presented in Figure 6.8 to let the crack select its own growth direction and also along
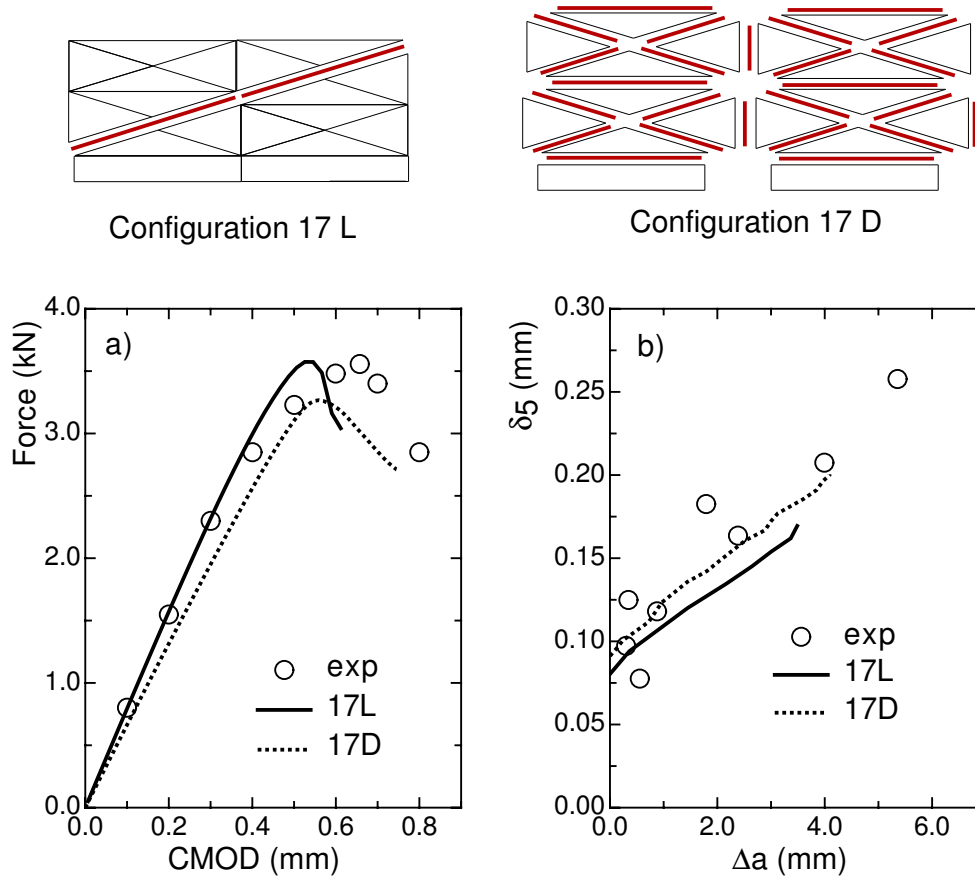
Figure 6.8: Comparison between experimental and numerical results for initial crack at the interface FZ/BM

the interface between FZ and BM, at the specimen ligament. At each cohesive element and at each time increment, the crack can either extend in the direction of the previous time increment or kink. This element arrangement is called hereafter 17D. The model parameters are identical to the ones used in the configuration 17L. The results of the simulation are plotted in Figure 6.8 together with the results from both the 17L simulation and the experiments. The bold lines in the FE-meshes in Figure 6.8 indicate the location of the cohesive elements for the two element configurations studied, i.e. 17L and 17D.

Comparing the two simulations 17L and 17D, it is noted that the number of cohesive elements introduced within the FE mesh has an important effect on both the global behaviour in terms of force vs. CMOD and on the fracture resistance of the specimen. First the overall stiffness decreases as the number of elements augment. The number of cohesive elements in the 17L case is 79 and there are 10680 cohesive elements in the 17D configuration. The stiffness of a single cohesive element is given by the slope of the TSL before the cohesive strength T_0 is reached. In Scheider's cohesive formulation, this slope is governed by the parameter δ_1. As the specimen is loaded, all the cohesive elements present in the component are activated and deform according to the prescribed TSL. The overall stiffness of the specimen decreases as it can be considered as the sum of each unique cohesive element stiffness and energy is dissipated. This phenomenon is amplified by the use of a

large δ_1 value and by an elevated number of cohesive elements. Secondly, as the element arrangement 17D becomes softer in comparison with the 17L one, the overall response of the 17D configuration is lower and the response after the peak load appears more ductile. Up to 4 mm crack extension, the simulation using the 17D element arrangement fits the experimental results in terms of δ_5 vs. Δa fracture resistance curve better.

6.3.2   Variation of the angle of crack path deviation

The experimental angles of deviation, measured by topography, are not constant between several tests but vary between the two limits $10°$ and $25°$. These two angles are assumed for additional numerical simulations. Two respective meshes are generated where the triangular continuum elements form either a $10°$ or a $25°$ angle with the x-axis. The cohesive elements are introduced between all continuum elements as in the 17D arrangement. The two mesh configurations are called 10D and 25D. The crack path is free and the main extension directions are either along the pre-defined crack kinking angle ($10°$ or $25°$) or parallel to the ligament. The cohesive parameters determined in section 6.3.1 are used.

The results of the three simulations are presented in Figure 6.9 in terms of force vs. CMOD and δ_5 vs. Δa fracture resistance curves. The observed crack paths are schematically represented at the top of Figure 6.9. For the 25D configuration, the crack extends along the interface FZ/BM, whereas for the two smaller angles, the crack extends in an inclined way. Two responses are obtained as function of the crack trajectory. When the crack extends in an inclined way, either $10°$ or $17°$, the global behaviour does not depend on the angle. The interface crack extension affects the overall response of the specimen: crack initiation is delayed and the maximal load is higher than for the two others configurations. The fracture resistance curve is nearly not affected by the direction taken by the crack.

6.3.3   Influence of mesh irregularities

The reference FE-mesh 17D is "distorted" in the fusion zone in order to change the angle of possible crack extension at each triangular element. The nodes of the reference 17D mesh are shifted in both x- and y-direction, the mesh is deformed only where the cohesive elements are introduced, its remaining part is identical as in the 17D configuration. Two meshes are created: one is only slightly distorted, it is called "17-ldist", a zoom around this FE-mesh crack tip is displayed in the top left of Figure 6.10; in the second mesh, labeled "17-vdist", the shift of the nodes is greater, a part of the mesh is presented at the bottom left of Figure 6.10. In both 17-ldist and 17-vdist, the maximum shift in y-direction is identical and is less than 1.2%. In the x-direction, the maximum shift is 4.5% for 17-ldist configuration and 8.5% for 17-vdist mesh.

The simulations are carried out using the model parameters determined in section 6.3.1. The results are discussed in terms of crack trajectory and in terms of fracture behaviour. For the 17-ldist case, the mesh being only slightly disturbed, the crack path is identical as in the reference one: along a $17°$ angle from the ligament. The numerical responses of the simulations 17D and 17-ldist are also similar, see Figure 6.11. On the other hand, the 17-vdist node arrangement results in a different crack path: the crack starts to grow along the $17°$ direction and then kinks to run parallel to the ligament. At the kinking location, the angle formed by the triangular element ($\geq 30°$) is too large and the crack chooses to
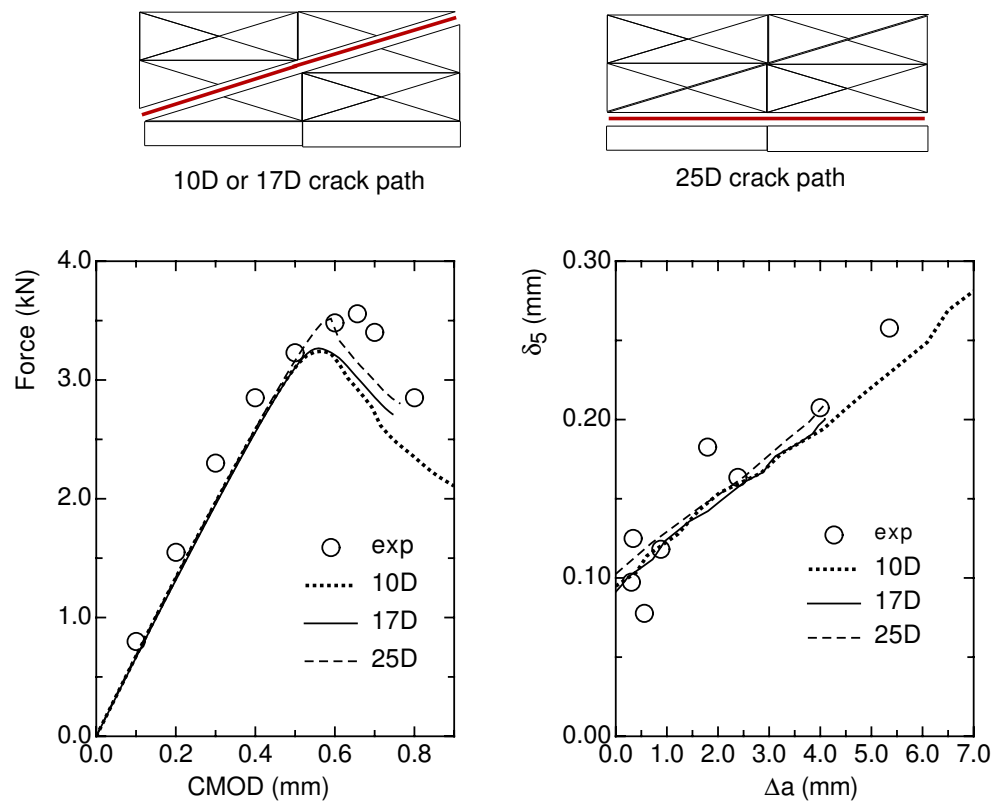
Figure 6.9: Variation of the angle formed by the continuum elements

extend parallel to the x-axis, the energy required to crack growth might be lower in that direction. The change of crack path influences the overall response of the specimen only after the peak load. The softening of the load due to crack extension is more pronounced for 17-vdist. However, the different crack paths do not have a significant effect on the R-curves.

6.3.4   Effect of cohesive parameters

Crack path deviation from the FZ/BM interface can be reproduced numerically using the cohesive model. The previous section demonstrated that the deflection of the crack is a function of the mesh at the "actual" crack tip. During the course of the present work, the author found that the model parameters also influence the direction of the crack independently of the mesh design. Only the effect of the normal traction T_{0N} is discussed next for the bi-material HAZ crack configuration. The bi-material case is identical as in section 6.3.1. The two materials joined at the interface consist of Al6056 T78 base and weld metal.

The following simulations have been carried out using only plane stress finite elements in the entire FE-mesh for two reasons. At the end of the chapter, the stresses ahead of the crack tip are studied for a homogeneous case and for a mismatched configuration. By choosing a unique stress state, any differences between the simulations arise from the constraint effects at the crack tip. Moreover, no comparison with experimental data is

Slightly distorted FE mesh (17-ldist)

Zoom of crack tip
of initial mesh

Deformed mesh

Highly distorted FE mesh (17-vdist)
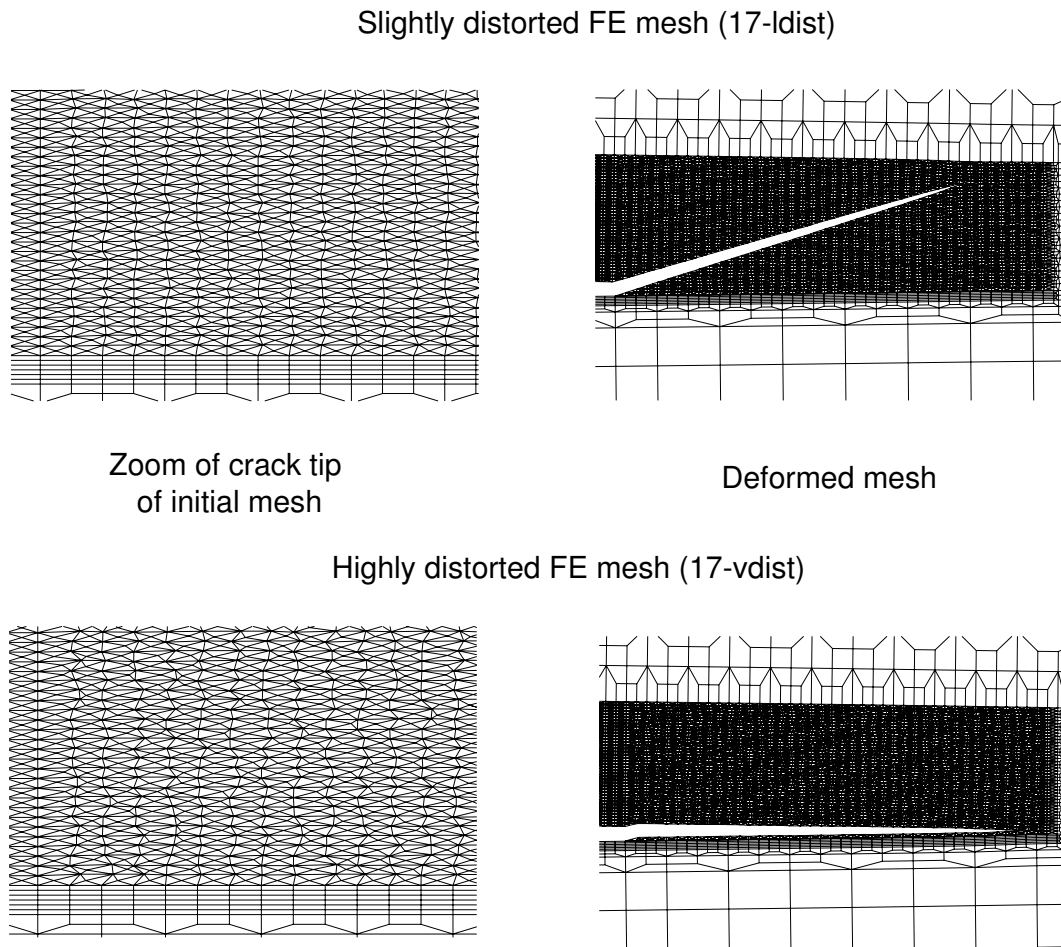
Figure 6.10: Distorted FE-meshes in the undeformed and deformed state
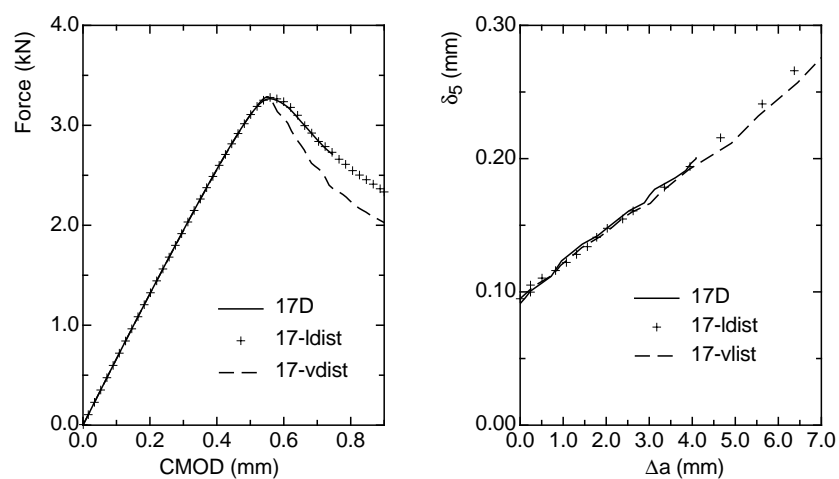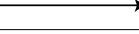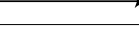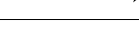
Figure 6.11: Effect of mesh irregularities on a) Force vs. CMOD and b) δ_5 vs. Δa resistance curve

wanted. The mesh design used is, however, identical as the 17D element arrangement, presented in Figures 6.7 and 6.8, that permits two main crack orientations along a 17° angle from the ligament or along the FZ/BM interface.

Both normal and tangential separations of the cohesive elements are employed. The simulations are carried out for various values of T_{0N} ranging from 275 MPa to 350 MPa. The other cohesive parameters are constant with $\Gamma_{0N} = 8$ N/mm. The ratios of normal over tangential parameters are identical in the different cases, $\Gamma_{0T} = \Gamma_{0N}$ and $T_{0T} = 0.4T_{0N}$.

The crack orientations are schematised in Figure 6.12a as function of the normal cohesive stress. The inclined arrows indicates a crack path following the 17° direction whereas the horizonzal arrows represent crack extension along the FZ/BM interface. A change in crack trajectory occurs for $T_{0N} = 310$ MPa. Below this value, the crack extends always along the 17° direction, whereas above this value, a crack always grows along the ligament. For $T_{0N} = 310$ MPa, the crack direction is not stable and multi-cracking is seen that leads to convergence problems and termination of the calculations. In order to understand the reasons of the change of crack orientation, two calculations are further investigated, namely the ones with $T_{0N} = 300$ MPa and with $T_{0N} = 325$ MPa. The overall behaviour of these two simulations in terms of force vs. CMOD is displayed in Figure 6.12b. The calculation "HAZ325" which presents the results with $T_{0N} = 325$ MPa stops just after the maximal load due to convergence problem.

a) Crack trajectories as a function
of the cohesive stress T_{0N}
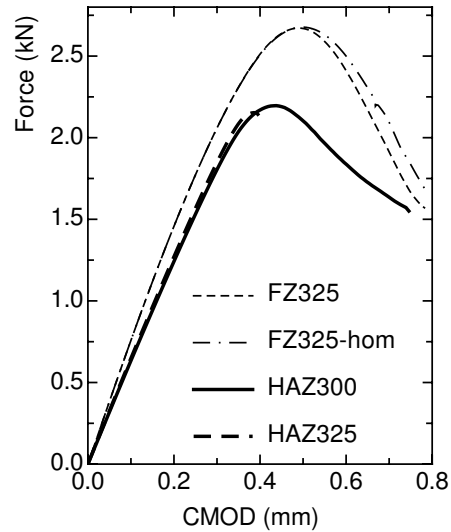
b) Force vs. CMOD curves

Figure 6.12: Influence of the cohesive strength T_0

First, the behaviour of the cohesive elements around the crack tip is analysed. Three cohesive elements are studied whose locations are indicated in Figure 6.13. Elements 8454 and 13775 are the first and second inclined cohesive elements and element 13773 is at the interface FZ/BM. The traction-separation behaviour of all interface elements is plotted in Figures 6.13a and 6.13b for $T_0N = 300$ MPa and $T_0N = 325$ MPa, respectively. They have to follow the imposed TSL. In both simulations, the three cohesive elements are

activated for small displacement as indicated in Figure 6.13d in which the normal cohesive stress is plotted as a function of the Crack Mouth Opening Displacement. The loading of the cohesive elements is identical in both cases and follows the pre-defined TSL. Then unloading or softening of the cohesive elements occurs. Unloading consists of a decrease of both traction and separation whereas softening corresponds to a decrease of traction with increasing separation. Softening of the cohesive elements is observed for the element introduced in the final direction of crack extension whereas unloading is seen in the other cases. For $T_0N = 300$ MPa, the crack extends along a $17°$ direction and the element 13773 is unloaded. For the $T_{0N} = 325$ MPa case, the opposite takes place, the 13773 interface elements behaves according to the TSL and the two others elements (8454 and 13775) are unloaded.

These phenomena are also visible in Figure 6.13d. The behaviour of the element 13775, displayed in green, is particularly interesting since variations between the two simulations occur only for this element. At a displacement value of 0.1 mm, the curves labeled "13775-300" and "13775-325" differ. An instability point is then apparent. The element does not reach the maximal cohesive strength $T_{0N} = 325$ MPa and consequently, the element 13775-325 closes which implies that the crack grows along the interface FZ/BM.

This instability point has always been observed when the crack extends along the specimen ligament. It depends on the value of δ_1: the instability occurs at a smaller displacement for a smaller value of δ_1 and vice versa. To summarise, the behaviour of the second inclined element is primordial and rules the crack extension direction.

Secondly, to investigate the origin of the instability described previously, the stresses within the continuum elements surrounding the initial crack tip have been analysed before the occurrence of the bifurcation. No obvious reasons for the appearance of an instability could be identified. Hence, no details of the stress analysis are presented here. An overall higher stress level is noted in the HAZ325 case than in the HAZ300 one due to the elevated value of T_{0N} in the first case. This does also hold for the analysis of crack extension in homogeneous material when two values of the normal cohesive strength are employed.

6.4 Comparison of stress state between homogeneous and mismatched configurations

Both the von Mises equivalent stress and the plastic strain ahead at the crack tip are investigated for three initial crack configurations in order to determine the influence of the mismatch in tensile properties of the Al6056 T78 laser weld. The three configurations are defined by the position of the initial crack:

- the crack is at the interface FZ/BM of the material. This configuration corresponds to one presented in the previous section and named "HAZ325". This case has been selected because the crack extends along the specimen ligament and no effects due to the deviation of the crack arise.

- the crack is in the middle of the FZ. The different regions of the HAZ are modelled. On the following plots, the present configuration is called "FZweld".

- the crack is within a unique homogeneous material whose tensile properties are those of the weld metal. This case is labelled "FZhom".
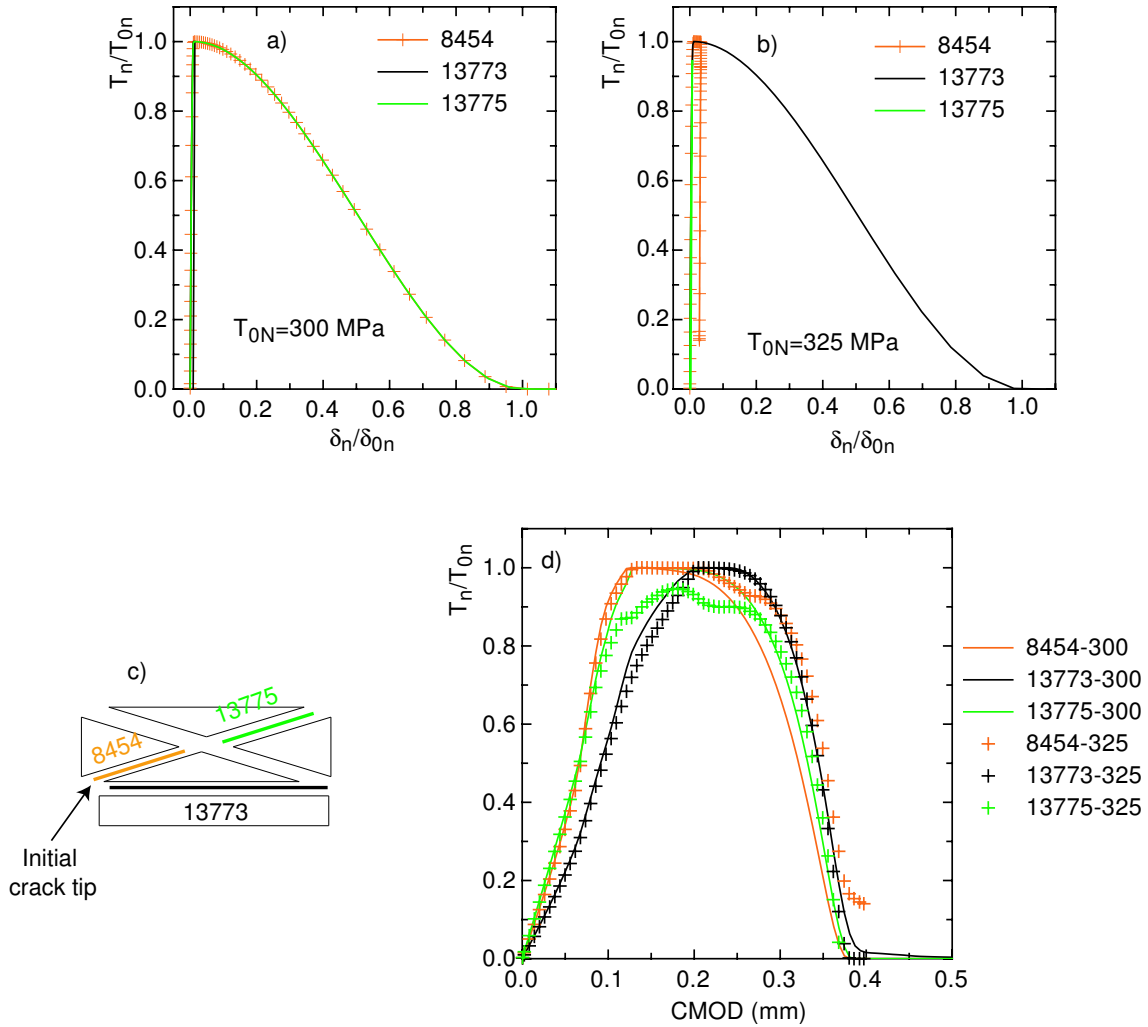
Figure 6.13: Behaviour of the cohesive elements around the initial crack tip, a) traction-separation law for $T_{0N} = 300$ MPa, b) traction-separation law for $T_{0N} = 325$ MPa, c) schematisation of the element locations, d) cohesive strength behaviour as function of the CMOD for the different elements and normal tractions studied

These three cases are presented in Figure 6.14, the material in the white regions consists of the base metal with $\sigma_{0FZ} = 302$ MPa and n=0.67, and the material in the grey areas is the weld metal with $\sigma_{0FZ} = 200$ MPa and n=0.25. In the picture, the different regions of the HAZ are represented in light grey in the FZweld sketch, the BM is modelled on each side of the HAZ but is not shown in the figure. The locations of the evaluations are also indicated in Figure 6.14. They are named after their distance from the ligament using the y-coordinate. A positive value of y indicates that the locations are within the FZ or above the FZ within the BM and a negative value stands for a measurement on the other side of the interface, within the BM in the HAZ325 case.

The simulations are carried out under plane stress state. The cohesive parameters are identical in the three cases and are: $T_0 = 325$ MPa and $\Gamma_0 = 8$ N/mm. No comparison with experimental data are presented as this plane stress state cannot reflect the real stress conditions. The global behaviour of the studied configurations are displayed in Figure

6.12b in terms of force vs. displacement. Due to the different number of cohesive elements between the HAZ325 case (10680 cohesive elements) and the two FZ cases (60 cohesive elements), a reduced stiffness is observed in the first case. The von Mises equivalent stress and the plastic strain are plotted for three different time increments that correspond to a load of F=1.12 and 2.08 kN; these two load levels are before crack initiation. The last measurements are taken at crack initiation, for HAZ325 the crack extension equals 0.23 mm whereas for the two "FZ cases" the crack is $\Delta a = 0.2$ mm.

The results of the von Mises measurements are displayed, in Figure 6.14 on the left hand side for HAZ325 and on the right hand side for the two "FZ" configurations. In all cases, the maximal stresses are at the crack tip and the equivalent von Mises stress decreases as the distance from the crack tip in both x- and y- direction increases. The values of stresses between FZweld and FZhom, are identical independently of the load level and y-values. However when normalised by the yield strength of the zone in which the values are determined, a difference will be observed at $y = 2.205$ mm; in FZweld, the material consists of HAZ1 whereas for FZhom the material is the weld metal.
The peak stress is, on the whole, higher in the FZ case than for HAZ325 except for relatively low load levels (Force=1.12 kN) for which the stress distributions are similar. For both HAZ325 and FZweld, the stresses are continuous across the interface FZ/BM and FZ/HAZ, respectively.
In HAZ325, at the crack tip, the normalised von Mises stresses ($\sigma_{mises}/\sigma_{0local}$) are higher above the interface in the FZ than below it, in the HAZ. This results in the development of a large plastic zone within the fusion zone whereas little plastic deformation is assumed to take place below the interface within the HAZ.

Figure 6.15 presents the equivalent plastic strain results of the analysed configurations. In all cases, the degree of plastic deformation is low $\epsilon pl < 0.01$ apart fromm the initial crack tip (at $y = 0.035$ mm). The level of equivalent plastic strain is identical for the two FZ cases up to a distance $y > 1.4$ mm $= h_{FZ}$. For FZhom, plasticity develops at a larger distance from the crack tip than in FZweld because no mismatch exists and the plasticity is not confined anymore within the fusion zone. At $y = 1.645$ mm, in FZhom, equivalent plastic strain are observed with a maximal value around 0.005 at $\Delta a = 0.2$ mm.
In the three configurations, the maximal plastic strain is found around the crack tip where the plastic strain values of the HAZ325 case attains the values of the FZ cases. However, for HAZ325, the plastic deformation is localised in both the fusion zone and in the base material. For y=1.085 mm no plot is presented because the plastic strain is zero.

The zones of plastic deformation are displayed in Figures 6.16 and 6.17 where different contours of plastic strain are plotted. The contours correspond to three levels of equivalent plastic strain: $\epsilon_{pl} = 0.001$, 0.005 and 0.01. The FZ is pictured by the grey region in the four drawings. Due to the symmetrical configuration of the FZ cases, the plastic regions are symmetric regarding the specimen ligament whereas in the HAZ325, the main part of the plastic deformation occurs within the FZ. Moreover, the plastic zones in the interface crack problem are smaller than in the "homogenous" cases in both x- and y-directions.
At crack initiation, the plastic zone of FZhom is higher than the one of FZweld as no gradient in tensile properties exists. In FZweld, the plastic zone is confined within the fusion zone for the studied load levels.
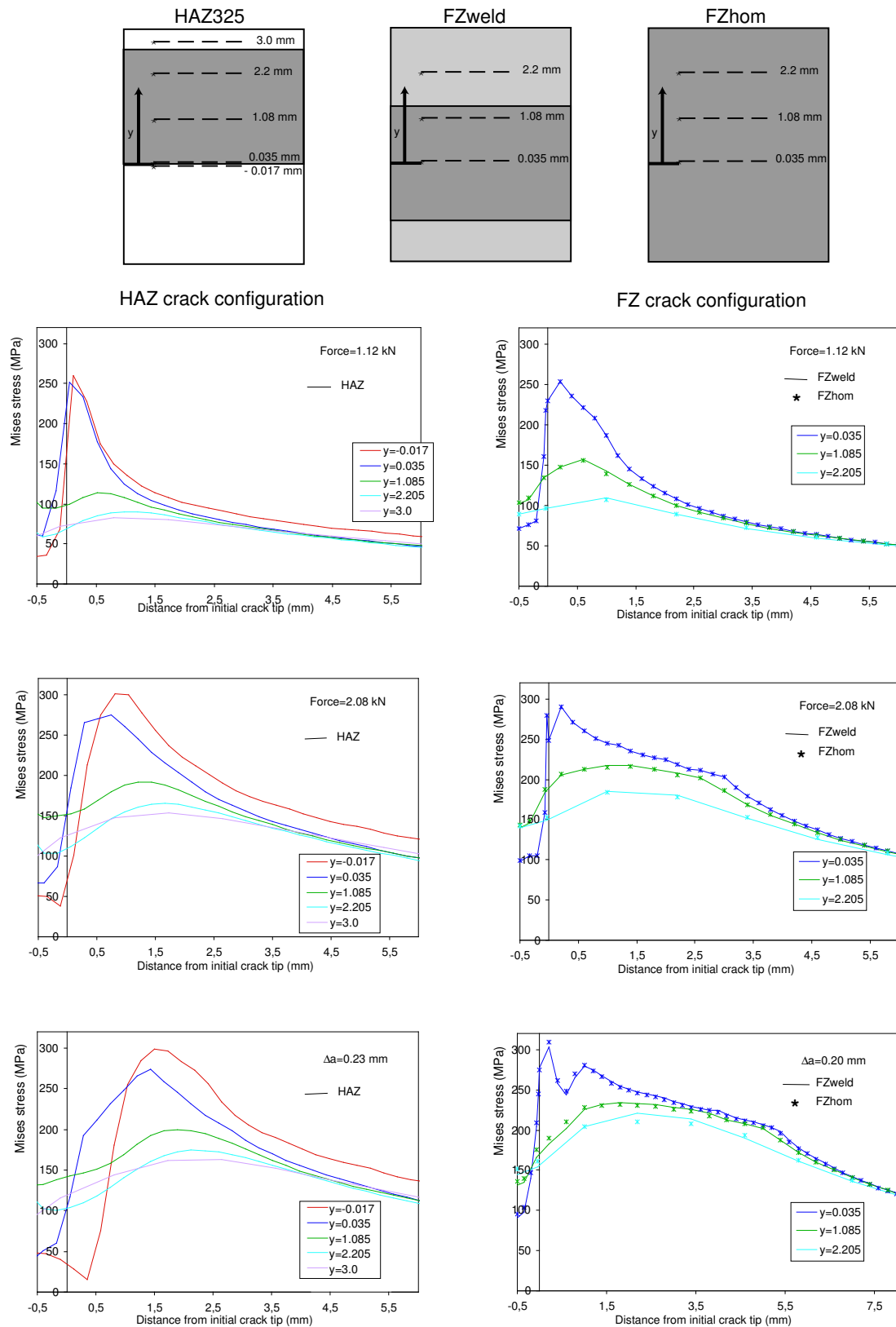
Figure 6.14: Plots of equivalent von Mises stress at the crack tip for three initial crack configurations at different numerical time increments
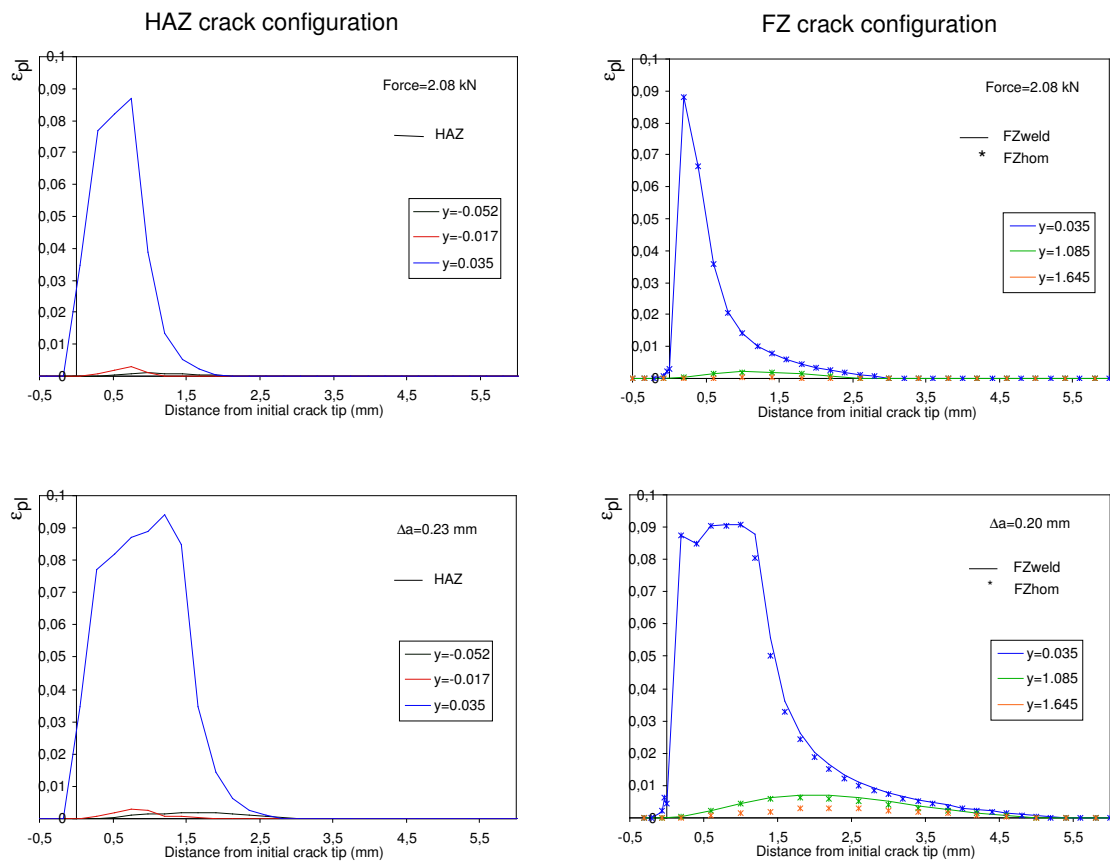
Figure 6.15: Plots of equivalent plastic strain at the crack tip for three initial crack configurations at different numerical time increments
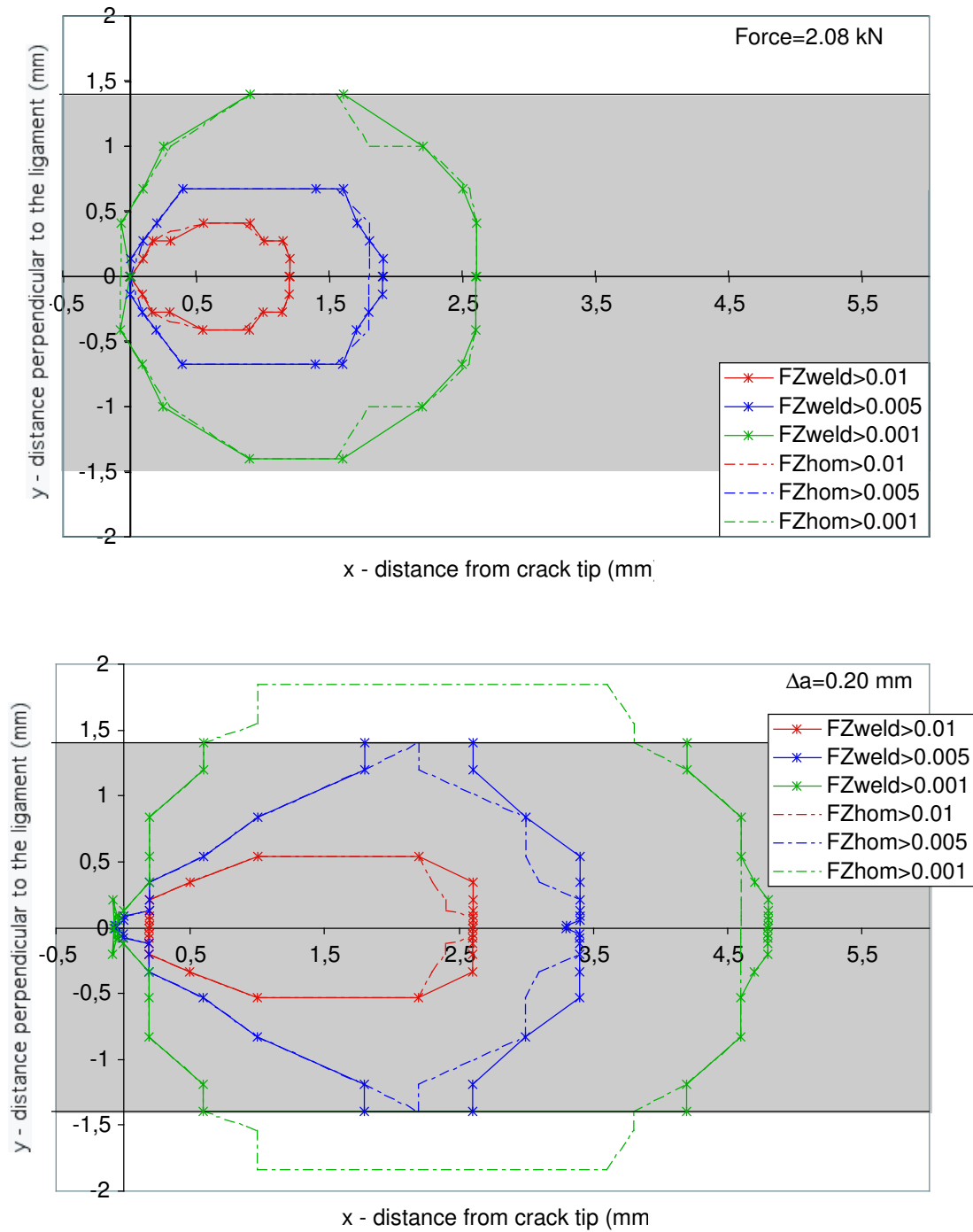
Figure 6.16: Contour plots of equivalent plastic strain for an initial crack within the fusion zone
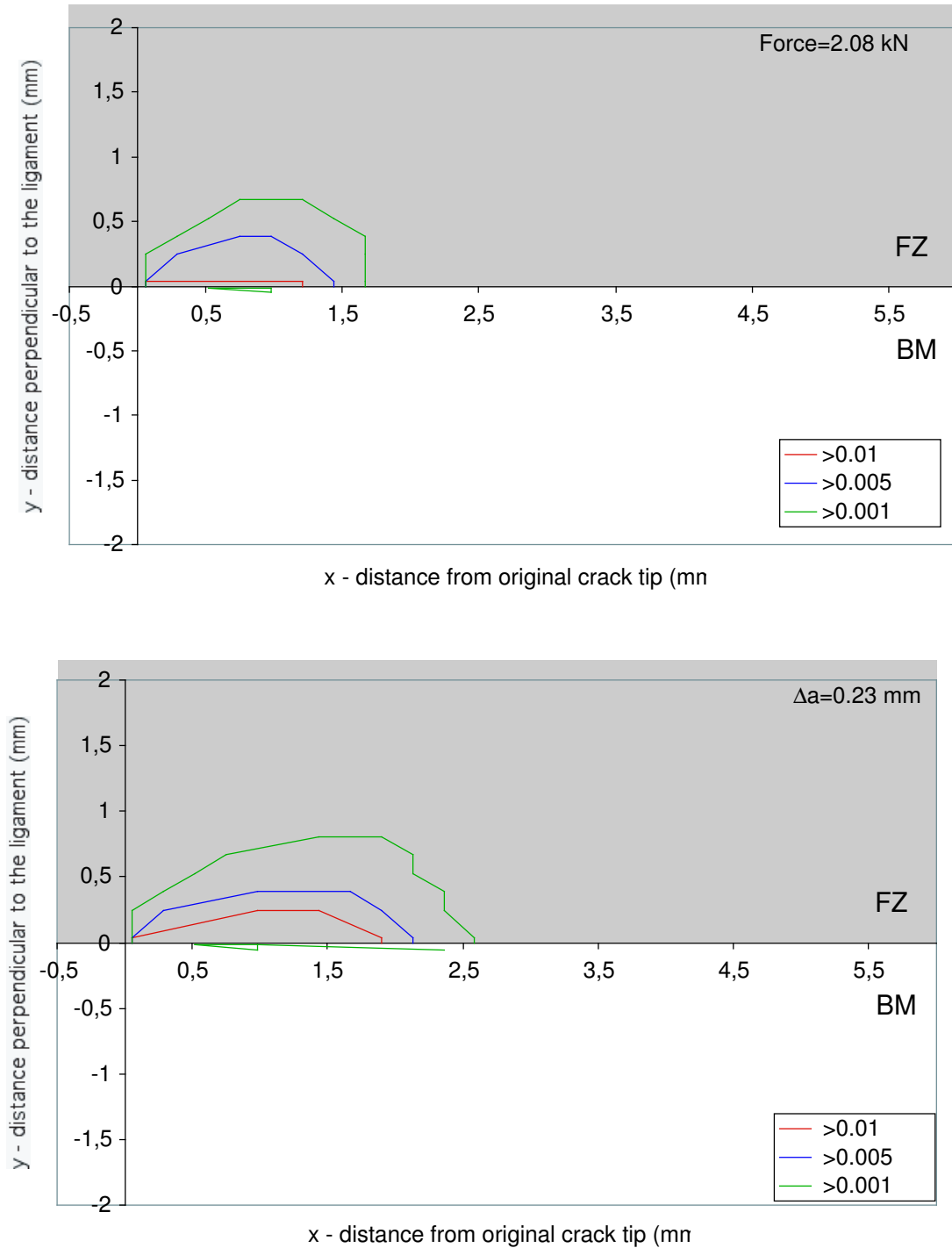
Figure 6.17: Contour plots of equivalent plastic strain for the configuration HAZ325

6.5 Concluding Remarks

Crack extension in an Al6056 T78 laser beam weld has been studied in dependence on the location of the initial crack within the different regions of the laser weld using the cohesive model. The traction-separation law proposed by Scheider [81] has been employed. The experimental data can be accurately reproduced in terms of force vs. Crack Mouth Opening Displacement and δ_5-Δa fracture resistance curves. However, similarly as the simulations carried out with the Gurson Tvergaard-Needleman model whose results are discussed in Chapters 4 and 5, the load softening after the peak load due to damage evolution is underestimated in spite of the use of 3D simulations, which are supposed to reflect the "real" stress state.

The use of the results of the Gurson-Tvergaard-Needleman simulations has proven to be efficient in the determination of the cohesive parameters. The value of the J-integral at crack initiation as well as the maximal opening stress can serve as first indication for the cohesive energy and cohesive stress, respectively. Only small adjustment of the values have been required to fit the experimental data.

The deviation of the crack path in the HAZ interface crack problem can be reproduced by the cohesive model. Nevertheless, the numerical occurrence of crack kinking depends on the possible angle of crack extension at the crack tip and on the model parameters. For a non-straight crack, it has been shown that the admissible angle of crack extension must be lower than 25° otherwise the crack extends in the ligament or parallel to the ligament, direction thus minimising the consumed energy.
Secondly, allowing several crack paths, the influence of the cohesive parameters has been investigated with emphasis put on the cohesive strength T_0. A limit exists above which the crack always grows along the interface and below which the crack is inclined. Further investigations have demonstrated that the behaviour of a single cohesive element - namely the second inclined element - is responsible for the crack growth trajectory. As loading starts, all the cohesive elements open. For further loading, this specific element either softens according to the imposed cohesive law or is unloaded. In the case of softening of the cohesive element, the crack deviates from its horizontal path. Otherwise, the crack grows along the interface. Unfortunately, no apparent reason for the selection of either direction could be detected.

Both the equivalent von Mises stresses and the plastic strain ahead of the crack tip have been analysed using identical cohesive parameters for a crack extending along the specimen ligament but for different locations of the crack within the weld. The crack has been considered either at the interface between the fusion zone and the base metal or in the middle of the Al6056 T78 LBW fusion zone or within a unique material zone whose tensile properties correspond to the one of the weld metal (low yield strength). The two last configurations can be considered as homogeneous since at the crack tip both the stresses and the equivalent plastic strain are identical. Differences in stress states and plastic deformations between the two "homogeneous" cases arise at a distance $y > 1.4$ mm from the crack tip, the limit above which the yield strength of the materials differ.
Generally, the stress level is higher in the homogeneous cases than in the interface one. As a consequence, the plastic zone of the HAZ crack problem is reduced compared to the two other ones. Furthermore the "HAZ" plastic zone is not symmetric with respect to the specimen ligament anymore due to the gradient of mechanical properties. Only a

small amount of plasticity occurs below the interface in the harder material. Moreover for the two mismatched cases, the plastic zone is confined within the fusion zone up to crack initiation.

The previous observations are valid for this specific weld configuration. A different, larger or slender weld will produce different plastic zones and stress distributions at the crack tip since the size of the fusion zone influences the constraint at the crack tip. Here, the plastic zone is large enough that an initial crack introduced in the middle of the weld metal can be considered homogeneous.

Chapter 7

Summary and conclusions

The present work deals with the characterisation of the fracture behaviour of an aluminium butt joint. Two Al6056 T4 sheets were laser beam welded (LBW). The joint has afterwards undergone a heat treatment T78 to improve its properties. Based on hardness measurements and on tensile test results on micro flat tensile specimens, three main regions are defined: the fusion zone (FZ) in which the fusion process has taken place, the parent metal which has not been affected during welding and an intermediate region called the heat affected zone (HAZ). The material in the FZ is softer than the parent metal and the Al6056 T78 LBW is undermatched with a mismatch ratio $M = \sigma_{0weld}/\sigma_{0base} = 0.67$. The material in the fusion zone is then the site of preferential deformation and damage evolution.

In the fusion zone, the two parent materials have been melted and have fused together. As no additional transformation processes have taken place, the weld metal possesses a solidification microstructure with the presence of small dendrites. The base material (BM) has a typical wrought aluminium microstructure with coarse particles that are damage nucleating sites. The microstructure in the HAZ evolves towards the base metal one as the distance from the weld increases. Quantitative analysis of the microstructure of the different materials indicate a reduced lengthscale in the fusion zone compared to the base material.

The resistance to stable crack extension of the aluminium alloy 6056 and its weld has been investigated by means of fracture mechanics tests using homogeneous base material and welded specimens. In the last case, the initial crack is either within the fusion zone or in the heat affected zone. Due to the mismatch in mechanical properties in the HAZ, the crack starting within this zone deviates from its original path (normal to the loading direction) towards the fusion zone. The crack deflection has been quantified for several specimens through topography measurements of the fracture surface. Crack deviation takes place for all the specimens; the angle of deflection varies between $10°$ and $25°$ with an average value of $17°$.

The fracture behaviour of the three previously defined initial crack configurations (crack in BM, FZ, HAZ) has been simulated using two damage models: the Gurson-Tvergaard-Needleman model (GTN-model) and the cohesive model (CM). The GTN-model is micromechanically based and relates the macroscopic properties of the material to its microstructure. Such approach requires the determination of several parameters. The initial

void volume fraction, which is assumed to be equal to the volume fraction of the coarse particles in the material, and the mesh size at the crack tip that is a function of the average particle nearest neighbourg distance are determined from the materials microstructure. The other parameters are fitted by comparing the numerical to the experimental results. The two material lengthscales in the FZ and BM, also visible on the fracture surface of the broken specimens, are conserved in the FE-simulations by using different "discretisation" lengths.

The cohesive model possesses two phenomenological parameters which are physically based: the cohesive strength and the cohesive energy. They have been determined from the numerical simulations using the GTN-model. As a first approximation of the model parameters, the method employed here is attractive if the results of the GTN-simulations are already available.

The simulation of crack extension of the HAZ initial crack configuration has been studied in details due to its originality. A bi-material and a tri-material configuration have been employed. The bi-material configuration represents the weld in a simplified way. The crack is introduced at the fusion line: at the interface between the fusion zone and the parent metal. The HAZ is omitted. This arrangement can be used to study the influence of the model parameters and of the mesh design at the crack tip. The tri-material configuration accounts for the presence of the HAZ at the crack tip between the fusion zone and the base metal. It is employed to study the influence of the mechanical properties on the joint fracture toughness.

The mesh dependency of the numerical results constitutes a drawback of the presented models. First, the refinement of the mesh at the crack tip provides convergent solutions using the cohesive model. This is not true with the Gurson-Tvergaard-Needleman model as damage takes place within a single layer of finite elements whose height is considered as a material parameter and affects the energy dissipated per crack increment. The results of the numerical simulation of crack extension using the GTN-model are then valid only for a given mesh size.

Secondly, the crack trajectory is mesh dependent for the two models considered. Using the cohesive model, the crack can only extend along the finite element boundaries. The use of triangular finite elements permits therefore two main directions of crack extension: either parallel to the fusion line or inclined by a pre-defined angle imposed by the aspect ratio of the triangular elements. The crack extends parallel to the interface BM/FZ if the pre-defined angle of deviation is too large. Otherwise the crack path is inclined. The influence of the pre-defined angle of crack deflection can be minimised by using other pre-processor tools that build non-ordered free meshes.

Strain localisation and mesh dependency occurs with the GTN-model that accounts for strain softening. Even if the crack path is unknown ab-initio, crack path deviation is dependent of the finite element aspect ratio. Non-local theories of deformation and damage have been established, which account for the gradient of continuum quantities in a finite vicinity of the respective material point. By this, localisation of deformation and damage is limited. The microstructural length scale is included in the constitutive equations and must not be introduced via the mesh size. The problem of identifying this microstructural length continues, of course, and a number of unsolved question like boundary conditions for strain gradients still inhibit a broad acceptance of the respective theories.

The HAZ fracture toughness has been studied with respect to joint properties using the

tri-material configuration. The width of the fusion zone itself is not a critical issue but the weld slenderness: the relationship between the weld width and the ligament expressed by the ratio $(W - a_0)/H_{FZ}$. In an undermatched weld, the plasticity is confined within the fusion zone and this is even more detrimental to the weld fracture toughness for a slender weld. For the studied Al6056 T78 laser weld and specimen geometry, when the crack is placed in the middle of the weld, the fusion zone is wide enough to behave similarly to an homogeneous crack configuration whose tensile properties are those of the weld metal. The material mismatch has then a limited effect on both the stresses and the plastic deformation ahead of the crack tip.

Both the tensile properties and the crack trajectory have been investigated as a function of the tensile properties of the material in the HAZ. The strain hardening exponent value of the material within the HAZ has little effect on the fracture resistance of the HAZ crack configuration. On the other hand, the HAZ yield strength is the dominant factor. Its yield strength influences the local material mismatch at the interface. A high strength material increases the mismatch ratio of the interface and thus reduces the fracture resistance of the joint. A hard material favours crack kinking.

The location of the initial crack as a function of the distance from the interface FZ/HAZ was also analysed. The crack was considered either within the fusion zone or within the heat affected zone. If the crack position varies from the interface to the middle of the weld, the load carrying capacity increases while the occurrence of crack kinking decreases. When the crack is close to the middle of the weld, no more crack path deviation occurs. The plastic zone that develops ahead of the interface crack is much smaller than the one at the center of the weld and not symmetric anymore. The stress distributions ahead of the crack for a given remote load between these two extreme cases are similar. However, the stresses in the FZ case are more intense than the ones in the interface case. For an initial crack located within the HAZ, the crack grows towards the fusion zone leading to a higher resistance to crack extension as it crosses several layer of HAZ's material.

For the three initial crack configurations (BM, FZ, HAZ), the two models are able to reproduce quantitatively the experimental fracture behaviour of the aluminium weld in terms of global behaviour (force vs. displacement) and of fracture resistance curves δ_5 vs. Δa. With both models, the load reduction due to damage is underestimated. However, the lack of experimental data for large displacement does not permit to investigate this point further. The experimental crack trajectory has been successfully simulated using both the GTN-model and the cohesive model.
The cohesive model provides fast and efficient solutions for the simulation of crack extension. Due to the requirement of using 3D analysis with the GTN-model, the simulations of crack extension require a much higher computational effort.

The transferability of the here established parameters to other specimen geometries and sizes requires to be investigated and validated. Larger compact tension specimens or large middle cracked tension specimens can be used. This additional numerical work needs to be combined with experimental tests. Moreover, the use of larger fracture specimens also permits to investigate the fracture behaviour of the present weld under conditions closer to the real ones for which the weld is slender. In large coupons, the fracture of an aluminium laser weld is often unstable due to confined plasticity at the crack tip. The stresses at the crack tip can achieve several times the weld metal yield strength at a distance of two to three times the width of the fusion zone ahead of the crack tip. Such aspect for the

studied Al6056 T78 laser weld could be further investigated using either the GTN-model or the cohesive model.

In the present work, the fracture behaviour of a crack parallel to the weld has been studied. In a real structure, the crack can also be normal to the weld. If in the latter case, the crack tip reaches the weld, two possibilities exist: the crack can either stop at the interface or run through the weld. The distance of the weld to the crack tip, the width of the weld and the mismatch ratio of the joint are critical. When a crack extends from a hard to a soft material, there is an increase in crack driving force and in void growth compared to a homogeneous material. Under which circumstances such an event can occur can be investigated numerically for the Al6056 T78 laser weld using the GTN-model since the model parameters of each zone of the weld have already been determined. Experimental tests of the simulated configurations could validate the obtained results.

Compared to experimental investigations, the use of the finite element simulations presents the advantage to be more versatile. Once the models have been validated, a variety of configurations, materials, etc ...can be efficiently investigated at minimal cost and in a relatively short time. The welding of high strength aluminium alloys still results in discrepancy in joints properties / quality which are related to the welding process itself, to the parent material .... To investigate such variations, the use of finite element is advantageous. Numerical simulations of "dummy" configurations taking into account for example the effect of the weld mismatch, of the size of the weld, etc ... allow to draw tendency of the influence of the difference parameters without carrying out a long and expensive experimental program. The improved knowledge increases the understanding of the mechanisms taking place and also permit the improvement of the existing technologies or materials.

The following conclusions can be drawn from the present work:

- Using the Gurson-Tvergaard-Needleman model, a relationship between the microscopic scale and the macroscopic properties of the material and its weld can be established.

- Since no standardised methods exist up to now to characterise the resistance to stable crack extension of a weld, the cohesive model is an attractive tool, particularly for engineers. The physically based model is relatively "easy" to handle and can also be employed to quantify the fracture toughness of components.

- Porosity models combined with the use of 3D finite elements are capable to simulate crack extension in low triaxiality sheet metal.

- The degree of undermatching of the weld influences the joint fracture toughness by affecting slightly the stress state at the crack. However, the size of the weld or its slenderness is the dominant factor.

- The deviation of the crack path can be numerically predicted. The crack trajectory affects only slightly the fracture behaviour of the weld.

Bibliography

[1] Annual book of ASTM standards. Tech. Rep. E 561-94, American Society for Testing and Materials, Philadelphia, 1998.

[2] Standard test method for measurement of fracture toughness, annual book of ASTM standards. Tech. Rep. E 1820-01, American Society for Testing and Materials, Philadelphia, 2003.

[3] BARENBLATT, G. The mathematical theory of equilibrium cracks in brittle fracture. *Advances in Applied Mechanics 7* (1962), 55–129.

[4] BARLAT, F., BREM, J. C., YOON, J. W., CHUNG, K., DICK, R. E., LEGE, D. J., POURBOGHRAT, F., CHOI, S. H., AND CHU, E. Plane stress yield function for aluminum alloy sheets–part 1: theory. *International Journal of Plasticity 19* (2003), 1297–1319.

[5] BARPI, F., AND VALENTE, S. Size effects induced bifurcation phenomena during multiple cohesive crack propagation. *Int. J. Solids Structures 35* (1998), 1851–1861.

[6] BECKER, R., SMELSER, R. E., AND RICHMOND, O. The effect of void shape on the development of damage and fracture in palne-strain tension. *J. Mech. Phys. Solids 37* (1989), 111–129.

[7] BERDIN, C., BESSON, J., BUGAT, S., DESMORAT, R., FEYEL, F., FOREST, S., LORENTZ, E., MAIRE, E., , T., PINEAU, A., AND TANGUY, B. *Local approach to fracture.* J. Besson, 2004.

[8] BERNAUER, G., AND BROCKS, W. Micro-mechanical modelling of ductile damage and tearing - results of a european numerical round robin. *Fatigue Fract. Eng. Mater. Struct. 25* (2002), 363–384.

[9] BESSON, J., STEGLICH, D., AND BROCKS, W. Modeling of crack growth in round bars and plane strain specimens. *Int. J. Solids Struct. 38* (2001), 8259–8284.

[10] BESSON, J., STEGLICH, D., AND BROCKS, W. Modeling of plane strain ductile rupture. *Int. J. Plasticity 19* (2003), 1517–1541.

[11] BLANC, C., ROQUES, Y., AND MANKOWSKI, G. Application of phase shifting interferometric microscopy to studies of the behaviour of coarse intermetallic particles in 6056 aluminium alloy. *Corrosion Science 40* (1998), 1019–1035.

[12] BRAUN, R., DALLE DONNE, C., AND STANIEK, G. Laser beam welding and friction stir welding of 6013-T6 aluminium alloy sheet. *Mat.-wiss. u. werkstofftech 31* (2000), 1017–1026.

[13] BRAUN, R., ROTH, G., AND ARNOLD, J. Nd:yag laser beam welding of 6013 aluminium alloy sheet using different filler powders. *Materials Science Forum 396-402* (2002), 1691–1696.

[14] BROCKS, W., CORNEC, A., AND SCHEIDER, I. Computational aspects of nonlinear fracture mechanics. In *Comprehensive Structural Integrity Fracture of Materials from Nano to Macro* (2003), vol. 3 Numerical and Computational Methods, R. de Borst and H Mand, pp. 127–209.

[15] BROCKS, W., KLINGBEIL, D., KÜNECKE, G., AND SUN, D. Z. Application of the Gurson model to ductile tearing resistance. In *Constraint effects in fracture: theory and applications* (1995), vol. STP 1244, American Society for Testing and Materials, pp. 232–252.

[16] BROCKS, W., AND SCHEIDER, I. Reliable J-values - numerical aspects of the path-dependence of the J-integral in incremental plasticity. *Materialprüfung 45* (2003), 264–275.

[17] BRON, F., AND BESSON, J. A yield function for anisotropic materials: Application to aluminium alloys. *Int. J. Plasticity 20* (2004), 937–963.

[18] BURSTOW, M. C., AND HOWARD, I. C. Constraint effects on crack growth resistance curves on strength mis-matched welded bend specimens. In *Mis-Matching of interfaces and welds* (1997), GKSS Research Center Publications, pp. 357–369.

[19] ÇAM, G., DOS SANTOS, J. F., AND KOÇAK, M. Laser and electron beam welding of Al-Alloys: Literature review. Tech. Rep. GKSS 97/E/25, GKSS-Forschungszentrum Geesthacht GmbH, Geesthacht, 1997.

[20] ÇAM, G., ERIM, S., YENI, C., AND KOÇAK, M. Determination of mechanical and fracture properties of laser beam welded steel joints. *Welding Research Supplement* (1999), 193s–201s.

[21] ÇAM, G., VENTZKE, V., DOS SANTOS, J. F., AND KOÇAK, M. Characterisation of laser and electron beam welded Al alloys. *Prakt. Metallogr. 36* (1999), 1–31.

[22] CHABANET, O., STEGLICH, D., BESSON, J., HEITMANN, V., HELLMANN, D., AND BROCKS, W. Predicting crack growth resistance of aluminium sheets. *Computational Materials Science 26* (2003), 1–12.

[23] CHANDRA, N. Evaluation of interfacial fracture toughness using cohesive zone model. *Composites: part A 33* (2002), 1433–1447.

[24] CHEN, B., AND DILLARD, D. A. Numerical analysis of directionally unstable crack propagation in adhesively bonded joints. *Int. J. Solids Struct. 38* (2001), 6907–6924.

[25] CHU, C. C., AND NEEDLEMAN, A. Void nucleation effects in biaxially stretched sheets. *J. Eng. Mater. Technol.-Trans. ASME 102* (1980), 249–256.

[26] CORNEC, A., AND SCHEIDER, I. Modellierungskonzept für die Versagensbewertung von Laserschweisssverbindungen. *Mat.-wiss. u. Werkstofftech. 32* (2001), 316–328.

[27] COTTERELL, B., AND RICE, J. R. Slightly curved or kinked cracks. *Int. J. Fract. 16* (1980), 155–169.

[28] DAVIS, J. R. E. *ASM speciality handbook: Aluminium and Aluminum Alloys.* 1993.

[29] DE BORST, R. Numerical aspects of cohesive-zone models. *Engng. Fract. Mech. 70* (2003), 1743–1757.

[30] DIF, R., BES, B., EHRSTRÖM, J. C., SIGLI, C., WARNER, T. J., LASSINCE, P., AND RIBES, H. Understanding and modelling the mechanical and corrosion properties of 6056 for aerospace applications. *Materials Science Forum 331-337* (2000), 1613–1618.

[31] DONNADIEU, P., LAPASSET, G., AND SANDERS, T. H. Manganese-induced ordering in the α- (Al-Mn-Fe-Si) approximant phase. *Phil. Mag. Letters 70* (1994), 319–326.

[32] DUGDALE, D. S. Yielding of steel sheets containing slits. *J. Mech. Phys. Solids 8* (1960), 100–104.

[33] EHRSTRÖM, J., AND WARNER, T. Metallurgical design of alloys for aerospace structures. *Materials Science Forum 331-337* (2000), 5–16.

[34] FABREGUE, D., AND DESCHAMPS, A. Microstructural study of laser welds Al6056-AS12 in relation with hot tearing. *Materials Science Forum 396-402* (2002), 1467–1572.

[35] FALESKOG, J., GAO, X., AND SHIH, C. F. Cell model for nonlinear fracture mechanics - I. Micromechanics calibration. *Int. J. Fract. 89* (1998), 335–373.

[36] GAO, X., FALESKOG, J., AND SHIH, C. F. Cell model for nonlinear fracture analysis - II. Fracture-process calibration and verification. *Int. J. Fract. 89* (1998), 375–398.

[37] GEGNER, J., ÖCHSNER, A., WINTER, W., AND KUHN, G. Metallographical investigations of ductile damage in aluminium alloys. *Prakt. Metallogr. 37 37* (2000), 563–579.

[38] GITTOS, N. F., AND SCOTT, M. H. Heat-affected zone cracking of Al-Mg-Si alloys. *Welding Research Supplement* (1981), 95s–103s.

[39] GOLOGANU, M., LEBLOND, J.-B., AND DEVAUX, J. Approximate models for ductile metals containing non-spherical voids - Case of axisymmetric prolate ellipsoidal cavities. *J. Mech. Phys. Solids 41* (1993), 1723–1754.

[40] GOLOGANU, M., LEBLOND, J.-B., AND DEVAUX, J. Approximate models for ductile metals containing non-spherical voids - Case of axisymmetric oblate ellipsoidal cavities. *J. Eng. Mater. Technol.-Trans. ASME 116* (1994), 290–297.

[41] GOLOGANU, M., LEBLOND, J.-B., PERRIN, G., AND DEVAUX, J. Recent developments of Gurson's model for porous ductile metals. Tech. rep., CISM, Udine, 1996.

[42] GRIFFITH, A. A. The phenomena of rupture and flow in solids. *Phil. Trans. Roy. Soc. London A 221* (1920), 163–198.

[43] GUITTEREZ, L. A., NEYE, G., AND ZSCHECH, E. Microstructure, hardness profile and tensile strength in welds of AA6013 T6 extrusions. *Welding Research Supplement* (1996), 115–s – 121–s.

[44] GURSON, A. L. Continuum theorie of ductile rupture by void nucleation and growth: Part I - yield criteria and flow rules for porous ductile media. *J. Eng. Mater. Technol.-Trans. ASME 99* (1977), 2–15.

[45] HIBBITT, KARLSSON, AND SORENSEN. *ABAQUS Theory manual 6.3.* Hibbitt, Karlsson & Sorensen, 2002.

[46] HILLERBORG, A., MODEER, M., AND PETERSSON, P.-E. Analysis of crack formation and crack growth in concrete by means of fracture mechonics and finite elements. *Cement Concrete Research 6* (1976), 773–782.

[47] HUANG, Y. Accurate dilatation rates for spherical voids in triaxial stress fields. *J. Appl. Mech.-Trans. ASME 58* (1991), 1084–1086.

[48] HUTCHINSON, J. Singular behaviour at the end of a tensile crack in hardening material. *J. Mech. Phys. Solids* (1968), 13–31.

[49] IRWIN, G. R. Analysis of stresses and strains near the end of a crack traversing a plate. *J. Appl. Mech.-Trans. ASME* (1957), 361–364.

[50] KACHANOV, L. M. *Introduction to continuum damage mechanics.* Kluwer Academic Publishers, 1986.

[51] KOÇAK, M., ÇAM, G., RIEKEHR, S., TORSTER, F., AND DOS SANTOS, J. F. Microtensile test technique for weldments. In *Weld mismatch effect*, vol. IIW Doc. SC X-F-079-98.

[52] KOPLIK, J., AND NEEDLEMAN, A. Void growth and coalescence in porous plastic solids. *Int. J. Solids Struct. 24* (1988), 835–853.

[53] KOVACHEVA, R. Metallographic investigation of Al-Si-Mg and Al-Si-Cu Alloys. *Prakt. Metallogr. 30* (1993), 68–81.

[54] LEMAITRE, J. How to used damage mechanics. *Nucl. Eng. Design 80* (1984), 233–245.

[55] LEMAITRE, J. *A course on damage mechanics.* Springer-Verlag, 1992.

[56] LEMAITRE, J., AND CHABOCHE, J. L. *Mechanics of solid materials.* Cambridge University Press, 1990.

[57] LI, W., AND SIEGMUND, T. An analysis of crack growth in thin-sheet metal via a cohesive zone model. *Eng. Fract. Mech. 69* (2002), 2073–2093.

[58] LIN, G. *Numerical investigation of crack growth behaviour using a cohesive zone model.* PhD thesis, TU Hamburg-Harburg, Geesthacht, 1998.

[59] LIN, G., MENG, X.-G., CORNEC, A., AND SCHWALBE, K.-H. The effect of strength mis-match on mechanical performance of weld joints. *Int. J. Fract. 96* (1999), 37–54.

[60] Liu, J., and Kulak, M. A new paradigm in the design of aluminium alloys for aerospace applications. *Materials Science Forum 331-337* (2000), 127–140.

[61] Melin, S. The influence of the T-stress on the directional stability of cracks. *Int. J. Fract. 114* (2002), 259–265.

[62] Moons, T., Ratchev, P., De Smet, P., Verlinden, B., and Van Houtte, P. A comparative study of two Al-Mg-Si alloys for automotive applications. *Scripta Materialia 35* (1996), 939–945.

[63] Mühlich, U., and Brocks, W. On the numerical integration of a class of pressure-dependent plasticity models including kinematic hardening. *Comp. Mech. 31* (2003), 479–488.

[64] Needleman, A. A continuum model for void nucleation by inclusion debonding. *J. Appl. Mech.-Trans. ASME 54* (1987), 525–531.

[65] Needleman, A. An analysis of decohesion along an imperfect interface. *Int. J. Fract. 42* (1990), 21–40.

[66] Needleman, A., and Tvergaard, V. An analysis of ductile rupture modes at a crack tip. *J. Mech. Phys. Solids 35* (1987), 151–183.

[67] O'Dowd, N., and Shih, C. Family of crack-tip fields characterized by a triaxiality parameter - I. Structure of fields. *J. Mech. Phys. Solids 39* (1991), 989–1015.

[68] O'Dowd, N. P., and Shih, C. F. Family of crack-tip fields characterized by a triaxiality parameter ii fracture applications. *J. Mech. Phys. Solids 40* (1992), 939–963.

[69] Østby, E. *Numerical simulations of material mismatch and ductile crack growth.* PhD thesis, Trondheim Norges Teknisk-Nturvitenskapelige Universitet, Trondheim, Norway, 2002.

[70] Pardoen, T., and Hutchinson, J. W. An extended model for void growth and coalescence. *J. Mech. Phys. Solids 48* (2000), 2467–2512.

[71] Quan, G., Heerens, J., and Brocks, W. Distribution characteristics of constituent particles in thick plate of Al 20024-T351. *Prakt. Metallogr. 41* (2004), 304–313.

[72] Ranestad, O., Zhang, Z., and Thaulow, C. Quantification of mismatch constraint for an interface crack in an elastic-plastic tri-material system. In *Mis-Matching of interfaces and welds* (1997), GKSS Research Center Publications, pp. 357–369.

[73] Rashid, M. M., and Tvergaard, V. On the path of a crack near a graded interface under large scale yielding. *Int. J. Solids Struct. 40* (2003), 2819–2831.

[74] Rice, J. A path independent integral and the approximate analysis of strain concentrations by notches and cracks. *J. Appl. Mech.-Trans. ASME 35* (1968), 379–386.

[75] Rice, J., and Rosengreen, G. Plane strain deformation near a crack tip in a power-law hardening material. *J. Mech. Phys. Solids 16* (1968), 1–12.

[76] RICE, J. R., AND TRACEY, D. M. On the ductile enlargement of voids in triaxial stress fields. *J. Mech. Phys. Solids 17* (1969), 201–217.

[77] RISTINMAA, M. Void growth in cyclic loaded porous plastic solid. *Mech. Mater. 26* (1997), 227–245.

[78] ROSE, J., FERRANTE, J., AND SMITH, J. Universal binding energy curves for metals and bimetallic interfaces. *Phys. Review Letters 47* (1981), 675–678.

[79] ROUSSELIER, G. Ductile fracture models and their potential in local approach of fracture. *Nucl. Eng. Design 105* (1987), 97–111.

[80] RUGGIERI, C., PANONTIN, T. L., AND DODDS, R. H. Numerical modeling of ductile crack growth in 3-D using computational cell elements. *Int. J. Fract. 82* (1996), 67–95.

[81] SCHEIDER, I. *Bruchmechanische Bewertung von Laserschweissverbindungen durch numerische Rifortschrittsimulation mit dem Kohäsivzonenmodell.* PhD thesis, TU Hamburg-Harburg, Geesthacht, 2001.

[82] SCHEIDER, I., AND BROCKS, W. The effect of the traction separation law on the results of cohesive zone crack propagation analyses. *Key Engineering Materials 251-252* (2003), 313–318.

[83] SCHEIDER, I., BROCKS, W., AND CORNEC, A. Procedure for the determination of true stress-strain curves from tensile tests with rectangular cross-section specimens. *Trans. ASME, J. Eng. Mater. Techn. 126* (2004).

[84] SCHEIDER, I., AND WERWER, M. FEMESH Programm zur Generierung von Eingabedatensätze für das FE-System ABAQUS. *Technical note GKSS/WMS/00/18* (2000).

[85] SCHWALBE, K.-H., AND D., H. Correlation of stable crack growth with the J-integral and the crack tip opening displacement, effects of geometry, size and material. Tech. Rep. GKSS 84/E/37, GKSS Forschungszentrum, GKSS, Geesthacht, 1984.

[86] SCHWALBE, K.-H., HEERENS, J., ZERBST, U., PISARSKI, H., AND KOCAK, M. The GKSS test procedure for determining the fracture behaviour of materials: EFAM GTP 02. Tech. Rep. GKSS 2002/24, GKSS, Geesthacht, 2002.

[87] SHA, G., O'REILLY, K., CANTOR, B., WORTH, J., AND HAMERTON, R. Growth related metastable phase selection in a 6xxx series wrought Al alloy. *Materials Science and Engineering A A304-306* (2001), 612–616.

[88] SHAN, G., KOLEDNIK, O., AND FISCHER, D. F. A numerical study on the influence of geometry variations on stable crack growth in C(T) specimens for different materials. In *Constraint Effects in Fracture: Theory and applications* (1994), vol. STP 1244, ASTM.

[89] SHI, Y., SUN, S., MURAKAWA, H., AND UEDA, Y. Finite element analysis on relationships between the J-integral and CTOD for stationary cracks in welded tensile specimens. *Int. J. Pres. Piping 75* (1998), 197–202.

[90] SHIH, C. Relationships between the J-integral and the crack opening displacement for stationary and extending cracks. *J. Mech. Phys. Solids 29* (1981), 305–326.

[91] SHIH, C. F., AND ASARO, R. J. Elastic-plastic analysis of cracks on bi-material interfaces: Part I - Small scale yielding. *J. Applied Mechanics 55* (1988), 299–316.

[92] SHIH, C. F., AND ASARO, R. J. Elastic-plastic analysis of cracks on bi-material interfaces: Part II - Structure of small scale yielding fields. *J. Applied Mechanics 56* (1989), 763–779.

[93] SHIH, C. F., AND ASARO, R. J. Elastic-plastic analysis of cracks on bi-material interfaces: Part III - Large scale yielding. *J. Applied Mechanics 58* (1991), 450–463.

[94] SIEGMUND, T., AND BROCKS, W. A user-material subroutine incoporating the Gurson-Tvergaard-Needleman model of porous metal plasticity into the abaqus finite element program. Tech. Rep. Technical note GKSS/WMG/97/2, Institut für Werkstoffforschung, GKSS, Geesthacht, 1997.

[95] SIEGMUND, T., AND BROCKS, W. Prediction of the work of separation and implications to modeling. *Int. J. Fract. 99* (1999), 97–116.

[96] SIEGMUND, T., AND BROCKS, W. A numerical study on the correlation between the work of separation and the dissipation rate in ductile fracture. *Eng. Fract. Mech. 67* (2000), 139–154.

[97] SIEGMUND, T., AND BROCKS, W. *The role of cohesive strength and separation energy for modeling of ductile fracture.* 2000, pp. 139–151.

[98] SØVIK, O. P. *Numerical modelling of ductile fracture - A damage mechanics approach.* PhD thesis, NTNU Trondheim, 1996.

[99] STARKE, E. A. J., AND STALEY, J. T. Application of modern aluminium alloys to aircraft. *Prog. Aerospace Sci. 32* (1996), 131–172.

[100] STEGLICH, D. *Bestimmung von mikrostrukturellen Parametern in Schädigungsmodellen für duktile Metalle.* PhD thesis, Technische Universität, Berlin, 1999.

[101] STEGLICH, D., PIRONDI, A., BONORA, N., AND BROCKS, W. Micromechanical modelling of cyclic plasticity incorporating damage. *Int. J. Solids Struct. 42* (2005), 343–357.

[102] SUN, D. Z., HÖNIG, A., BÖHME, W., AND SCHMITT, W. Application of micromechanical models to the analysis of ductile fracture under dynamic loading. In *Fracture Mechanics, 25th Vol.* (1995), vol. ASTM STP 1220, American Society for Testing and Materials, pp. 343–357.

[103] THOMASON, P. F. *Ductile Fracture of Metals.* Pergamon Press, 1990.

[104] TIJSSENS, M. G. A., SLUYS, B. L. J., AND VAN DER GIESSEN, E. Numerical simulation of quasi-brittle fracture using damaging cohesive surfaces. *Eur. J. Mech. A/Solids 19* (2000), 761–779.

[105] TONG, J. T-stress and its implications for crack growth. *Engng. Fract. Mech. 69* (2002), 1235–1337.

[106] TVERGAARD, V. Influence of voids on shear band instabilities under plane strain conditions. *Int. J. Fract. 17* (1981), 389–407.

[107] TVERGAARD, V. Influence of void nucleation on ductile shear fracture at a free surface. *J. Mech. Phys. Solids 30* (1982), 399–425.

[108] TVERGAARD, V. Resistance curves for mixed mode interface crack growth between dissimilar elastic-plastic solids. *J. Mech. Phys. Solids 49* (2001), 2689–2703.

[109] TVERGAARD, V., AND HUTCHINSON, J. W. The relation between crack growth resistance and fracture process parameters in elastic-plastic solids. *J. Mech. Phys. Solids 40* (1992), 1377–1397.

[110] TVERGAARD, V., AND HUTCHINSON, J. W. On the toughness of ductile adhesive joints. *J. Mech. Phys. Solids 44* (1996), 789–800.

[111] TVERGAARD, V., AND NEEDLEMAN, A. Analysis of the cup-cone fracture in a round tensile bar. *Acta metall. 32* (1984), 157–169.

[112] URRETA, S. E., LOUCHET, F., AND GHILARDUCCI, A. Fracture behaviour of an Al-Mg-Si industrial alloy. *Mat. Science Engn. A 302* (2001), 300–307.

[113] WILLIAMS, M. L. On the stress distribution at the base of a stationary crack. *J. Appl. Mech.-Trans. ASME 24* (1957), 109–114.

[114] XIA, L., AND SHIH, C. F. Ductile crack growth - III. Transition to cleavage fracture incorporating statistics. *J. Mech. Phys. Solids 44* (1996), 603–639.

[115] XIA, L., AND SHIH, F. Ductile crack growth - I. A numerical study using computational cells with microstructurally-based length scales. *J. Mech. Phys. Solids 43* (1995), 233–259.

[116] ZHANG, Z. A sensitivity analysis of material parameters for the Gurson constitutive model. *Fatigue Fract. Eng. Mater. Struct. 19* (1996), 561–570.

[117] ZHANG, Z. L., HAUGE, M., AND THAULOW, C. Two parameter characterisation of near-tip fields of a bi-material elastic-plastic interface crack. *Int. J. Fracture 79* (1996), 65–83.

[118] ZHANG, Z. L., ODEGARD, J., MYHR, O. R., AND FJAER, H. From microstructure to deformation and fracture behaviour of aluminium welded joints - a holistic modelling approach. *Comput. Mater. Sci. 21* (2001), 429–435.

[119] ZHANG, Z. L., ODEGARD, J., AND SOVIK, O. P. Determining true stress-strain curve for isotropic and anisotropic materials with rectangular tensile bars: method and verifications. *Comput. Mater. Sci. 20* (2001), 77–85.

[120] ZHANG, Z. L., THAULOW, C., AND ODEGARD, J. A complete Gurson model approach for ductile fracture. *Eng. Fract. Mech. 67* (2000), 155–168.

List of Tables

List of Figures